

# Micromagnetic study of self-organized magnetic nanostructures

## DISSERTATION

zur Erlangung des akademischen Grades  
doctor rerum naturalium  
(Dr. rer. nat.)  
im Fach Physik

eingereicht an der  
Mathematisch-Naturwissenschaftlichen Fakultät I  
Humboldt-Universität zu Berlin

von

Herr Dipl.-Phys. Roman Harald Engel-Herbert  
geboren am 28.09.1976 in Dessau

Präsident der Humboldt-Universität zu Berlin:  
i.V. Prof. Dr. Hans Jürgen Prömel

Dekan der Mathematisch-Naturwissenschaftlichen Fakultät I:  
Prof. Dr. Thomas Buckhout

Gutachter:

1. Prof. Dr. Klaus H. Ploog
2. Prof. Dr. Wolfgang Nolting
3. Prof. Dr. Wolfgang Kuch

eingereicht am: 16. Dezember 2005  
Tag der mündlichen Prüfung: 13. April 2006

## Abstract

In the present thesis the micromagnetic structure, as well as the magnetization reversal, of epitaxial MnAs films on GaAs substrates is studied. Over a wide temperature range, MnAs films show a coupled magneto-structural phase transition. As a result of the strain imposed by the substrate, a phase coexistence of the ferromagnetic  $\alpha$ -phase and the nonmagnetic  $\beta$ -phase is observed. The two phases arrange themselves in a regular fashion and the ferromagnetic areas show a large variety of micromagnetic structures. The shape and distribution of the self-organized phase pattern is determined by the substrate orientation. For anisotropic substrates, a stripe pattern is found whereas isotropic substrates lead to an island structure with three-fold symmetry.

In the focus of this work is the systematic investigation of the micromagnetic structure of anisotropically strained MnAs films on GaAs(001). The domain structure of MnAs films was investigated with MFM (magnetic force microscopy). Earlier investigations at room temperature revealed a meander-like pattern, which is due to antiparallel domains separated by a  $180^\circ$  Bloch wall. The investigations have been expanded to a large variety of film thicknesses, as well as to different phase compositions which can be tuned by the temperature, revealing a multitude of MFM contrast patterns aside from the meander-like structure. So far, their micromagnetic origin has not been understood. To completely characterize the micromagnetic properties of the self-organized stripe structure, I expanded the temperature-controlled MFM setup by a variable magnetic field assembly using a permanent magnet. Now, the magnetic structure can be investigated with high lateral resolution as a function of applied magnetic field without undesired sample heating. This gives us access to the different magnetization reversal processes of MnAs films on a microscopic scale.

A classification of the domain structure has been derived from MFM experiments. Since the MFM signal does not allow the unambiguous determination of the domain structure, I derived a simple model on the basis of uniaxial bar magnets that allows the calculation of the stray field - and thus the MFM contrast - for the classified domain types. The stray field calculations agree qualitatively with the measured contrast. Up to three basic domain types are found that are characterized by the number of subelements perpendicular to the ferromagnetic stripe. More complex domain structures can be explained by a combination of the basic domain types. Subsequent XMCDPEEM (X-ray magnetic circular dichroism photoelectron emission microscopy) measurements generally confirm the domain classification scheme.

Although the employed complementary experimental techniques show a mostly consistent picture of MnAs, the micromagnetic structure of the self-organized ferromagnetic stripes cannot be understood on the basis of uniaxial bar magnets. A fundamental problem is the fact that the introduction of subdomains implies a domain boundary that is perpendicular to the preferred direction of magnetization. This leads to a strong stray field due to the large divergence in the magnetization. XMCDPEEM measurements further show that thick films exhibit a tendency to the formation of zig-zag shaped domain walls, which is typical for domain walls with surface charges. Consequently, the question after the magnetic ground state at remanence remained unanswered. Measurements of the magnetization reversal of MnAs films show that the reversal is strongly depending on the nature of this domain transition.

A complete picture of the micromagnetic properties of MnAs films, explaining the domain structure and the magnetization reversal in a consistent way, is based on the development and application of a three-dimensional micromagnetic simulator. The main finding is that MnAs stripes start exhibiting complex magnetization distributions in depth for thicknesses larger than 100 nm. These structures are due to the planar symmetry of the magnetocrystalline anisotropy and thus due to the additional degree of freedom of the magnetization in the basal plane. Consequently, the magnetization arranges in domains of reduced stray field energy. The stability of the three-dimensional micromagnetic structure depends on the properties of the self-organized stripe structure, i.e., on the film thickness as well as on the ratio of the stripe width to thickness — and thus the temperature.

Taking into account the magnetization distribution in-depth, the remaining differences between the XMCDPEEM and the MFM results can be explained by the disturbing effect of the MFM tip. The properties of the zig-zag shaped domain boundaries, commonly observed in thicker films, are analyzed

and explained. Moreover, the micromagnetic structure of MnAs films on GaAs(111) is simulated and the understanding of the micromagnetic properties is now covering all substrate orientations. Finally, the field-dependence of the domains is investigated. It is shown that, in general, two different magnetization reversal processes are observed that are characteristic for a certain combination of film thickness and temperature. The reason for the different reversal is the nucleation of in-depth domain types.

The results presented in this work are of fundamental importance for a comprehensive understanding of the magnetic properties of strained MnAs films on GaAs substrates. The results of the micromagnetic simulations, in combination with the experimental results, allow for a determination of the micromagnetic structure in an applied field throughout the phase coexistence regime.

**Keywords:**

micromagnetic simulation, magnetic force microscopy, magnetization reversal, epitaxial ferromagnetic films

## Zusammenfassung

In der vorliegenden Arbeit wurden die mikromagnetische Struktur sowie das Ummagnetisierungsverhalten epitaktisch gewachsener MnAs Filme auf dem Substrat GaAs untersucht. In einem weiten Temperaturbereich zeigen MnAs-Filme einen gekoppelten magneto-strukturellen Phasenübergang. Auf Grund der durch das Substrat aufgeprägten Verspannung stellt sich in diesem Temperaturbereich ein selbstorganisiertes Phasengleichgewicht zwischen der ferromagnetischen  $\alpha$ -Phase und der nicht ferromagnetischen  $\beta$ -Phase ein. Im Resultat bildet sich eine regelmäßige Anordnung der Phasen heraus, wobei die ferromagnetische Phase eine Vielzahl mikromagnetischer Strukturen aufweist. Die Strukturbildung der MnAs-Phasen in dünnen Schichten ist in Form und Verteilung abhängig von der Orientierung des Substrates. Es entsteht eine Streifenstruktur für anisotrop und eine inselartige Struktur mit aufgeprägter dreizähliger Symmetrie für isotrop verspannte Filme.

Im Mittelpunkt dieser Arbeit steht die systematische Untersuchung der mikromagnetischen Struktur von anisotrop verspannten MnAs Filmen auf GaAs(001). Die Domänenstruktur von MnAs-Filmen wurde mittels magnetischer magnetischer Kraftmikroskopie (MFM) bestimmt. Frühere Untersuchungen an MnAs-Filmen bei Raumtemperatur zeigten vorzugsweise ein mäanderförmiges Muster, welches durch senkrecht zum Streifen orientierte, antiparallel magnetisierte Domänen entsteht, die durch eine Blochwand getrennt sind. Eine Ausweitung der untersuchten Filmdicken, sowie der Zugang zu unterschiedlichen Temperaturen und damit veränderten Phasenzusammensetzungen zeigten, dass neben der mäanderartigen Struktur sich noch eine Vielzahl anderer Domärentypen im Phasenkoexistenzregime ausbilden können. Deren mikromagnetische Struktur war bislang unverstanden. Um eine vollständige Charakterisierung der mikromagnetischen Eigenschaften der selbstorganisierten Streifenstruktur zu ermöglichen, habe ich den Versuchsaufbau des temperaturgeregelten MFMs durch einen externen Magnetfeldaufbau erweitert. Diese Experimentieranordnung ermöglicht die Untersuchung der magnetischen Strukturen mit hoher lateraler Auflösung in einem äußeren Magnetfeld, welches während der Messungen angelegt werden kann und ferner die Probe nicht erwärmt. Damit ist der experimentelle Zugang geschaffen worden, die unterschiedlichen Ummagnetisierungsprozesse von MnAs-Filmen auf mikroskopischer Skala zu studieren.

Eine Klassifizierung der Domänenstrukturen wurde aus den MFM-Experimenten abgeleitet. Da eine eindeutige Bestimmung der Domänenverteilung aus den MFM-Ergebnissen nicht möglich ist, habe ich ein einfaches Modell auf der Basis uniaxialer Stabmagneten entwickelt, welches es erlaubt, das Streufeld und somit den MFM-Kontrast für die klassifizierte Elementardomänen zu berechnen. Diese Streufeldrechnungen stimmen qualitativ sehr gut mit dem gemessenen Domänenkontrast überein. Das Schema der Anordnung von Domänen bei Remanenz unterscheidet bis zu drei elementare Typen, abhängig von der Zahl der Subdomänen senkrecht zum ferromagnetischen Streifen. Kompliziertere Domänenstrukturen lassen sich durch eine Kombination der drei elementaren Domärentypen erklären. Durch nachfolgende Messung mittels XMCDPEEM (Photoemissions-Elektronen-Mikroskopie des röntgenangeregten zirkular-magnetischer Dichroismus) ist das Domänenklassifizierungsschema im Wesentlichen bestätigt worden.

Trotz der Einbindung der Ergebnisse komplementärer experimenteller Techniken, die größtenteils ein konsistentes Bild liefern, kann jedoch die mikromagnetische Struktur der selbstorganisierten ferromagnetischen Streifen im Rahmen des einfachen Modells – der Anordnung uniaxialer Stabmagneten – nicht zufriedenstellend verstanden werden. Ein grundlegendes Problem stellt die Tatsache dar, dass die Einführung der Subdomänen einen Domänenübergang impliziert, der senkrecht zur bevorzugten Magnetisierungsrichtung verläuft und somit eine hohe Divergenz in der Magnetisierungsverteilung und damit ein starkes Streufeld aufweist. XMCDPEEM-Messungen zeigten, dass dieser Domänenübergang bei dicken Filmen eine Tendenz zur Bildung von Zick-Zack-förmigen Wänden hat, welches üblicherweise ein typisches Merkmal von Domänenwänden mit Oberflächenladungen ist. Damit blieb die Frage nach dem magnetischen Grundzustand bei Remanenz unbeantwortet. Weiterführende Untersuchungen von Ummagnetisierungsprozessen an MnAs-Filmen zeigten, dass deren Eigenschaften wesentlich von der Bildung dieses Domänenübergangs abhängt.

Erst mit der Entwicklung eines mikromagnetischen Simulators für dreidimensionale magnetische Strukturen auf mesoskopischer Skala ist es gelungen, diese zentralen Fragen zu beantworten und eine widerspruchsfreie Deutung der Domänenstruktur und der Unterschiede im Ummagnetisierungsverhalten zu geben. Das entscheidende Ergebnis ist, dass ab einer kritischen Filmdicke von etwa 100 nm die ferromagnetischen Streifen eine Domänenverteilung in der Tiefe aufweisen. Diese Strukturen werden durch die planare Symmetrie der magnetokristallinen Anisotropie, und somit dem zusätzlichen Freiheitsgrad der Magnetisierung in der basalen Ebene von MnAs, ermöglicht. Die

Magnetisierung ordnet sich folglich in Domänen mit reduzierter Streufeldenergie an. Die Stabilität der dreidimensionalen mikromagnetischen Struktur hängt von den Eigenschaften der selbstorganisierten Streifenstruktur ab, d.h. sowohl von der Filmdicke als auch vom Verhältnis ihrer Breite zur Filmdicke – und damit der Temperatur.

Durch die Erkenntnis, dass eine magnetische Struktur in der Tiefe des Streifens vorhanden ist, können die verbleibenden Unterschiede in den MFM- und XMCDPEEM-Resultaten als Spitzen-induzierte Wechselwirkung erklärt werden. Die Eigenschaften des bei dickeren Filmen auftretenden Zick-Zackförmigen Übergangs werden analysiert und interpretiert. Zudem wird die mikromagnetische Struktur von MnAs auf GaAs(111) simuliert und damit das Verständnis auf alle vorhandenen Substratorientierungen vervollständigt. Desweiteren wird die Feldabhängigkeit der Domänen untersucht. Es wird gezeigt, dass zwei generell unterschiedliche Ummagnetisierungsprozesse eine Rolle spielen, die von der Temperatur und der Filmdicke der Proben abhängen. Dies liegt in der Nukleation unterschiedlicher Domäentypen beim Ummagnetisierungsprozess begründet.

Die in dieser Arbeit vorgestellten Resultate sind von grundlegender Bedeutung für ein umfassendes Verständnis der magnetischen Eigenschaften von verspannten MnAs-Filmen auf GaAs-Substraten. Die Ergebnisse des Simulationsprogramms in Kombination mit den experimentellen Daten ermöglichen die Aufklärung der mikromagnetischen Struktur in einem äußeren Magnetfeld über den gesamten Phasenkoexistenzbereich hinweg.

**Schlagwörter:**

Mikromagnetische Simulation, Magnetische Rasterkraftmikroskopie, magnetische Domänen, Ummagnetisierung

# Widmung

Diese Arbeit ist in großer Liebe und tiefem Respekt meiner Frau Mandy gewidmet.



## Parts of this work have already been published

**R. Engel-Herbert**, J. Mohanty, A. Ney, T. Hesjedal, L. Däweritz, and K.H. Ploog, *Understanding the submicron domain structure of MnAs thin films on GaAs(001): Magnetic force microscopy measurements and simulations*, Appl. Phys. Lett. **84**, 1132 (2004).

**R. Engel-Herbert** and T. Hesjedal, *Calculation of the magnetic stray field of an uniaxial magnetic domain*, J. Appl. Phys. **97**, 074504 (2005).

J. Mohanty, **R. Engel-Herbert** and T. Hesjedal, *Variable field and temperature magnetic force microscopy*, Appl. Phys. A, **81**, 1359 (2005).

**R. Engel-Herbert**, T. Hesjedal, J. Mohanty, D.M. Schaadt, and K. H. Ploog, *Field dependence of micromagnetic domain patterns in MnAs films*, J. Appl. Phys., **98**, 063909 (2005).

**R. Engel-Herbert**, T. Hesjedal, D. M. Schaadt, L. Däweritz, and K. H. Ploog, *Micromagnetic properties of MnAs(0001)/GaAs(111) epitaxial films*, Appl. Phys. Lett., **88**, 052505 (2006).

**R. Engel-Herbert**, T. Hesjedal, J. Mohanty, D. M. Schaadt, L. Däweritz, K. H. Ploog, E. Bauer, R. Belkhou, S. Cherifi, S. Heun, A. Locatelli, and A. Pavlovska, *Investigation of magnetically coupled ferromagnetic stripe arrays*, Appl. Phys. A, **84**, 231 (2006).

**R. Engel-Herbert**, T. Hesjedal, J. Mohanty, D. M. Schaadt, L. Däweritz, and K. H. Ploog, *Magnetization reversal in MnAs films on GaAs(001)*, Phys. Rev. B, **73**, 104441 (2006).

**R. Engel-Herbert**, D. M. Schaadt, S. Cherifi, E. Bauer, R. Belkhou, A. Locatelli, S. Heun, A. Pavlovska, J. Mohanty, K. H. Ploog, and T. Hesjedal, *The nature of charged zig-zag domains in MnAs thin films*, J. Magn. Magn. Mat., **305**, 457 (2006).

**R. Engel-Herbert**, D. M. Schaadt, and T. Hesjedal, *Analytical and numerical calculations of the magnetic force microscopy response: A comparison*, J. Appl. Phys. **99**, 113905 (2006).

## Conference Contributions

J. Mohanty, **R. Engel-Herbert**, T. Hesjedal, L. Däweritz, K. H. Ploog, S. Cherifi, S. Heun, A. Locatelli, and E. Bauer, *Micromagnetic properties of epitaxial MnAs films on GaAs: An in-depth investigation using MFM and XMCDPEEM*, Poster: 338<sup>th</sup> WEH seminar, Nanomagnetism: New Insights with Synchrotron Radiation, Bad Honnef, January 5-7, 2005.

**R. Engel-Herbert**, J. Mohanty, T. Hesjedal, *Simulation of magnetic force microscopy of MnAs/GaAs (001)*, Poster: 69. Jahrestagung der Deutschen Physikalischen Gesellschaft, Berlin, March 4-9, 2005.

# List of Acronyms

AFM .....	Atomic Force Microscopy
CBM .....	Cantilever Beam magnetometry
CPU .....	Central Processor Unit
C/NC .....	Contact mode/ Non-Contact mode
FFT .....	Fast Fourier Transformation
FFTW .....	Fastest Fourier Transform in the West
FMR .....	FerroMagnetic Resonance spectroscopy
LEED .....	Low Energy Electron Diffraction
LEEM .....	Low Energy Electron Microscopy
LLG .....	Landau-Lifshitz-Gilbert equation
MFM .....	Magnetic Force Microscopy
MBE .....	Molecular Beam Epitaxy
MPI .....	Message Passing Interface
PEEM .....	Photo Emission Electron Microscopy
RDS .....	Reflectance Difference Spectroscopy
RHEED .....	Reflection High Energy Electron Diffraction
SEM .....	Scanning Electron Microscopy
SFM .....	Scanning Force Microscopy
SPELEEM .....	Spectroscopic Photo-Emission and Low Energy Electron Microscopy
SQUID .....	Superconducting Quantum Interference Device
TEM .....	Transmission Electron Microscopy
VT-MFM .....	Variable Temperature Magnetic Force Microscopy
XAS .....	X-ray Absorption Spectra
XMCD .....	X-ray Magnetic Circular Dichroism
XMCDPEEM .....	X-ray Magnetic Circular Dichroism Photo Emission Electron Microscopy
XPEEM .....	X-ray induced Photo Emission Electron Microscopy
XRD .....	X-Ray Diffraction

# Contents

<b>1</b>	<b>Introduction</b>	<b>1</b>
<b>2</b>	<b>The Material System MnAs-on-GaAs</b>	<b>5</b>
2.1	Structural and magnetic properties of MnAs . . . . .	6
2.2	Epitaxial growth of MnAs-on-GaAs . . . . .	8
2.3	Structural and magnetic properties of MnAs films on GaAs . . . . .	9
<b>3</b>	<b>Experimental Techniques</b>	<b>17</b>
3.1	SQUID . . . . .	18
3.2	XMCDPEEM . . . . .	18
3.3	MFM . . . . .	24
3.3.1	Principle and modes of operation . . . . .	25
3.3.2	Theoretical consideration of the MFM response . . . . .	29
3.3.3	Extensions of the MFM setup . . . . .	38
<b>4</b>	<b>The micromagnetic simulator</b>	<b>41</b>
4.1	Basics of micromagnetism . . . . .	42
4.1.1	Energy contributions in micromagnetism . . . . .	43
4.1.2	Equation of motion . . . . .	47
4.2	Description of the implementation . . . . .	50
4.2.1	Discretization of the magnetization distribution and the effective magnetic field . . . . .	50
4.2.2	Time discretization . . . . .	54
4.3	Parallelization scheme and general algorithm . . . . .	55
4.4	Test of the numerical code . . . . .	58
4.5	Extension to realistic MFM response . . . . .	62

<b>5</b>	<b>The micromagnetic structure of MnAs-on-GaAs</b>	<b>69</b>
5.1	Simple micromagnetic model . . . . .	70
5.2	The intra-stripe domain structure . . . . .	73
5.3	Zig-zag domain transitions . . . . .	78
5.4	Inter-stripe coupling . . . . .	87
5.5	Micromagnetics of MnAs-on-GaAs(111)B . . . . .	95
<b>6</b>	<b>Field dependence of micromagnetic domain pattern</b>	<b>99</b>
6.1	The virgin curve . . . . .	99
6.2	Magnetization reversal . . . . .	110
<b>7</b>	<b>Summary</b>	<b>120</b>

# Chapter 1

## Introduction

For more than 50 years, the progress in the semiconductor industry was fueled by the steadily decreasing feature size of the electronic circuit components. According to Moore's law [91], which is in fact an empirical observation published in 1965 and refined in 1975 [92], the complexity of an integrated circuit doubles every 24 months. Already now, state-of-the-art PC processors are fabricated with sub-100 nm technology. In the near future, mass fabrication of truly nanoscale structures will pose a serious roadblock for engineering. So far, only the charge of the electron has been exploited to carry, store, and process data in information technology. The spin is a further fundamental property of the electron that corresponds to a magnetic moment and thus provides a means to interact with a magnetic field. The investigation of spin-dependent electronic transport phenomena led to a new research field termed magnetoelectronics. In ferromagnetic materials, the motion of an electron depends on its spin orientation with respect to the local magnetization. These spin-related effects can only be utilized, if the spin is conserved during the transport. The characteristic length scale for spin conservation ranges from a few nanometers up to several tens of nanometers for magnetic alloys, and exceeds 100 nm for nonmagnetic metals [16].

The decrease of structural size and the introduction of spin-related phenomena into conventional semiconductor devices requires ferromagnet-semiconductor hybrid structures. These structures, which allow the development of devices with novel functionalities, were subject of intense research over the past few years [106, 107, 138]. Among potential applications are high-density non-volatile magnetic memory with integrated circuits, magnetic sensors coupled with semiconductor circuitry, and optical isolators integrated with semiconductor lasers for optical communication systems [140]. The advantages of magnetic logic devices would be non-volatility, increased data processing speed, decreased electric power consumption, and increased integration

densities compared to semiconductor devices.

A prerequisite for spintronic devices is the injection of electrons with a controlled spin state into semiconductors at room temperature. Researchers face the challenge of integrating suitable ferromagnets and semiconductors with well-defined, atomically sharp interfaces, which allow for efficient spin injection from the ferromagnetic layer into the semiconductor. For practical applications, problems associated with the combination of dissimilar materials, such as thermodynamical and morphological instabilities, as well as interfacial reactions, have to be solved [139]. Manganese arsenide is one of the few ferromagnetic materials that can be grown epitaxially on the technologically important semiconductors Si [3, 4, 140] and GaAs [141, 142, 143]. With a Curie temperature above room-temperature ( $\sim 40^\circ\text{C}$ ) and with GaAs being a superior optical and electronic material, the hybrid structure MnAs/GaAs is a promising material system, which demonstrates potential for spin injection [110] and magneto-logic applications [96, 102]. For room-temperature applications, a detailed understanding of both structural and magnetic properties of MnAs/GaAs heterostructures is mandatory.

The binary compound MnAs exists in different phases depending on the temperature. The ferromagnetic  $\alpha$ -MnAs phase crystallizes in the hexagonal NiAs structure and exhibits alternating hexagonal planes of Mn and As atoms. In the bulk,  $\alpha$ -MnAs is stable up to a temperature of about  $40^\circ\text{C}$ , at which it transforms to quasi-hexagonal (orthorhombic)  $\beta$ -MnAs by a first-order phase transition [12, 154, 155]. The lattice spacing within the hexagonal plane ( $a$ -axes) abruptly shrinks by  $\sim 1.0\%$  and ferromagnetic order breaks down in a discontinuous manner.

In epitaxial MnAs films, the phase transition is more complex as the involved strain – that depends on the substrate orientation – leads to a wide temperature coexistence region of both MnAs phases. Epitaxial MnAs films of high quality can be grown by molecular beam epitaxy (MBE) on GaAs(001) [119, 121, 140, 141], GaAs(113)A [20], GaAs(111) [34, 62] and GaAs(110) [65]. On GaAs(001) surfaces, the phase transition of MnAs films does not proceed abruptly, but a self-organizing regular pattern of alternating  $\alpha$ - and  $\beta$ -MnAs stripes is formed over a temperature range of  $10^\circ\text{C} - 40^\circ\text{C}$  [60, 61, 103]. In the  $\alpha$ - $\beta$ -phase coexistence regime the magnetization continuously decreases [19], but – as it is revealed by comparison with X-ray diffraction data [61] – this is mainly due to the decrease of the ferromagnetic  $\alpha$ -MnAs fraction. The phase transition itself remains first-order [97]. As it will be discussed later, the width of the  $\alpha$ -stripes is a function of temperature<sup>1</sup> and

---

<sup>1</sup>For a film thickness of 180 nm the width of the ferromagnetic stripes is 750 nm.

the  $\alpha$ - $\beta$ -stripe periodicity scales with the film thickness. The  $\alpha$ - $\beta$ -stripe array can be easily observed in AFM as the thickness of the  $\alpha$ -stripes is about 1.2% larger than those of the  $\beta$ -wires. The surface modulation due to the phase coexistence was described within an elastic model and results in almost rectangular cross-sections of the stripes [60, 103]. The micromagnetic images exhibit a large variety of domain patterns that depend on the tunable stripe width and film thickness [31, 87].

Despite the success in the growth of epitaxial MnAs and first magnetic studies of the MnAs-on-GaAs system [87, 120], no explanation of the micromagnetic properties was yet given. In order to judge the applicability of the material system for spintronics or magnetic memory devices it is necessary to understand and control the magnetic domain structure of the film, to predict the remanent state and to understand the magnetization reversal characteristics in detail.

In this thesis, a systematic investigation of the magnetic domain structure of MnAs films grown on different GaAs surface orientations is presented. The domain structure is affected by the film thickness, by applying a magnetic field and by the temperature due to the phase coexistence. The strain-mediated self-organization of the phases determine both shape and arrangement of the ferromagnetic phase. For the investigation of the micromagnetic structure of MnAs films in the phase coexistence regime, magnetic force microscopy (MFM) is the method of choice imaging the domain structure with sub- $\mu\text{m}$  resolution [76]. The extension of the temperature-controlled MFM setup by an in-situ applied magnetic field allows for a complete experimental determination of the magnetization distribution in the phase coexistence regime. The experimental results have been extended by the analysis of X-ray magnetic circular dichroism photo emission electron microscopy (XMCDPEEM) images. Both techniques are complementary: XMCDPEEM provides the direct observation of one magnetization component (parallel to the incident beam) from the surface of the sample and in MFM the stray field, i.e. only an indirect measure of the magnetization distribution, is recorded.

The self-organized arrangement of sub- $\mu\text{m}$ -sized, ferromagnetic material has lateral dimensions that lead to finite-size effects of the magnetization due to film thickness and lateral confinement, while they are sufficiently large to presume that the magnetization distribution sustain inhomogeneous three-dimensional arrangements of the magnetization. Micromagnetic simulations are needed to explore the internal structure of the magnetization, which is not accessible by magnetic imaging techniques. For this purpose, a micromagnetic solver capable of calculating the equilibrium magnetization distribution



of large three-dimensional arrays of mesoscopic ferromagnetic ensembles has been developed and applied. The comparison of simulated results with the experimental findings allows for an unambiguous interpretation of the different, complicated and unexpected magnetization distribution. By applying the troika of two complementary experimental techniques with the micromagnetic simulator, an understanding of the micromagnetic structure of the self-organized magnetic nanostructures of MnAs/GaAs films was gained.

The structure of the thesis is as follows: a brief introduction to the material system MnAs and a summary of the structural and integral magnetic properties of MnAs films on GaAs substrate with the orientations (001) and (111)B is given in Chapter 2. The measurement techniques used for the analysis with emphasis on magnetic force microscopy and supporting stray-field simulations of the MFM response are described in Chapter 3. Chapter 4 provides an introduction to the theory of micromagnetism and deals with the micromagnetic simulator. The implementation of the algorithm as well as the evaluation of the numerical code are reported. In Chapter 5, the magnetic structure of MnAs on GaAs(001) and GaAs(111)B in absence of an applied field is discussed. Chapter 6 presents the field-dependent investigations of the stability of the domain structures in an applied field, and of the temperature-dependent magnetization reversal processes in a set of MnAs/GaAs(001) films. Finally, a summary and outlook is given in Chapter 7.

Throughout the thesis, SI units are used for the magnetic field and the magnetization.

# Chapter 2

## The Material System MnAs-on-GaAs

The integration of ferromagnetic and semiconductor materials is challenging as a suitable combination must allow for epitaxial film growth, exhibit thermodynamic stability without interfacial reactions, and morphological stability without the formation of agglomerations on the substrate [139]. None of the elemental ferromagnetic metals in combination with standard group IV semiconductors, like Si, or III-V semiconductors, like GaAs, can meet all of these stringent requirements [153].

Although the crystal structure, chemical bonding, electronic and other properties are generally very different between ferromagnetic metals and semiconductors, Mn-based ferromagnetic metallic compounds, sharing common atomic species with the underlying III-V semiconductor, were found to be suitable alloys for dissimilar heteroepitaxy [140]. In particular, MnGa and MnAl have been successfully grown on GaAs employing MBE, where the precise control of the growth process is mandatory to obtain a compound with the desired ferromagnetic properties [143]. The advantage of a magnetic binary compound based on arsenides is the compatibility with conventional III-V MBE. Remarkably, MnAs fulfills these prerequisites and is therefore a promising candidate to realize magnetic semiconductor hybrid structures.

This chapter gives an overview of the properties of bulk MnAs and summarizes the epitaxial growth of MnAs films on GaAs substrates with different orientations, namely on GaAs(001) and GaAs(111)B. Additionally, the structural and magnetic properties of MnAs films are explained as a consequence of crystallographic orientation and epitaxial constraints of the substrate.

## 2.1 Structural and magnetic properties of MnAs

The ferromagnetic nature of MnAs is known since first experiments about the synthesis of non-magnetic compounds to magnetic alloys has been performed [51]. MnAs exhibits three different phases: the low temperature  $\alpha$ -phase, the intermediate  $\beta$ -phase and the high temperature  $\gamma$ -phase [48]. The crystal structure of the  $\alpha$ -phase and the  $\gamma$ -phase is of hexagonal NiAs ( $B8_1$ ) symmetry with alternating hexagonal planes of manganese and arsenic atoms, see Fig. 2.1(a).

MnAs is ferromagnetic in its  $\alpha$ -phase up to about 40°C at which it undergoes a coupled magnetic and structural phase transition to the  $\beta$ -phase. The ferromagnetic order of  $\alpha$ -MnAs discontinuously breaks down, accompanied by an abrupt change in volume: the lattice constant of the  $a$ -axis decreases by  $\sim 1.2\%$ , while the  $c$ -axis remains unchanged. The temperature hysteresis of about 10°C and the latent heat of 7500 J/kg indicates a first order phase transition [12, 24]. Additionally, the crystal structure of MnAs changes from the hexagonal  $B8_1$  structure to the orthorhombic MnP ( $B31$ ) type. The crystal structure of the  $\beta$ -phase deviates slightly from the other phases, since the manganese atoms are displaced out of the centers of hexagonal symmetry to form one shorter manganese-arsenic bond [155]. X-ray measurements reveal that for increasing temperature the orthorhombic ‘distortion’ decreases con-

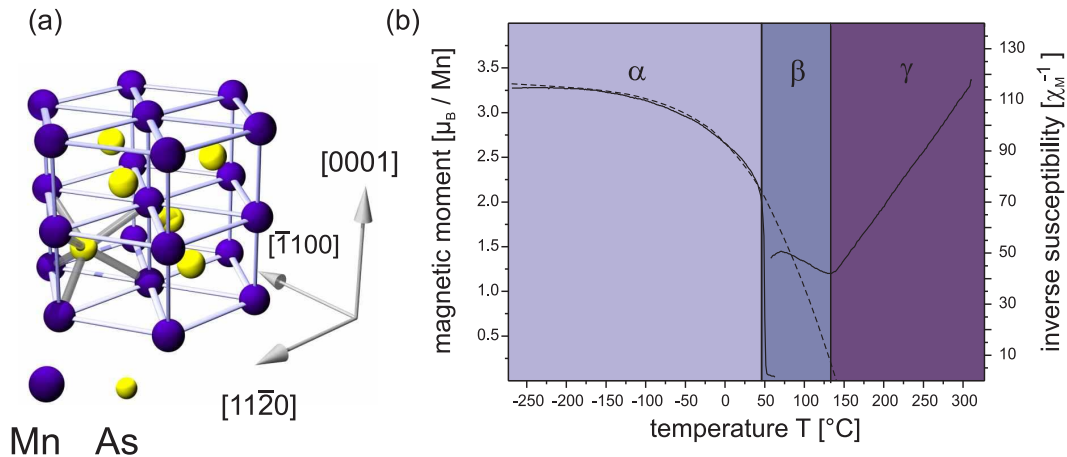


Figure 2.1: (a) Crystal structure ( $B8_1$ ) of MnAs in the  $\alpha$ - and  $\gamma$ -phase. (b) Magnetic properties of MnAs (at atmospheric pressure). The image is taken from Ref. [80]. The dotted line indicates the Brillouin function  $B_1(T)$ .

Table 2.1: Lattice constants, linear thermal expansion coefficients  $\kappa^{\alpha,\beta}$ , saturation magnetization and magnetocrystalline anisotropy constants of bulk MnAs, taken from Ref. [23].

Structure		Magnetism	
$c = 5.71 \text{ \AA}$	$\kappa_{0001}^{\alpha,\beta} = 2.8 \cdot 10^{-5}$	$K_{u_1} = -5.75 \cdot 10^5 \text{ J/m}^3$	
$a = 3.72 \text{ \AA}$	$\kappa_{11\bar{2}0}^{\alpha} = -1.1 \cdot 10^{-4}$	$K_{u_2} = 1.5 \cdot 10^5 \text{ J/m}^3$	
	$\kappa_{11\bar{2}0}^{\beta} = 6.3 \cdot 10^{-5}$	$K_{u_3} = -1.15 \cdot 10^5 \text{ J/m}^3$	

tinuously until the reversion to the hexagonal B8<sub>1</sub> structure at about 125°C is completed [155]. This temperature marks the phase transition from  $\beta$ -MnAs to  $\gamma$ -MnAs, which is of second order. It is remarkable that it coincides with the virtual Curie temperature of the extrapolated magnetization curve of  $\alpha$ -MnAs using the Brillouin function. Temperature-dependent measurements of the susceptibility revealed that  $\gamma$ -MnAs is paramagnetic, obeying the Curie-Weiss law, see Fig. 2.1 (b).

The magnetic order of  $\beta$ -MnAs cannot be conclusively determined and waits for final experimental proof. On the one hand, the anomalous behavior of the susceptibility of  $\beta$ -MnAs [see Fig. 2.1(b)] and the virtual disappearance of ferromagnetic order at about  $T \approx 130^\circ\text{C}$  indicate a remaining coupling. Moreover,  $\beta$ -MnAs can be transferred back to ferromagnetic  $\alpha$ -MnAs at temperatures far above the  $\alpha$ - $\beta$ -phase transition temperature by applying large magnetic fields [18, 57, 84]. The entropy change at the low temperature (first order) phase transition does not imply complete randomization of the spins [45]. On the other hand, this entropy change was evaluated to be larger than one would expect for a transition between two ordered magnetic phases [24]. Additionally, no long range magnetic order has been detected by neutron diffraction [7]. A possible explanation of these contradictory experimental results has been proposed recently. Density functional theory studies of  $\beta$ -MnAs discard paramagnetism and supports an antiferromagnetic state with lacking long-range order [99].

Torque magnetometer measurements performed on single crystalline  $\alpha$ -MnAs provide anisotropy constants and magnetization values [23], exhibiting an uniaxial magnetocrystalline anisotropy and a saturation magnetization at 35°C of  $M_s = 630 \text{ kA/m}$ . The anisotropy constants are given in Tab. 2.1.

## 2.2 Epitaxial growth of MnAs-on-GaAs

MnAs can be grown epitaxially on different GaAs surface orientations employing solid source MBE. Successful heteroepitaxy has been demonstrated on the substrate orientation GaAs[001] [119, 121, 140, 141], GaAs[113]A [20], GaAs[111]B [62], and GaAs[110] [65]. Here, the epitaxial growth of MnAs films on GaAs(001) and GaAs(111)B is briefly summarized.

For the epitaxial growth of MnAs on epi-ready GaAs(001) wafers, a GaAs buffer layer of 100 nm thickness was grown at a temperature of 550°C after oxide desorption. The substrate is cooled down to 250°C in As-rich environment, accompanied by a change of the surface reconstruction from  $(2 \times 4)$  to  $c(4 \times 4)$  [119, 141]. MnAs films were grown with a rate of 5 to 20 nm/h with a beam equivalent pressure ratio  $\text{As}_4/\text{Mn}$  of 90 [118]. For this substrate temperature MnAs grows in the  $\gamma$ -phase. In situ RHEED and RDS measurements reveal that there exist two possible epitaxial relations for MnAs on GaAs(001) surfaces, depending on the surface stoichiometry [119]: the A orientation, where  $(\bar{1}100)\text{MnAs} \parallel (001)\text{GaAs}$  and  $\text{MnAs}[0001] \parallel \text{GaAs}[1\bar{1}0]$ , and the B orientation with  $(\bar{1}100)\text{MnAs} \parallel (001)\text{GaAs}$  and  $[0001]\text{MnAs}$  ( $c$ -axis)  $\parallel \text{GaAs}[110]$ . In both cases the  $c$ -axis and the  $a$ -axis of MnAs are in-plane, however, the orientations differ by an azimuthal rotation of 90°.

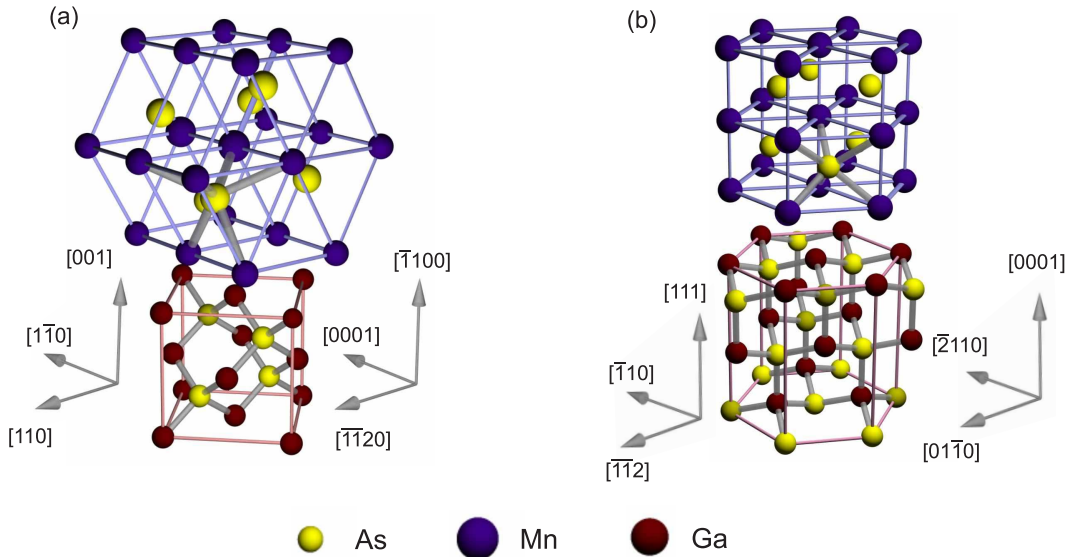


Figure 2.2: Epitaxial relationship of (a) MnAs on GaAs(001) in the A orientation and (b) MnAs on GaAs(111)B.

The crystal structure and the epitaxial relation are shown in Fig. 2.2(a). The dominant orientation of the MnAs films is mainly defined by the surface reconstruction and the termination of the GaAs(001) template. The growth conditions were chosen to assure the A orientation.

Transmission electron microscopy revealed an atomically sharp interface and no interfacial layer is apparent [149], although the lattice mismatch along the  $a$ -axis is  $\sim 7\%$  and along the  $c$ -axis of MnAs  $\sim 30\%$ , respectively. At the interface a coincidence lattice is formed along the  $c$ -axis direction where every 4<sup>th</sup> MnAs {0002} plane matches every 6<sup>th</sup> GaAs {220} plane, leading to a reduced lattice misfit of  $\sim 5\%$  [119].

For the growth of MnAs on GaAs(111) epi-ready GaAs(111)B substrates were used, where the surface is As terminated. First, a 400 nm GaAs buffer layer was grown at 600° C showing a  $(\sqrt{19} \times \sqrt{19})R23.4^\circ$  surface reconstruction. The samples were then cooled down to the growth temperature of MnAs films, ranging from 220 – 370°C, accompanied by a change of the RHEED pattern indicating a  $(2 \times 2)$  reconstruction. The growth rate and the As/Mn flux ratio were 230 nm/h and 2.5, respectively [62]. This leads to MnAs films on GaAs(111)B substrates that are exclusively  $c$ -plane oriented and the lattice mismatch along the  $a$ -axis is  $\sim 7\%$  [34]. The basal plane of MnAs is now in the film plane [cf. Fig. 2.2(b)]. This is in contrast to the growth on GaAs(001) where the prismatic plane of MnAs( $\bar{1}100$ ) is in the film plane.

## 2.3 Structural and magnetic properties of MnAs films on GaAs

When cooling the MnAs/GaAs heterostructures from growth temperature down to room temperature, one would expect that MnAs passes the two phase transitions completely, ending up in the pure  $\alpha$ -phase at room temperature. Instead, a coexistence regime of  $\alpha$ - and  $\beta$ -phase is established in epitaxial films over a wide temperature interval. This is a quite intriguing behavior, as the phase transition is of first order. The apparent violation of Gibb's phase rule turns out to be a strain-mediated phase coexistence in heteroepitaxial films, where the free energy released at the phase transition and the emerging elastic energy are balanced [60, 61].

The strain is caused by three interdependent properties of the system:

- the discontinuous change of the lattice constant  $a$  within the basal plane at the phase transition

- the crystallographic lattice mismatch between MnAs and GaAs
- the difference of the thermal expansion coefficients of GaAs and MnAs

Consequently, the epitaxial relation of film and substrate influences the structural and magnetic properties. In the following, I will discuss the consequences for MnAs films on the substrate orientations GaAs[001] and GaAs[111]B.

**MnAs/GaAs(001):** The two lattice directions  $a$  and  $c$  are clamped to the substrate leading to anisotropic strain. The thermal expansion coefficients of MnAs are about one order of magnitude larger than those of GaAs [154]. Cooling from growth temperature to room temperature gives rise to a tensile strain in the MnAs film along the  $c$ -axis direction [19].

On the other hand, the film behaves differently in the  $a$ -axis direction. Here, the abrupt expansion of the basal plane causes two effects. First, in the in-plane  $a$ -axis direction, the expansion causes a large strain that is effectively reduced by forming  $\beta$ -MnAs. Second, the MnAs film changes its volume by uniaxial expansion in the growth direction. The resulting modulation of

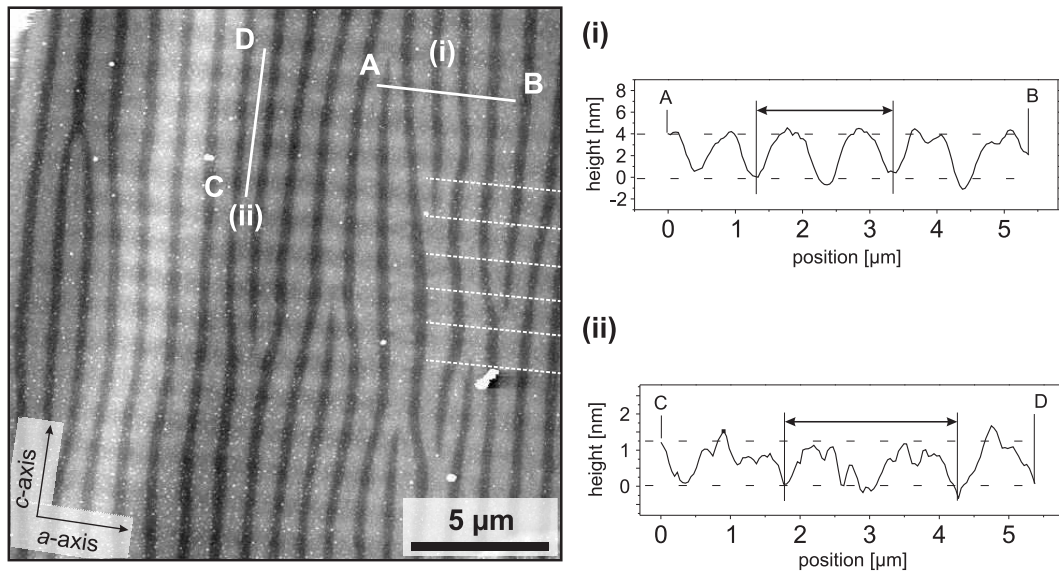


Figure 2.3: AFM micrograph of the two-dimensional strain modulation on a 215 nm thick MnAs film grown on GaAs(001) measured at room temperature (left). The positions of the line scans, shown on the right hand side, are indicated by white lines (i) and (ii) in the AFM image.

the topography of the  $\alpha$ - $\beta$ -phase coexistence structure is about 1.7% and compares well with the 1.9% calculated for a clamped bulk crystal [45]. In result, the  $\alpha$ - $\beta$  coexistence regime exhibits ordered stripes of the two phases, which relax the built-up strain along the  $a$ -axis direction. However, the smaller strain along the  $c$ -axis direction remains intact [89].

The lateral distribution of the two phases can be identified with AFM [63]. The height modulation due to the expansion of  $\alpha$ -MnAs normal to the film forms ridges consisting of  $\alpha$ -MnAs (bright) separated by  $\beta$ -MnAs valleys (dark), as illustrated in Fig. 2.3. The  $\alpha$ - $\beta$ -stripe structure is oriented parallel to the  $c$ -axis. The period of the stripe structure, measured along the line indicated by (i), is  $1.1 \mu\text{m}$  and the peak-to-valley height modulation roughly 4 nm. Perpendicular to this array along the  $c$ -axis direction, a second height modulation is visible that is indicated by the dotted white lines. Its period is  $1.28 \mu\text{m}$  and the height modulation is around 1 nm along line (ii). The latter modulation can be attributed to the remaining strain along the  $c$ -axis [89].

A multitude of samples has been analyzed to precisely determine the  $\alpha$ -

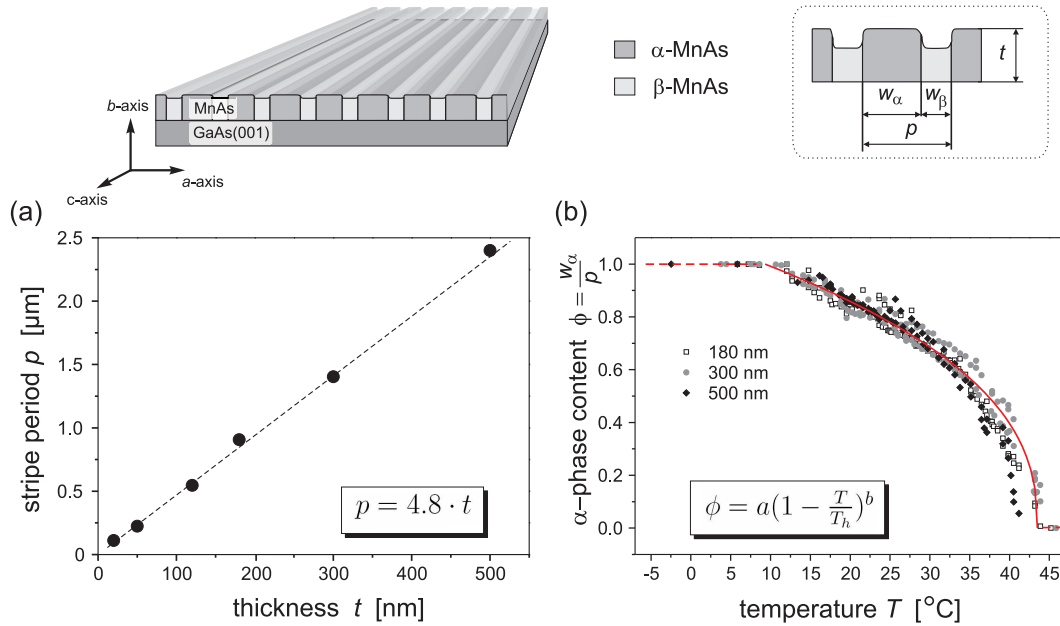


Figure 2.4: Sketch of the phase content. The period of the stripe structure  $p$  varies linearly with film thickness (a). The temperature dependence of the phase content  $\phi$  of ferromagnetic  $\alpha$ -MnAs is shown for three film thicknesses (b).



$\beta$ -stripe phase characteristics on the basis of XMCDPEEM measurements [90]. The phase coexistence of MnAs on GaAs(001) shows two characteristic features in dependence of film thickness (a) and temperature (b) in Fig. 2.4. First, the period of the stripe structures  $p$  is linearly dependent on the film thickness  $t$  ( $p = 4.8 \cdot t$ ). Second, upon changing the temperature of a film with a given thickness, the period of the stripes remains to first approximation unchanged, whereas the phase content  $\phi$ , and thus the ratio of the stripe widths  $w_\alpha/w_\beta$ , varies within the range of purely  $\alpha$ -phase ( $\phi = 1$ ) at the low temperature onset of the phase coexistence ( $T_l \approx 10^\circ\text{C}$ ), up to the complete disappearance of the  $\alpha$ -phase ( $\phi = 0$ ) at the temperature  $T_h \approx 40^\circ\text{C}$ . The  $\alpha$ -phase content  $\phi$  can be expressed as a function of temperature:  $\phi(T) = a \cdot (1 - T/T_h)^b$ . The parameters  $a = 1.10 \pm 0.01$ ,  $b = 0.368 \pm 0.01$  and  $T_h = (41.4 \pm 0.12)^\circ\text{C}$  are obtained by fitting a set of data from samples with three different film thicknesses. The largest errors in the determination of the phase content occur close to the phase transition temperature, as the stripes become discontinuous. For the fit, data near  $T_h$  have been omitted and only experimental values of  $\phi$  in the temperature range of  $10^\circ\text{C}$  to  $40^\circ\text{C}$  were considered. With these parameters the temperature onset of the phase coexistence ( $\phi(T_l) = 1$ ) was determined to  $T_l = 9.4^\circ\text{C}$ . It has to be noted that the fit parameters presented here are not universal for all films investigated, but can differ slightly from sample to sample.

Further complications in determining the phase content as a function of temperature arise from the fact that the film exhibits a temperature hysteresis. For a reliable prediction of  $\phi$  at a certain temperature, the history of the sample has to be taken into account. Second, the phase coexistence window can be shifted to higher temperature by applying an external magnetic field [98]. Third, the phase content is affected by the change of the stress in the film. This is indicated by an increase of the phase content in the vicinity of a crack at the same temperature [89].

The integral magnetic properties of MnAs on GaAs(001) have been determined by SQUID magnetometry [120]. An external field was applied along the MnAs $[11\bar{2}0]$ ,  $[1\bar{1}00]$  and  $[0001]$  directions. A representative result at room temperature is shown in Fig. 2.5 for a 180-nm-thick film. The measurements reveal that the easy axis of magnetization is along the  $[11\bar{2}0]$  direction, showing a square-like loop with a small coercive field and a high remanent magnetization [Fig. 2.5(a)]. The film behaves like a single domain system. The measured saturation magnetization is 480 kA/m. However, since a small fraction of MnAs is already in the  $\beta$ -phase and does not contribute to the SQUID signal, the saturation magnetization must be corrected for the phase content [ $\phi(20^\circ\text{C}) = 0.86$ ]. The phase-content-corrected saturation magnetization is thus 550 kA/m. To saturate the magnetic moments along the other

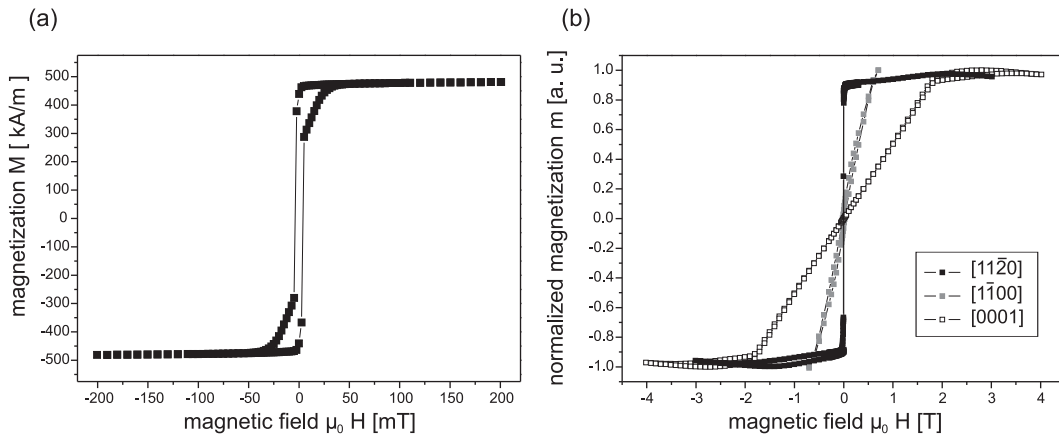


Figure 2.5: (a) Magnetization curve of a 180-nm-thick MnAs film on GaAs(001) with the field applied along MnAs $[11\bar{2}0]$  (in-plane  $a$ -axis). (b) Comparison of the magnetization curves for a magnetic field applied along  $[11\bar{2}0]$ ,  $[1\bar{1}00]$  and  $[0001]$ .

two directions, relatively high fields are necessary: 2 T along the  $c$ -axis and 0.8 T normal to the film, respectively. The higher saturation fields can be attributed to magnetic anisotropies, namely the magnetocrystalline anisotropy along the  $c$ -axis in the plane and the shape anisotropy perpendicular to the film plane. From the SQUID curves, the effective anisotropy constants  $K_{\text{eff}}$  can be deduced using the definition of  $K_{\text{eff}}$ :

$$K_{\text{eff}} = \int_0^{M_s} \mu_0 H dM. \quad (2.1)$$

In other words,  $K_{\text{eff}}$  is a measure for the energy required to saturate the magnetization along different directions, i.e. the area enclosed between the magnetization curve  $M(H)$  and the  $M$ -axis [161]. From SQUID measurements, the effective anisotropy constants were determined to be  $K_{\text{eff}}^{(0001)} = 520 \text{ kJ/m}^3$  and  $K_{\text{eff}}^{(1\bar{1}00)} = 220 \text{ kJ/m}^3$ . The impact of shape anisotropy can be estimated from the sample geometry. The demagnetization factors for rectangular ferromagnetic prisms are given in Ref. [2]. For typical sample dimensions used in SQUID measurements (lateral size on the order of mm, film thickness up to some 100 nm) it is appropriate to approximate the sample as an infinitely extended plane. The shape anisotropy constant obtained this way  $K_{\text{ani}}^{\text{plane}} = \mu_0/2 \cdot M_s^2 = 190 \text{ kJ/m}^3$  is equivalent with the value derived from the data of Fig. 2.5. Thus the magnetometry measurements of MnAs on GaAs(001) reveal the easy plane character of the magnetocryst-

talline anisotropy of bulk MnAs. Deviations from this value due to the strain in the film are small and will be, to first order, neglected.

**MnAs/GaAs(111)B:** In contrast, for MnAs layers grown on GaAs(111)B the hexagonal plane of MnAs lies in the film plane. The strain due to the epitaxial constriction is now isotropic and its influence on the phase transition is stronger compared to MnAs on GaAs(001). This is due to the fact that the basal plane is now completely clamped and not partially linked to the substrate, resulting in a wider phase coexistence regime which is additionally shifted to higher temperatures [59, 78]. A disappearance of magnetization at  $T_h \approx 50^\circ\text{C}$  and a phase fraction of  $\phi = 0.8$  at room temperature are reported [78]. Small amounts of  $\beta$ -MnAs could be identified even at temperatures  $T_l \approx 10^\circ\text{C}$  [21].

It is difficult to determine the lateral arrangement of the two phases. In AFM, a network of hexagonal structures is visible, showing a height modulation above 5 nm. However, it is known that bulk MnAs shows almost no change in the  $c$  lattice constant over the phase transition. Thus a significant height difference between the two phases in the film cannot be expected and

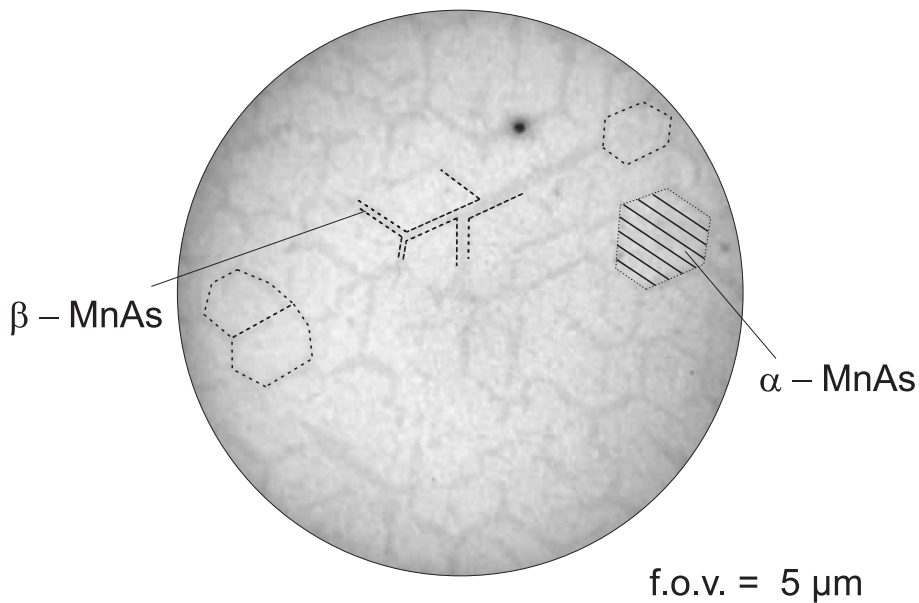


Figure 2.6: LEEM image of a 300 nm thick MnAs layer on GaAs(111)B at room temperature.  $\beta$ -MnAs (thin dark lines) formed a network, separating large areas of polygonally shaped  $\alpha$ -MnAs islands (bright). Electron energy: 14.5 eV, field of view (f.o.v.) 5  $\mu\text{m}$  in diameter [10].

the observed surface corrugation is most likely due to growth-related effects.

From chemical wet etching experiments on MnAs/GaAs(001) it is known [135] that  $\alpha$ - and  $\beta$ -MnAs have different etch rates. This property of MnAs is used to visualize the distribution of the two phases for MnAs films on GaAs(111)B [136]. The arrangement of the two phases agrees very well with the structure obtained by LEEM imaging shown in Fig. 2.6. The structure consists of  $\alpha$ -MnAs islands having a polygonal shape originating from the three-fold symmetry of the crystals, separated by a honeycomb-like network of  $\beta$ -MnAs.

The hysteresis loops measured on MnAs films on GaAs(111)B also differ in comparison to films on GaAs(001). Now, the basal plane is in the film plane and the observed behavior along the  $[11\bar{2}0]$  and  $[1\bar{1}00]$  directions reveals the magnetic isotropy in the film plane. The hysteresis curves are rounded and the remanent magnetization is smaller than the saturation magnetization. MnAs on GaAs(111)B demagnetizes at remanence by the formation of domains. For the out-of-plane magnetization, both effects, shape anisotropy and magnetocrystalline anisotropy, add up. The saturation field is the sum of demagnetizing and anisotropy fields: for a magnetocrystalline anisotropy field of 2 T and a saturation magnetization of  $M_s = 700$  kA/m [see Fig. 2.7(a)] the saturation field is then close to 3 T.

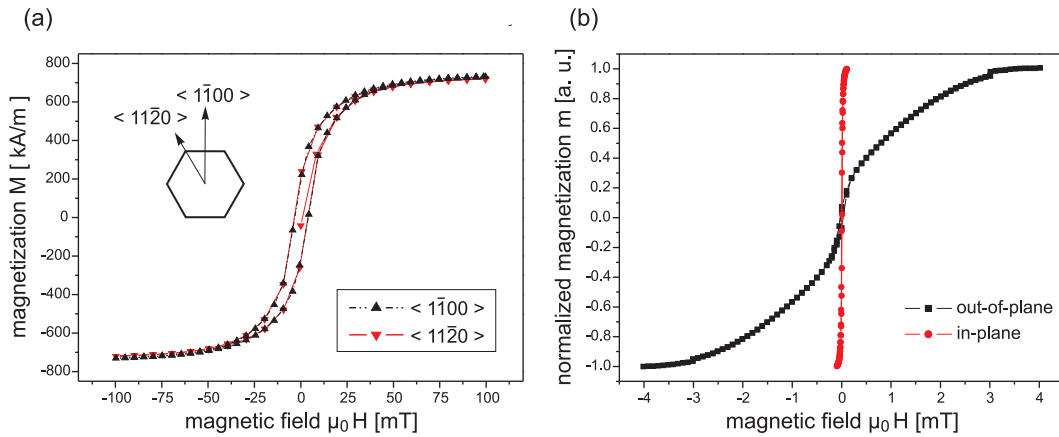


Figure 2.7: (a) Magnetization curves for a 650 nm thick MnAs film on GaAs(111)B. The field is applied in the film plane along two different directions. The red and black curves represent fields applied along  $[11\bar{2}0]$  and  $[1\bar{1}00]$ , respectively. (b) Comparison of the magnetization curves of a MnAs film/GaAs(111)B for a field applied in the film plane (red curve) and normal to the film plane (black).

In summary, the different epitaxial constraints induced by the substrate orientation, give rise to a unique interplay of elastic properties in the heterostructures. The formation of a self-organized pattern of  $\alpha$ - and  $\beta$ -MnAs arises, reflecting the symmetry of the strain state. The boundary between the two phases is oriented perpendicular to the stress direction. The integral magnetic properties measured by SQUID reveal a strong magnetocrystalline anisotropy, which impedes the magnetization along the  $c$ -axis. For MnAs/GaAs(001), the shape anisotropy interferes with the planar magnetocrystalline isotropy, resulting in an easy axis character of the film along the in-plane  $a$ -axis. For MnAs/GaAs(111)B, the planar magnetocrystalline isotropy is not altered by the shape anisotropy since the basal plane is in the film plane.

# Chapter 3

## Experimental Techniques

The primary goal of a magnetic imaging technique is to provide a spatially resolved picture of the magnetization distribution  $\mathbf{M}(\mathbf{r})$  throughout the sample. Knowing the magnetic structure is at the heart of understanding the magnetic properties. An ideal magnetic imaging technique should allow high-resolution imaging, both laterally and as a function of depth, fast imaging to follow magnetization dynamics, imaging in an external field environment, imaging magnetic devices where magnetic structures are buried under non-magnetic overlayers and imaging without disturbing the magnetic structure.

To determine the magnetic properties of MnAs films on GaAs, the results obtained from different measurement techniques were taken into consideration. The macroscopic magnetic properties were determined with SQUID and the micromagnetic properties using MFM and XMCDPEEM. The latter two are magnetic domain observation methods exhibiting a comparable lateral submicron resolution, however, they are complementary due to the different origin of the measured signal. On the one hand, the surface magnetization and magnetic domains of the sample can be directly visualized with XMCDPEEM. Together with SQUID, this allows for a quantitative mapping of the magnetization in thin films. On the other hand, MFM exhibits a large information depth on the order of the working distance. Unfortunately, instead of measuring the magnetization directly, the stray field originating from the magnetization distribution is imaged. The micromagnetic measurements are supported by quasi-simultaneous topographical methods: MFM with AFM and XMCDPEEM with LEEM, respectively.

In this Chapter, an overview of the experimental methods for the determination of the magnetic properties will be presented.

### 3.1 SQUID

Commercial SQUID magnetometry [109] was used to measure the integral magnetic properties. The samples were mounted on a sample rod, which is equipped with a temperature control ranging from 2 K to 400 K. The sample was placed in the magnetic field of a 5 T superconducting magnet. Pickup coils detect the magnetic field originating from the magnetic moment of the sample and the shielded SQUID detector converts the change of the magnetic flux to a voltage signal.

The experimental setup of the SQUID allows the measurement of the magnetic moment of a sample as a function of external magnetic field, depending on its orientation in the field and as a function of temperature. The absolute magnetization values can be determined knowing the volume of the sample whereby the measurement of the film thickness is the main source of error. Although the cross-section of the sample was measured by scanning electron microscopy (SEM), fluctuations in the observed layer thickness due to the cleaving amount to about 10%.

### 3.2 XMCDPEEM

XMCDPEEM is a relatively new technique that combines X-ray absorption spectroscopy and electron microscopy. First successful measurements have been performed in 1987 [126]. The contrast formation originates from the difference in X-ray absorption coefficient depending on the relative orientation of photon helicity and magnetization. The secondary electron yield is proportional to the absorption coefficient and the emitted electrons are detected in PEEM. The reason for the relatively late facilitation of the magnetic dichroism effect in case of soft X-ray absorption are the demands on the X-ray source. Very high intensities of monochromatic X-rays are needed, where the photon energy can be tuned and the polarization of the flux can be controlled. Only synchrotrons can fulfill these demands.

The physical origin of magnetic dichroism in soft x-ray absorption is the spin-dependence of the combined effects of spin-orbit coupling and exchange splitting of the valence states. Optical excitations are governed by the dipole selection rules. Applying these rules to the transition from core levels with spin-orbit splitting to final states with exchange splitting yields the qualitative features of magnetic dichroism.

The basic principle of XMCD can be explained with a simple two-step model of excitation and transition for 3d transition metals, as illustrated

in a one-electron picture in Fig. 3.1. First, the photoelectrons are excited from the initial states of the 2p core level of Mn, which is split into two levels due to the spin-orbit interaction:  $L_3$  ( $2p_{3/2}$ ) and  $L_2$  ( $2p_{1/2}$ ) with total angular momentum  $j = 3/2$  and  $j = 1/2$ . In the  $L_3$  state, spin and orbital momentum couple parallelly ( $j = l + s$ ) — in the  $L_2$  state antiparallely ( $j = l - s$ ) — to each other. The dipole selection rules are:  $\Delta j = 0, \pm 1$ ,  $\Delta l = \pm 1$ ,  $\Delta m = +1$  for left and  $\Delta m = -1$  for right circular polarized photons, respectively. The helicity of circularly polarized light is defined to be parallel (right) or antiparallel (left) to the X-ray propagation direction,

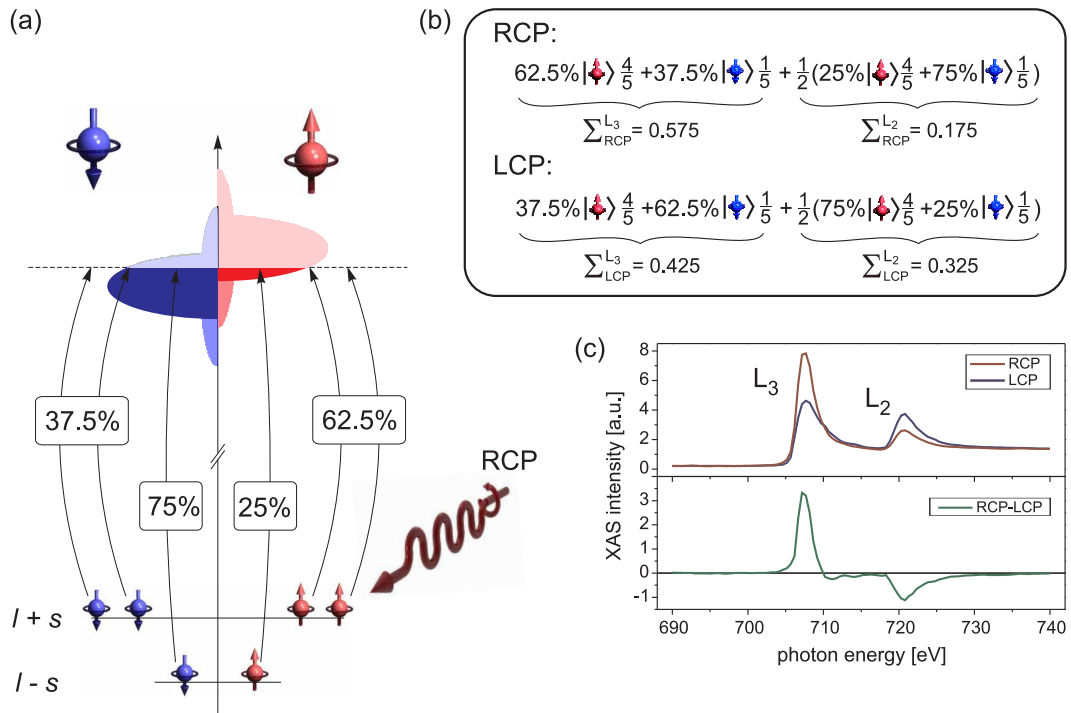


Figure 3.1: (a) Principles of magnetic circular dichroism in absorption at the  $L_{2,3}$  edge. Schematic absorption and transition probabilities for right circularly polarized light (RCP) that preferably excites spin-up electrons out of  $L_3$  and spin-down electrons out of  $L_2$ . (b) Calculation of the transition probability for RCP and left circularly polarized light (LCP) assuming an occupancy of majority and minority spin bands to be  $4/5$  and  $1/5$ . Since spin flips are forbidden, the measured resonance intensity directly reflects the number of empty  $d$  band states of a given spin. (c) X-ray absorption spectra (XAS) for the different helicity signals and the XMCD spectra, here exemplary shown for Fe [132].



thus photons carry an angular momentum of  $+\hbar$  and  $-\hbar$ , respectively [131]. The excitation of the initial  $p$  electrons into the  $s$ -band ( $p \rightarrow s$ ) are of minor importance, since the transition probability and the density of states above the Fermi level is smaller as compared to a  $p \rightarrow d$  transition<sup>1</sup>. The transition probabilities for the  $p \rightarrow d$  transition can be calculated using Fermi's Golden Rule. The spin polarization depends on the absorption edge and on the polarization of the light. They are higher for electrons with an orbital angular momentum parallel to the light helicity of the photon. For right-polarized photons (RCP), photoelectrons with spin-up are preferentially excited from the  $2p_{3/2}$  level (62.5%) and with spin down from the  $2p_{1/2}$  level (75%) [56], since the levels have parallel and antiparallel spin-orbit coupling  $l + s$  and  $l - s$ , respectively. This is shown in Fig. 3.1(a).

The magnetic properties enter in the second step. The spin polarization of the excited photoelectrons is revealed only in case of an imbalance for the spin-up and spin-down density of states in the  $3d$  valence band. Since spin flips are forbidden in dipole transitions, photoelectrons with spin-up (down) from the  $p$  core shell can only be excited into spin-up (down)  $d$  hole states. The  $3d$  valence band acts as a "spin-detector" of the spin-polarized photoelectrons and the transition intensity (and thus the absorption) is the product of the spin-dependent transition probabilities and the number of empty  $d$  states of a given spin. This is schematically illustrated in Fig. 3.1(a) and (b), where the number of unoccupied spin-up states at the Fermi level is larger than for the spin-down states. Therefore the absorption of RCP light will be enhanced at the  $L_3$  edge and reduced at the  $L_2$  edge. The opposite effect occurs for LCP light. This difference in the absorption is the X-ray magnetic circular dichroism effect and it is quantitatively related by sum rules to the magnitude of spin and orbital magnetic moments [17, 146].

The XMCD absorption spectra and the XMCD signal for both helicities are shown in Fig. 3.1(c). In XMCD spectroscopy it is equivalent whether the photon polarization is changed and the magnetization is kept fixed or whether the magnetization direction is changed and the helicity remains fixed.

PEEM can be used to image magnetic domains based on the polarization-dependent X-ray absorption. The difference in absorption coefficient can be measured and imaged through the detection of the secondary electrons, which is well suited for this purpose, as no polarization analysis, energy selection or directional selectivity is necessary. The schematic setup of an PEEM is shown in Fig. 3.2(a). Auger electrons are generated by radiationless recombination process of X-ray-excited atoms, that originate secondary electrons

---

<sup>1</sup>In practice, the  $p \rightarrow d$  channel dominates by a factor of  $> 20$  [28])

from inelastic scattering. A large secondary electron intensity is a direct measure of the X-ray absorption coefficient of the sample and provides a suitable large PEEM signal [132]. The sampling depth, as illustrated in Fig. 3.2(b), is determined by the cascading process of the scattered Auger electron and is on the order of a few nanometers. The electron signal originates close to the sample surface, as only secondary electrons escaping from the surface can contribute to the detected yield. The emitted electrons are projected with magnification onto a screen and the spatial resolution is determined by the electron optics within the microscope.

In XMCDPEEM, contrast also arises from the surface topography and differences in the local work function. The electric field is distorted at surface topographical features, leading to a distortion of the electron trajectories causing ridges to appear darker and grooves brighter than flat regions. In

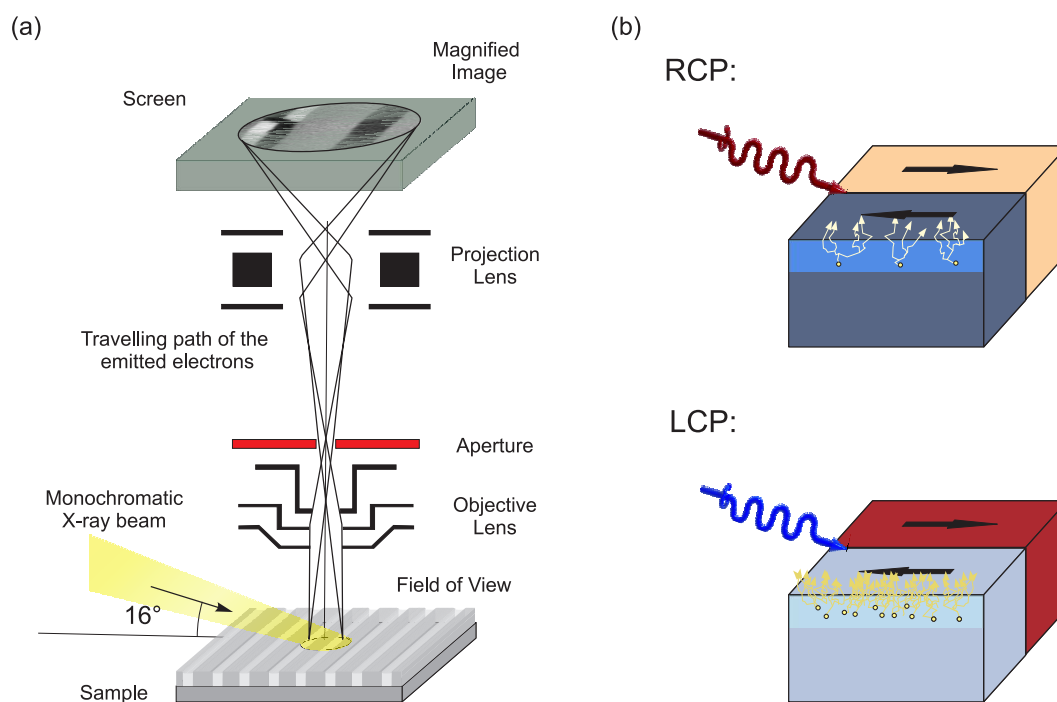


Figure 3.2: (a) Schematic of PEEM imaging technique [133]. (b) Resultant XMCD contrast of the  $L_3$  absorption edge for domains with magnetization parallel and antiparallel to the incident photon beam for two different helicities, leading to a strong absorption (bright), when the photon spin direction and the spin quantization axis are parallel. Additionally, the cascading effect from the emitting centers of the Auger electrons is indicated.

order to eliminate the additional topographical contrast, XMCDPEEM images of the same spot are recorded with opposite photon helicity and then subtracted. This way the helicity-independent structural contrast is removed and the resulting difference image contains only helicity-dependent magnetic contrast. The difference of the absorption probabilities of the  $2p_{3/2}$  level for different magnetization and circular polarizations are shown in Fig. 3.2(b).

The measurements have been performed at the 'Nanospectroscopy' beamline of the synchrotron ELETTRA in Trieste [29]. The layout of the beamline is described in Ref. [71]. A Sasaki APPLE-II type undulator serves as source of spin-polarized photons. It takes about 30 seconds to reverse the polarity of the photon beam. After passing a pinhole and mirrors, the emitted X-ray

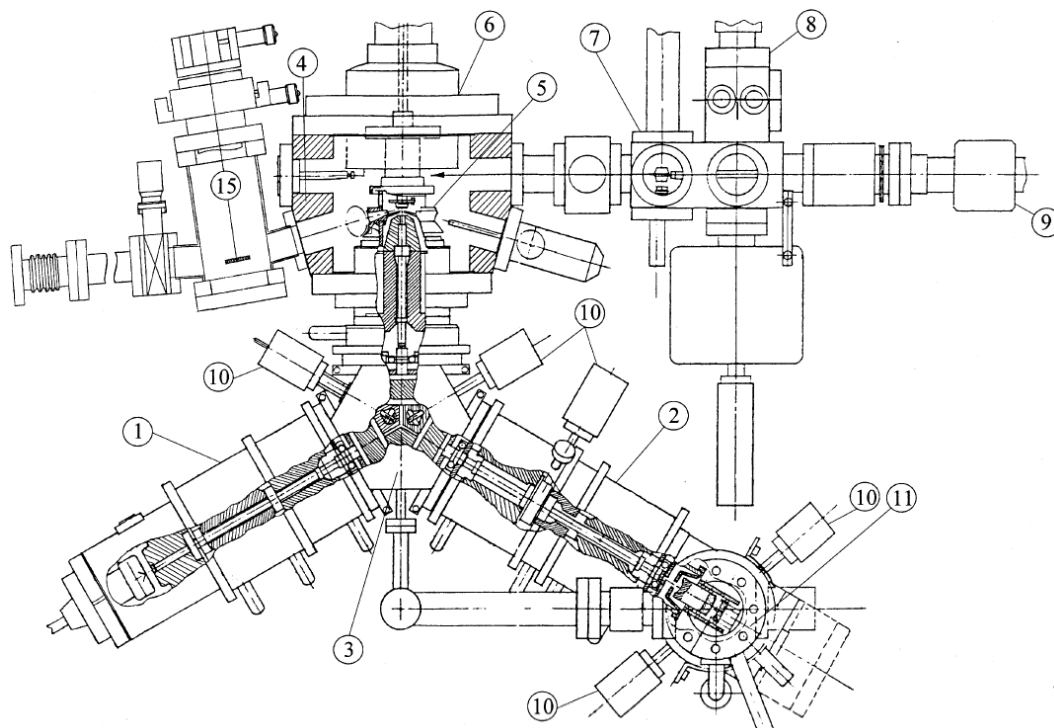


Figure 3.3: Schematic of the SPELEEM: (1) electron gun, (2) image column, (3) magnetic beam separator, (4) specimen rod, (5) magnetic objective lens, (6) sample manipulator, (7) preparation chamber, (8) air lock, (9) transfer rod, (10) illumination, selected area and contact aperture, as well as energy slits, (11) analyzer, (15) soft X-ray refocussing mirror. The picture is taken from Ref. [122].

light is dispersed by a monochromator and reflected by a refocussing mirror into the specimen chamber of the SPELEEM [123]. The light illuminates the sample at a grazing incidence angle of  $16^\circ$ .

The geometry of the SPELEEM setup is shown in Fig. 3.3 [122]. The microscope combines LEEM [9] and energy filtered XPEEM [8] operation modes, as the imaging column hosts a hemispherical electron energy analyzer. For XMCDPEEM imaging, the sample is illuminated by a monochromatic X-ray beam with a photon energy of 639.5 eV, which is moderately focussed such that it matches the maximum field-of-view (f.o.v.) of the photoelectron microscope. The energy corresponds to the  $L_3$  absorption edge of Mn which is chosen to map the X-ray absorption, because the maximum dichroitic effect for two different helicities is observed if electrons from the Mn  $2p_{3/2}$  core level are excited and the photon spin direction and the spin quantization axis are collinear (typically 20%). The spatial orientation of the spin quantization axis is given by the sample magnetization  $\mathbf{M}$  (majority spin antiparallel, minority spin parallel). The sample is oriented such that the direction of incident light from the X-ray source is oriented along the easy  $a$ -axis of MnAs. The emitted electrons traverse the image column and the energy analyzer and are projected onto a screen. The energy analyzer is used as an energy filter, which leads to a reduction of chromatic aberrations induced by the broad inelastic secondary electron peak spoiling the lateral resolution [133]. The kinetic energy of the transmitted electrons is limited to 5 eV. In LEEM mode, the electrons generated and collimated in the illumination system, and deflected by the magnetic beam separator are decelerated in front of the specimen from 18 keV to a kinetic energy of 4.5 eV. After reflection from the surface the electrons are reaccelerated to 18 keV, and are now deflected by the beam separator into the image column. Finally, they are transferred via the energy analyzer into an image on the screen.

For transporting the samples to the beamline, the MnAs films were capped with a 300 nm thick As layer. They were heated to  $\sim 325^\circ\text{C}$  in the preparation chamber. After the complete desorption of the arsenic cap low energy electron diffraction (LEED) patterns of MnAs  $(\bar{1}100)$ - $(1 \times 2)$  were obtained.

Figure 3.4 shows an example of the topographic (LEEM) and the corresponding XMCD contrast of a 500-nm-thick MnAs film on GaAs(001). Both images clearly exhibit the two-phase stripe structure of MnAs films. The domains in the ferromagnetic stripe are clearly visible in the XMCDPEEM image. The contrast in the difference image corresponds to a magnetization collinear with the direction of incident light. The gray contrast originates from  $\beta$ -MnAs. Since no exchange splitting is apparent, the transition proba-

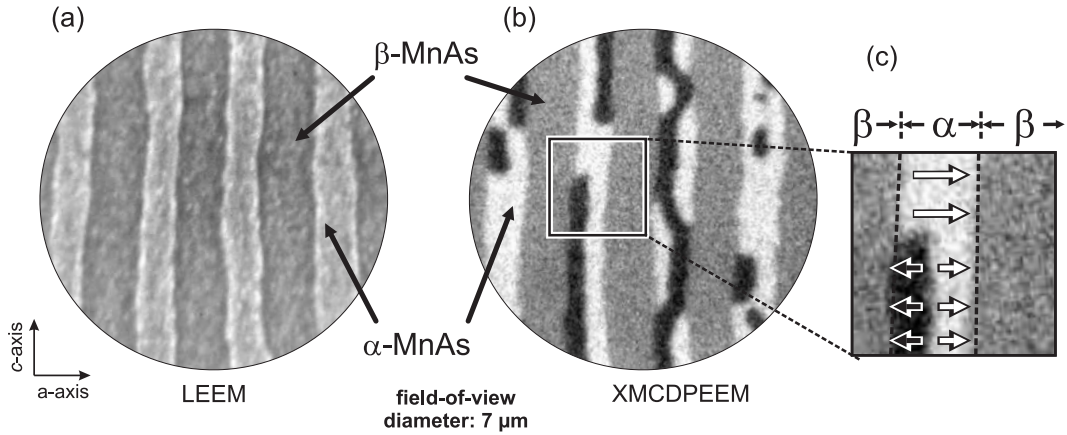


Figure 3.4: LEEM (a) and XMCDPEEM (b) image of the topography and the magnetic contrast, respectively, of a 180-nm-thick MnAs film on GaAs(001). The XMCDPEEM image contains additional information of the magnetization component of the topmost surface, parallel to the incident photon beam. The ferromagnetic stripes ( $\alpha$ -MnAs) are separated by non-ferromagnetic areas of  $\beta$ -MnAs (grey, i.e. no magnetic contrast). The direction of magnetization and photon wave vector of incident light and the magnetization direction on the ferromagnetic stripes, represented by arrows, is illustrated in (c). It shows that the stripe magnetization is either parallel or antiparallel to the  $a$ -axis of the sample. Field-of-view diameter:  $7 \mu\text{m}$ . Temperature  $T = 35^\circ\text{C}$ .

bility is helicity-independent, causing a gray contrast in the difference image. A gray contrast in the ferromagnetic stripes has also been observed. This can be attributed to a domain flip during the measurement, as reversing the helicity of the photon source takes about 30 seconds.

### 3.3 MFM

The magnetic force microscope (MFM)[76, 114] is a variant of the scanning force microscope family capable of recording the magnetostatic force, or the force gradient, between a magnetic tip and a magnetic sample. The advantage of this technique is that it works in ambient condition and no special sample preparation is needed. However, the interpretation of the measured signal is not straightforward, since MFM does not directly monitor the magnetization distribution but the stray field emanating from the sample. Additionally, the magnetic tip can distort the magnetization of the sample. Nevertheless, MFM is the most commonly used imaging technique

due to its easy implementation and low cost.

In this section, an overview of the technique as well as simulations of the MFM contrast will be presented. Furthermore, the extension of the conventional MFM technique by an external magnetic field setup is described.

### 3.3.1 Principle and modes of operation

Several different techniques have been developed to detect the magnetic interaction between tip and sample. There are two modes of MFM operation: static MFM, where the interaction force is measured through the deflection of the cantilever, and dynamic MFM, where the change in the resonant properties of the cantilever is registered. All experiments have been performed in dynamic mode, as it offers the advantage of a higher sensitivity and a lower signal-to-noise ratio compared to the static mode when measuring long range forces, like magnetic interaction [47]. The discussion is solely restricted to the dynamic operation mode, which is responsive to force gradients, as will be shown below. The common setup of an MFM is shown in Fig. 3.5.

In MFM, the cantilever and thus the tip is coated with a magnetic layer. The cantilever is excited to oscillate close to its resonance frequency by a

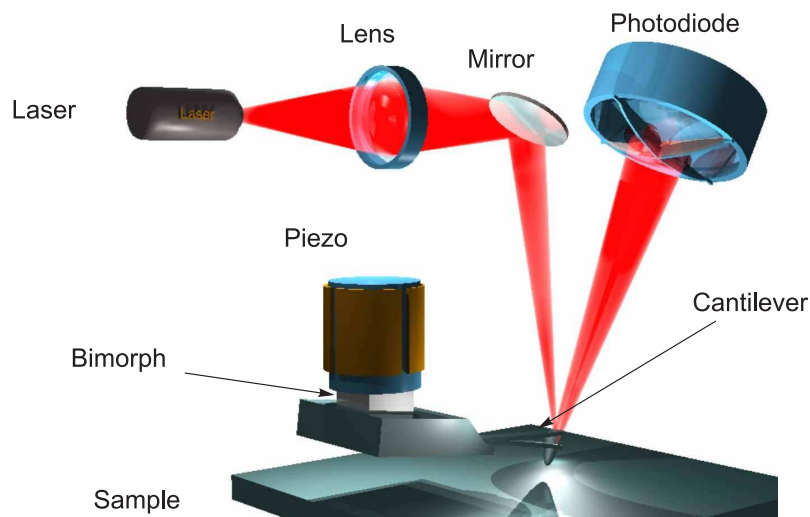


Figure 3.5: Common MFM setup. The cantilever is excited to oscillate close to its resonance frequency by a piezo bimorph. The cantilever deflection is measured by a laser beam reflected onto a split photodiode. The difference of the light intensities in the sectors gives access to the vertical deflection of the tip.

piezoelectric bimorph with a given amplitude  $A_d$  and frequency  $\omega_d$ . To detect the deflection of the cantilever motion, and hence the force gradient, the movement of the reflected laser beam onto a photosensitive detector is measured. The deflection can be detected with a resolution of  $< 1\text{\AA}$ . The image is obtained by raster-scanning the cantilever across the sample and recording the change in the cantilever oscillation due to tip-sample interaction.

The motion of the cantilever beam can be modeled as an one-dimensional damped, driven harmonic oscillator with quality factor  $Q$ , spring constant  $k$  and effective mass  $m$ , exhibiting a resonance frequency  $\omega_0 = \sqrt{k/m}$ . The free oscillation of the cantilever suffers a perturbation in a force field. The tip-sample interaction can be treated as a spring in series with the cantilever. An attractive force, and thus a positive force gradient ( $F' > 0$ ), will make the cantilever spring softer. The effective spring constant of the cantilever can be written as:

$$k_{\text{eff}} = k - F' . \quad (3.1)$$

The change in spring constant due to the force gradient causes a shift in the resonance frequency of the cantilever  $\omega_r = \sqrt{(k - F')/m}$ . In a linear approximation, the frequency shift can be written as:

$$\Delta\omega = \frac{\omega_0 F'}{2k} . \quad (3.2)$$

The amplitude and the phase shift with respect to the driven oscillation also vary linearly with the force gradient and can also be utilized to deter-

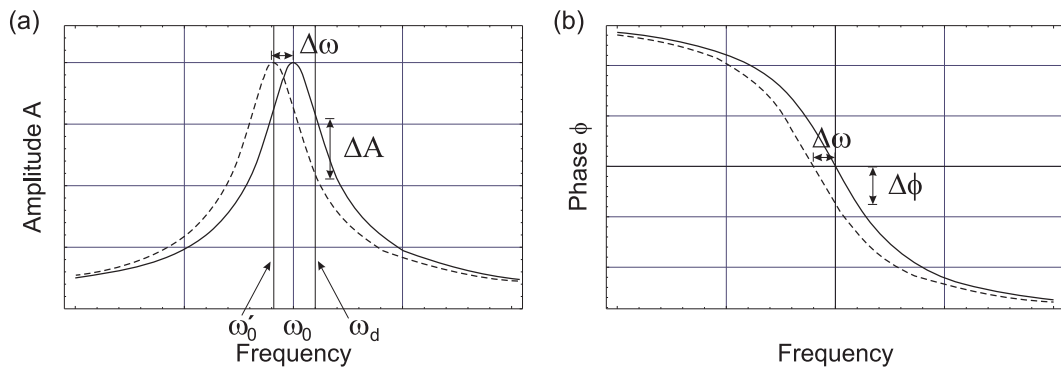


Figure 3.6: Force gradient detection techniques. The cantilever is driven at a fixed frequency  $\omega_d$ . A frequency shift causes changes in (a) the amplitude or (b) phase of the oscillation (slope detection method) [47]. The direct frequency shift can be obtained in a frequency modulation (FM) technique using a phase locked loop circuit (b).

mine the force gradient. The approximation of the linear response is only valid under the following assumptions: (1) the perturbation of the harmonic oscillation of the cantilever is very small, (2) the quality factor and therefore the damping of the cantilever oscillation is constant, (3) the tip-sample distance is constant, and (4) the oscillation amplitude of the cantilever is small compared to the decay length of the magnetic interaction. If the last condition is not fulfilled, the force gradient can be replaced by a weighted average of the force gradient over the amplitude [42].

Two different principles, the amplitude modulation (AM) and the frequency modulation (FM) mode, can be used to determine the force gradient, see Fig. 3.6 [5, 77]. The first detection scheme exploits the change in the oscillation amplitude  $A$ . If the cantilever is initially forced to vibrate at  $\omega_d > \omega_0$ , then a shift in the resonance spectrum of the cantilever towards lower frequencies due to an attractive interaction will cause a decrease in the oscillation amplitude. In the frequency modulation (FM) detection system, the cantilever serves as the frequency-determining component of a constant-amplitude oscillation. The phase relation between the drive signal and the cantilever oscillation can be kept constant by a phase locked loop (PLL) device and the cantilever is driven near its new resonance frequency. Thus, the cantilever frequency shift can be directly monitored.

Unfortunately, in addition to the magnetic tip-sample interaction, there are further interactions to consider, including the van der Waals interaction and electrostatic interaction. Thus, the change of the cantilever status cannot be directly attributed to the magnetic interaction. Instead, the total force gradient is determined as follows:

$$F'_{tot} = F'_{mag} + F'_{el} + F'_{vdW}. \quad (3.3)$$

It contains additional features of topographic and electrostatic origin. To minimize these unwanted influences, the tip should be positioned at a height where the magnetic interaction dominates over the other interactions. However, for stable imaging the total force gradient has to be monotonic. Since magnetic interactions can either be attractive or repulsive, an additional force gradient is needed to stabilize the feedback and to ensure loop stability. According to Eq. 3.3, van der Waals interaction or the electrostatic interaction can be used for the purpose of a 'servoing force', which has to be larger than the strongest magnetic interaction. Unwanted contributions from the topography and the electrostatic interaction have to be taken into consideration in MFM imaging.



To generate an image, the MFM can be operated in constant frequency shift mode and in tapping-lift mode, see Fig. 3.7 [47]. In the constant frequency shift mode, the image is acquired by maintaining the cantilever status adjusting the tip-sample separation. The tip-sample distance is increased over regions of magnetic attraction and reduced over regions of magnetic repulsion. The scanning speed is chosen slow enough so that the servo loop can fully respond to the changes in the interaction. Thus, the contours of the total force gradient are measured and the tip-sample distance is the information signal. However, this signal also depends on the force distance curve of the servoing force. To reduce interference effects of force gradient contributions from magnetic and servoing interaction, the signal should be independent of position and the servoing interaction much larger than the magnetic interaction. This ensures a response independent of the force distance properties of both contributions. Usually the electrostatic interaction is utilized. However, experiments applying a dc voltage between tip and sample have revealed that the measured response contains other artifacts, which are caused by the difference in conductivity of  $\alpha$ - and  $\beta$ -MnAs. The use of the van der Waals force is advantageous since its contribution to the total force gradient is known from independent AFM topography measurements. However, using the van der Waals force, which is relatively weak and short range, the advantage of a larger servoing force is lost and the magnitudes of both contributions are comparable. The resulting response is nonlinear and

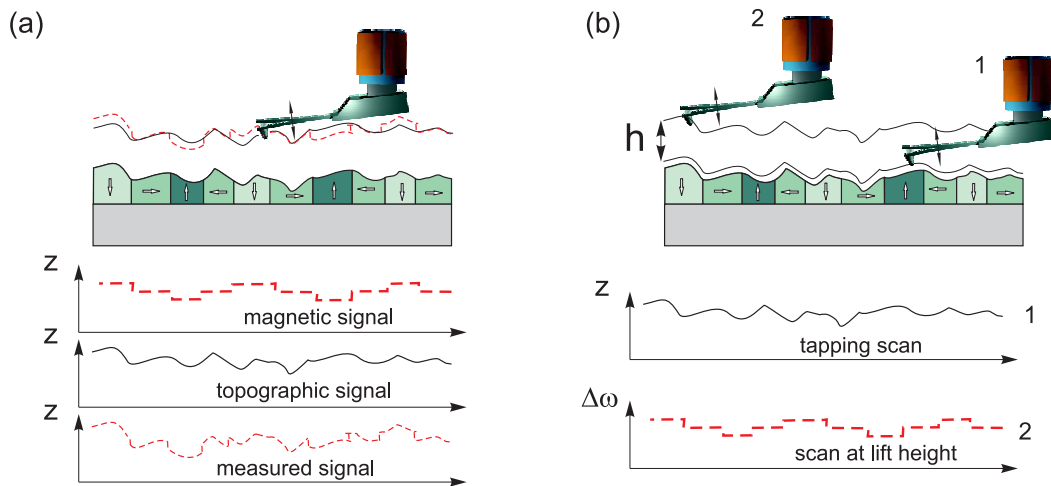


Figure 3.7: (a) Schematic of the constant frequency shift mode. The resulting scan is a convolution of topography and MFM interaction. (b) Illustration of the lift-mode operation. In a first scan (1) the sample topography is measured, while the lift scan follows at elevated height  $h$ .

can lead to asymmetric imaging due to magnetic force derivatives of opposite sign. The obtained image will certainly be a convolution of magnetic contrast with topography, since the height modulation of the stripe structure additionally irritates the measured signal.

In tapping/lift mode [see Fig. 3.7(b)], the topography and the contrast can be separated. In a first scan the sample topography is obtained in tapping-mode using the cantilever oscillation amplitude as a feedback signal. In a subsequent scan the magnetic contrast is obtained in lift-mode monitoring the cantilever frequency or phase shift upon re-scanning the previously measured topography at an elevated height. This technique ensures a deconvolution of magnetic and topographic interaction. In tapping/lift mode MFM the results can be corrupted by drifts during data acquisition. Additionally, during the first tapping scan, the stray field of the MFM tip can induce a substantial distortion of the magnetic structures of the sample.

### 3.3.2 Theoretical consideration of the MFM response

The MFM response, i.e. the response due to the magnetic interaction between tip and sample, enables in many cases for a qualitative characterization of the micromagnetic properties of a sample, like the hard [46] or soft magnetic [73] properties, or even the determination of the nature of domain walls as Bloch- or Néel-like [94, 108].

The quantitative interpretation of MFM results, on the other hand, is a challenging task. The magnetic interaction force between the tip and the sample,  $\mathbf{F} = -\nabla E_{t-s}$ , is determined by the convolution of the tip magnetization  $\mathbf{M}_{\text{tip}}$  with the sample stray field  $\mathbf{H}_s$ :  $E_{t-s} \sim \int_{\text{tip}} \mathbf{M}_{\text{tip}} \mathbf{H}_s$ . In case of mutual non-disturbance of tip and sample magnetization, the convolution of the sample magnetization  $\mathbf{M}_s$  and tip stray field  $\mathbf{H}_{\text{tip}}$  yields the same result and, by knowing the precise tip stray field, one can, in principle, determine the sample magnetization  $\mathbf{M}_s$ . The first problem arises as different magnetization patterns will lead to the same stray field at a certain distance above the sample [151].

The second problem is related to the magnetic probe in MFM. As the measured response is governed by the tip properties which are usually not known in detail [1], some effort has been dedicated to develop suited calibration standards for MFM tips [43, 66]. A few attempts have been made to measure the magnetic stray field of the tip by electron holography [134], Lorentz microscopy [79, 127], and micro Hall probe measurements [145]. Also, the magnetization distribution of the tip has been calculated, assuming the tip as a two-dimensional triangular structure [100] and based on a three-dimensional model [148]. Nevertheless, it has to be noted that the calibration of the tip is

laborious to obtain and, furthermore, the tip properties are difficult to maintain in the experiment. Beyond this effort, MFM tips are known to influence the magnetic structure of the sample under investigation, which was a basic assumption for the extraction of the sample magnetization above [94, 160].

Due to the complexity of the problem, practical MFM simulations are based on a number of approximations mainly concerning a realistic tip magnetization. Common approaches are the point dipole model [49], the ellipsoidal dipole model [67] and the magnetic charge model [79]. More advanced tip models involve a spherical apex and a conical taper [113], a conically shaped tip [52], a nonmagnetic truncated cone covered by a thin magnetic layer [101], and a discretized probe [100], which are applied to samples with rather simple and well-known stray fields. For calculating the MFM response and resolution of samples with periodic magnetization features, such as recording media, a Fourier transform approach was introduced for obtaining the sample stray field [54, 104]. For more complex situations, i.e. for non-periodic magnetization distribution where every magnetic sample charge has to be Fourier transformed and for films with a magnetization distribution in depth, the method loses its advantages. The problem of the tip influence on the sample magnetization has been addressed in the framework of micromagnetism, where the tip was treated as an effective monopole [40]. The proper approach, however, relies on time-consuming iterative energy minimization techniques. The magnetization state with the lowest energy, taking into account exchange, anisotropy, and magnetostatic energies, represents the equilibrium magnetization state of the MFM tip [75] and the sample.

The force density  $\mathbf{f}$  acting on a magnetization  $\mathbf{M}_{\text{tip}}$  in the stray field of the sample  $\mathbf{H}_s$  is given by  $\mathbf{f} = \mu_0 \cdot \nabla (\mathbf{M}_{\text{tip}} \cdot \mathbf{H}_s)$  and simplifies in the case of mutual non-disturbance to:

$$\mathbf{f} = \mu_0 (\mathbf{M}_{\text{tip}} \cdot \nabla) \mathbf{H}_s . \quad (3.4)$$

Since MFM is based on dynamic force microscopy, the force gradient of the magnetic interaction has to be calculated. The component of the force gradient that alters the status of cantilever motion is the one normal to the cantilever [113]

$$F' = \frac{dF_n}{dn} = \mathbf{n} \cdot \nabla (\mathbf{n} \cdot \mathbf{F}) . \quad (3.5)$$

For the following discussion of the force gradient, only the normal derivative  $d/dn$  of the normal component  $\mathbf{F}_n$  of the total tip-sample interaction force is considered:

$$F'_n(\mathbf{r}) = \frac{d\mathbf{F}_n}{dn} = \mathbf{n} \cdot \nabla_{\mathbf{r}} (\mathbf{n} \cdot \mathbf{F}_{\text{tot}}(\mathbf{r})) , \quad (3.6)$$

where  $\mathbf{n}$  is collinear with the oscillation direction of the cantilever [76, 113].

The total magnetic interaction between sample and tip is given by the convolution of the magnetic field emanating from the sample  $\mathbf{H}_s$  and the magnetization of the tip  $\mathbf{M}_{\text{tip}}$ , leading to a total force:

$$\mathbf{F}_{\text{tot}}(\mathbf{r}) = \mu_0 \int_{\text{tip}} (\mathbf{M}_{\text{tip}}(\mathbf{r}') \cdot \nabla_{\mathbf{r}}) \mathbf{H}_s(\mathbf{r} - \mathbf{r}') d^3\mathbf{r}' . \quad (3.7)$$

By inserting Eq. 3.7 in Eq. 3.6, the force gradient can be written as:

$$F'_n(\mathbf{r}) = \mathbf{n} \cdot \nabla_{\mathbf{r}} \left( \mathbf{n} \cdot \mu_0 \int_{\text{tip}} (\mathbf{M}_{\text{tip}}(\mathbf{r}') \cdot \nabla_{\mathbf{r}}) \mathbf{H}_s(\mathbf{r} - \mathbf{r}') d^3\mathbf{r}' \right) . \quad (3.8)$$

A careful discussion of Eq. 3.8 is important for interpreting the simulations. For simplification, the normal vector is related to the surface of the sample as  $\mathbf{n} = \mathbf{e}_z$ . Then, only the  $z$ -component of the total force gradient contributes to the frequency shift. That simplifies Eq. (3.8) further, yielding:

$$F'_z(\mathbf{r}) = \mu_0 \int_{\text{tip}} \left( M_{z,\text{tip}}(\mathbf{r}') \cdot \frac{\partial^2}{\partial z^2} H_z(\mathbf{r} - \mathbf{r}') d^3\mathbf{r}' \right) \quad (3.9)$$

The assumption that  $\mathbf{n} = \mathbf{e}_z$ , and thus  $F' = \partial F_z / \partial z$ , neglects the tilt of the cantilever that is usually not avoidable in an experimental geometry. As a result, the experimental MFM contrast is asymmetric with respect to the line of zero force. However, as this effect is rather small, it will be neglected in our discussion [113].

**Model of the sample stray field:** Figure 3.8(a) shows a MFM scan of a 180-nm-thick MnAs/GaAs(001) film at room temperature. The magnetic contrast is located on the  $\alpha$ -stripes and it is dominated by a meander-like pattern extending along the stripe. The positions of the  $\alpha$ -stripes, obtained from the height modulation in the topography image, are indicated on the right-hand side. A closer look on the magnetic structure Fig. 3.8(b) reveals alternating bright areas at both ends of the ferromagnetic stripe (stretching along the  $c$ -axis direction). These areas are partially connected by narrower bright lines. The observed MFM contrast can be understood by assuming a

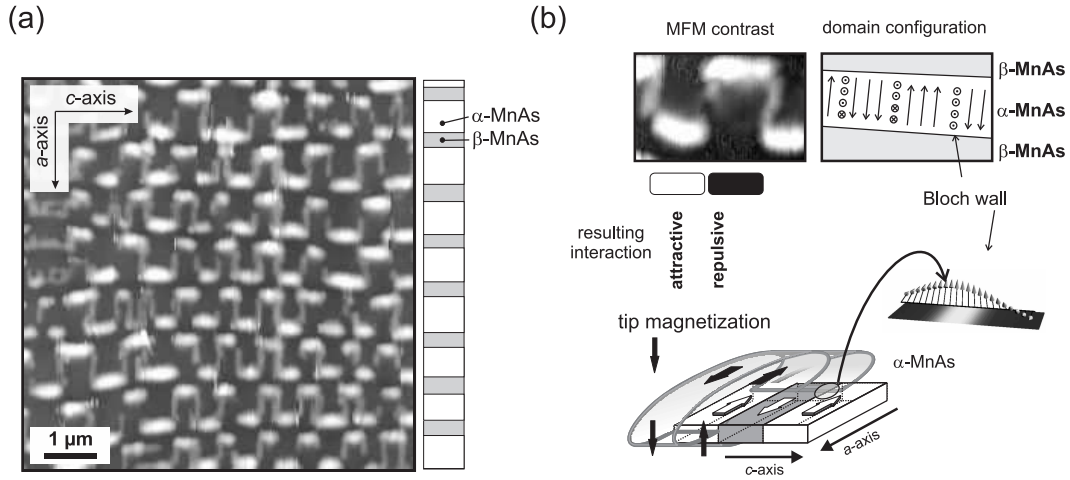


Figure 3.8: (a) MFM scan of a 180-nm-thick MnAs film at room temperature. (b) Micromagnetic domain structure and resulting stray field of ferromagnetic  $\alpha$ -MnAs stripes. The most likely domain configuration for the measured MFM image are modeled as a sequence of oppositely magnetized bar magnets separated by a  $180^\circ$  Bloch wall. An attractive (repulsive) magnetic interaction between the tip (magnetized along its axis) and the sample magnetization at the respective ends of the bar magnets results in dark (bright) MFM contrast.

sequence of alternately magnetized bar magnet-like domains (magnetization entirely along the easy  $a$ -axis), separated by  $180^\circ$  Bloch walls pointing into and out-of the sample plane [cf. Fig. 3.8(b)]. This assumption is justified as SQUID measurements revealed one easy magnetization direction along the  $a$ -axis, i.e. across the width of the stripe.

Figure 3.8(b) explains the contrast mechanism resulting from the interaction of the tip magnetization with the stray field of the domains. The magnetic stray field of the bar magnet-like domains will either point up (out-of the plane) or point down (back into the plane) at the end of the ferromagnetic stripe, as shown by arrows. The MFM is sensitive to the out-of-plane component of the stray field which interact with the tip magnetization (along the tip axis, cf. downward pointing arrow). The interaction between the tip and the stray field of the sample depends on the relative orientation of these two vectors. The parallel (antiparallel) orientation of the two magnetization vectors results in an attractive (repulsive) interaction, giving a bright (dark) contrast as shown in Fig. 3.8(b). Besides this contribution to the contrast, narrower dark and bright lines are also seen between two oppositely oriented domains. This is due to  $180^\circ$  Bloch walls where the magnetization vector ro-

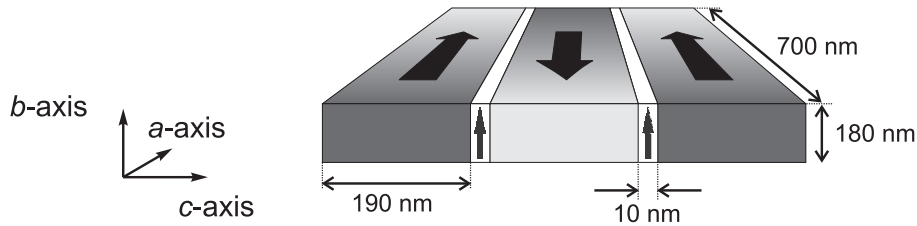


Figure 3.9: Model of the simulated domain structure.

tates through the surface normal direction (pointing out-of or into the plane) to reverse its direction between two oppositely magnetized in-plane domains. On the right-hand side of Fig. 3.8(b), the most likely domain configuration (including the orientation of the Bloch walls) is sketched that matches best the experimental image on the left.

The micromagnetic structure of the stripes in the film is modeled as an arrangement of bar magnets with a constant magnetization. Furthermore, it is assumed that the material is magnetically hard. In this model, the individual in-plane magnetized bar magnets are separated by out-of-plane magnetized bar magnets representing  $180^\circ$  Bloch walls. The dimension of the sample structure is given in Fig. 3.9. The calculation is based on the analytic expression of the stray field of uniaxial bar magnets [30]. In detail, the simulated structure has the following dimensions: width of the ferromagnetic stripe (along the  $a$ -axis): 700 nm, width of the individual domain (along the  $c$ -axis): 190 nm, film thickness: 180 nm, saturation magnetization: 800 kA/m. The Bloch walls, separating the in-plane domains, modeled as out-of-plane magnetized bar magnets with a thickness of 10 nm. These parameters are representative for room-temperature experiments on a 180-nm-thick MnAs film on GaAs(001).

**Tip model:** In general, the physical properties of the tip are influencing the MFM response (cf. Eq. 3.7). Consequently, the tip shape as well as the magnetic coating have to be treated in a suitable model. For simple sample stray fields, such as a single point dipole [52, 101], a direct integration over the tip is possible. For more complicated stray fields, e.g. the stray field of current-carrying lines[43, 44], parallel wires [64, 70, 157, 158], or rings [66, 72], the tip is modeled as a point dipole. In general, satisfactory qualitative agreement of the calculated and the measured curves is achieved. The position of the point dipole is usually within the real tip space and its position and the magnetic strength is a fit parameter [72]. In other words, the local magnetization of the tip coating is weighted by the stray field of the

sample at the respective positions and subsequently added. Due to the decay of the stray field with increasing distance from the sample, the position of the effective magnetization is at a distance  $z_{\text{eff}}$  away from the apex, inside the tip. The advantage of this model is that Eq. 3.8 simplifies to a multiplication of a function of the field  $\mathbf{H}_s$  with the monopole or dipole moment of the tip at the effective position  $z_{\text{eff}}$  (which is  $\delta z$  above the working distance  $z_0$ ). Numerical simulations based on this approach are very fast, however, the tip parameters  $z_{\text{eff}}$  and  $M_{\text{tip}}$  are physically unreasonable. The extreme simplification of the tip magnetization has two major disadvantages: (1) the tip geometry is omitted from the simulation, and, (2) reliable results are only obtained in the case that the investigated sample stray field shows the same decay behavior and a similar geometry as the tip stray field.

In order to obtain a quantitative model of the tip that is reliable, precise and easily applicable, only a few, experimentally accessible – and thus useful – parameters should be incorporated despite the increasing complexity. Consequently, the tip was modeled as a cone with an opening angle  $\gamma$ , terminated by a spherical apex (radius  $r$ , cf. Fig. 3.10). The two geometrical tip functions were continuously merged at the point where the cone touches tangentially the sphere (cf. Fig. 3.10). The magnetic properties of the coating are defined by its thickness  $\delta_{\text{tip}}$  and the remanent magnetization  $\mathbf{M}_{\text{tip}}^{\text{rem}}$ . The magnetic

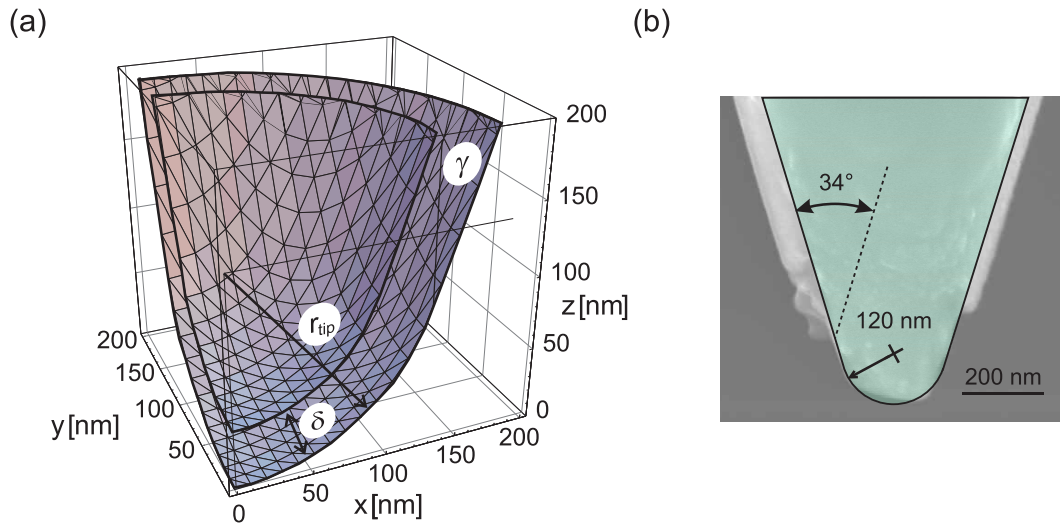


Figure 3.10: (a) Geometry of the modeled tip. (b) Scanning electron micrograph of a used MFM tip. The tip radius is  $r_{\text{tip}} = 120$  nm and the cone opening angle  $\gamma = 17^\circ$ . As the tip coating is partially worn of, its thickness can be determined to  $\delta = 20$  nm.

coating is further treated as a multi-shell structure of magnetic dipoles. All dipoles are oriented in the  $z$ -direction. Within this model, the influence of the four geometrical and magnetic properties on the MFM response can be systematically studied numerically as well as experimentally. Compared to the simple point probe approximation, a more computing-intensive treatment of Eq. 3.8 is necessary. On the other hand, the description of the magnetic stray field is valid for the entire half-space above the sample and no restrictions concerning the stray field geometry and its decay have to be taken into account.

**Simulation of the MFM response:** Based on the assumption that the tip magnetization is predominantly along the  $z$ -axis upon magnetization along its axis prior to the MFM experiments, we restrict ourselves to the treatment of the  $z$ -component of the magnetic field of the sample. It should be noted that, using the analytic expression given in Ref. [30], the second derivative of the stray field behaves well as we are only interested in the upper half-space above the sample. Furthermore, the divergences of the field at the corners of the bar magnet can be ignored, as the stray field is calculated sufficiently far away from these points. Now, the integral in the expression for the force gradient (Eq. 3.9) simplifies to the summation:

$$F'_z(\mathbf{r}) = \mu_0 \sum_{\text{tip}} \left( M_{z,\text{tip}}(\mathbf{r}') \cdot \frac{\partial^2}{\partial z^2} H_z(\mathbf{r} - \mathbf{r}') d^3\mathbf{r}' \right). \quad (3.10)$$

The  $(x,y)$ -plane is discretized introducing an equidistant step size  $\delta_s$ . Then, the values  $z_s(i \cdot \delta_s, j \cdot \delta_s)$  are calculated for the given tip geometry and an approximation for Eq. 3.8 is obtained:

$$F'_z(x, y, z) = \mu_0 \sum_{i,j} \left[ M_{z,\text{tip}}(x + i\delta_s, y + j\delta_s, z_s) \cdot \frac{\partial^2}{\partial z^2} H_z(x + i\delta_s, y + j\delta_s, z_0 + z_s) \right]. \quad (3.11)$$

The MFM response is further calculated from Eq. 3.11 requiring the tip and sample input parameters, as well as the tip-sample distance. The resulting force gradient leads, together with the cantilever parameters, to the MFM response. The detailed flow chart of the simulation procedure is depicted in Fig. 3.11(a).

The expenditure of time required for the calculation of the MFM response in a point above the sample depends on the rank of the involved matrices



and is thus a function of the sampling grid. In case of the tip matrix, its rank depends on the density and distribution of dipoles required for a sufficient sampling of the tip. This is, in turn, not only depending on the tip geometry but also on the decay length of the sample stray field. For practical calculations, a trade-off has to be made between the precision of the simulation and the computing time. In principle, starting from a measured MFM contrast, the experimental values of tip-sample distance  $z_0$  and oscillation amplitude  $A_d$  can be used as fitting parameters for obtaining a good agreement between measured and calculated contrast.

To estimate the tip dimension – and thus the rank of the tip matrix – that has to be taken into account for a correct simulation, we calculated the MFM response above characteristic points of the sample as a function of the dimension of the tip matrix. Figure 3.11(b) shows the results for two tip radii of curvature ( $r_{\text{tip}} = 100, 140$  nm) at two tip-sample distances

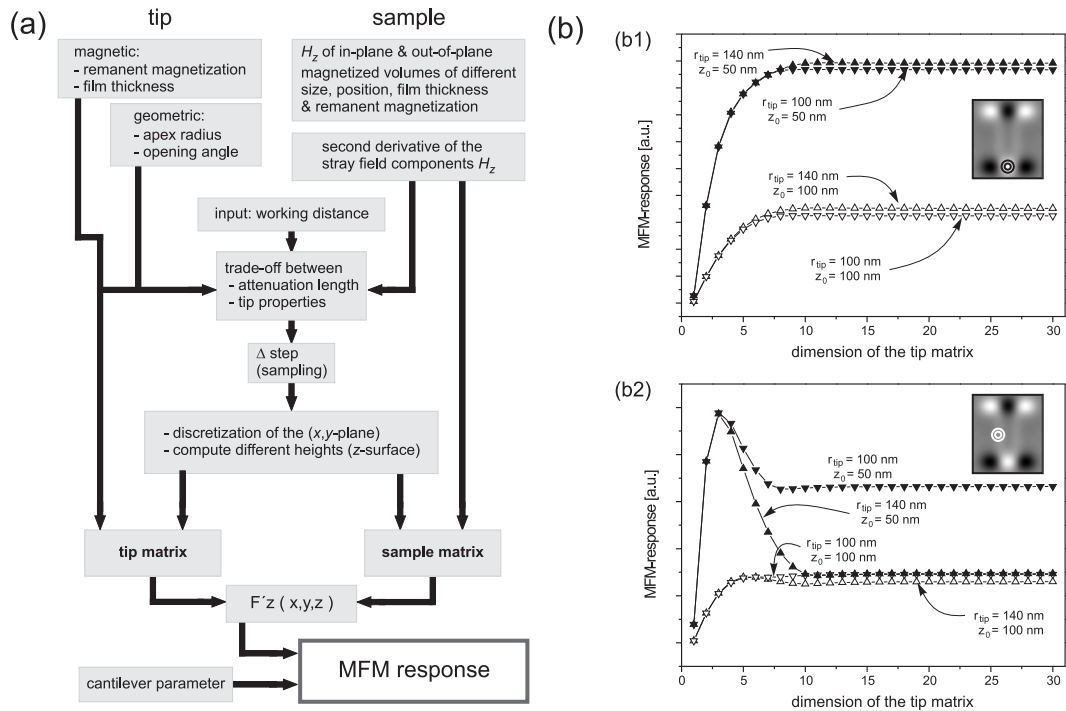


Figure 3.11: (a) Flow chart of the simulation procedure. (b) Plots of the MFM response above characteristic points of the sample as indicated in the figure (see insets): (b1) above the end of the in-plane bar magnet and (b2) above the Bloch wall. The calculations were performed at working distances of 50 and 100 nm, using tip radii of curvature of 100 and 140 nm, respectively. The cone opening angle of the tip is  $10^\circ$ .

( $z_0 = 50, 100$  nm). In (b1), the curves obtained above the end of an in-plane magnetized bar magnet are shown. The shape of the curves is similar with a stronger MFM response for smaller working distances. The tip geometry has no significant influence on the curves. It is found that in case of  $z_0 = 50$  nm, the tip matrix dimension  $n$  has to be larger than 10, whereas for  $z_0 = 100$  nm,  $n \geq 8$ .

A different behavior is observed for the out-of-plane magnetization within a Bloch wall, modeled by a bar magnet. For a large working distance ( $z_0 = 100$  nm), the tip geometry has only a minor influence on the MFM response and  $n \geq 10$  is sufficient for distinguishing the different tip shapes. When the tip is kept at small distances above the sample ( $z_0 = 50$  nm), a dramatic influence of the tip is observed due to the relative dimensions of tip and bar magnet. First, using a small tip matrix, the MFM response is overestimated. For  $n > 5$ , the tip geometry has a large impact on the response. Whereas for a tip radius of 100 nm  $n = 7$  is sufficient, a larger tip ( $r_{\text{tip}} = 140$  nm) requires  $n \geq 10$ . The tip geometry and working distance dependence of the MFM response can be easily understood bearing in mind the distribution of the second derivative of the stray field [113]. As a consequence of the close vicinity of areas with opposite sign of  $\partial^2 H_z / \partial z^2$ , the MFM response strongly depends function of the sampled area. For example, in case of a flat tip, large oppositely oriented areas ( $\partial^2 H_z / \partial z^2$ ) contribute to the overall signal.

Figure 3.12 shows the simulated results of the domain structure (cf. Fig. 3.9). The  $z$ -component of the magnetic stray field  $H$  is presented in (a) at a height of 100 nm.  $H_z$  shows a strong, smeared out contrast over the end of the in-plane domains. On the other hand, the stray field of the out-of-plane

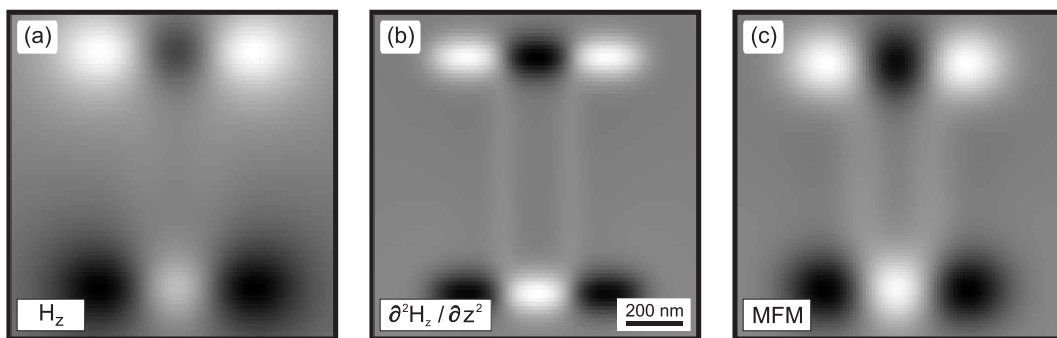


Figure 3.12:  $H_z$ -component of the stray field (a), the second derivative at a tip-sample distance  $z_0$  of 100 nm (b) and the corresponding MFM response (c) for the simulated domain structure shown in Fig. 3.9.

magnetization (Bloch wall) is hardly visible. For the second derivative of the magnetic stray field  $\partial^2 H_z / \partial z^2$ , shown in (b), a strong contrast enhancement of the out-of-plane magnetization is obvious. Moreover, the contrast of the in-plane domains is strongly localized at the ends of the domains. It is worth noting that the  $\partial^2 H_z / \partial z^2$ -image is identical with the MFM response for a strongly simplified tip represented by a single dipole. The artificial introduction of the effective position of the single tip dipole causes a less-localized and strongly underestimated MFM response, which is compensated by an overestimation of the dipole strength. The general MFM response (c) is given by the convolution of  $\partial^2 H_z / \partial z^2$  with the realistic tip model (tip radius of curvature 100 nm, magnetic coating thickness 40 nm, cone opening angle  $10^\circ$ , saturation magnetization 700 kA/m). Now, the finite size of the tip broadens the localized  $\partial^2 H_z / \partial z^2$ -signal. The MFM image [Fig. 3.12(c)] resembles the distribution of the stray field  $H_z$  [Fig. 3.12(a)] with the main difference that the Bloch walls show an enhanced contrast.

The presented simulation of the MFM response in real space can be used to at least qualitatively estimate the MFM signal of uniaxial domains of cuboidal shape. This way, in principle, arbitrary tip shapes and sample stray fields – provided that they can be approximated by an analytical expression – can be simulated quantitatively. The method presented here is used to correlate domain model and MFM response, which is presented in Chapter 5 in detail.

### 3.3.3 Extensions of the MFM setup

In the basic MFM setup, the measurements are performed at zero magnetic field and at room-temperature. In order to study the magnetic phase transition of MnAs films in the  $\alpha$ - $\beta$ -coexistence region, the MFM setup was equipped with a variable-temperature stage [86]. A Peltier element for cooling and a resistive heater were operated by a programmable temperature controller and a temperature sensor for the sample. The sample was mounted on top of a ceramic pad ( $14 \times 13 \text{ mm}^2$ ) with a heat-conducting paste. Under ambient conditions in air, the variable temperature stage was operated between 5 and  $50^\circ\text{C}$  with a nominal thermal stability of  $\pm 0.1 \text{ K}$ . Special care was taken to prevent ground loops which lead to unwanted electrical noise.

Additionally, we combined the variable-temperature setup with the possibility to apply an external magnetic field, which opens the door for studying magnetization reversal processes, as well as the field-dependent domain evolution and domain stability. The use of electromagnets offers a convenient way of exciting moderate magnetic fields in MFM. For achieving magnetic

fields above 10 mT, sample heating cannot be avoided easily [88]. Thus, for combining magnetic fields with a precise temperature control, the use of permanent magnets is advantageous. The core of the magnetic field unit is a rotatable permanent magnet. It is placed inside a yoke, as schematically shown in Fig. 3.13. Depending on the angle of rotation of the magnet, a variable amount of flux is guided towards the sample. The two extreme cases are illustrated in the inset of the Figure: on the bottom, the poles of the magnet are facing the yoke, resulting in the transfer of the maximum magnetic flux from the permanent magnet to the sample. Rotating the magnet reduces the flux penetrating into the yoke. After a full  $90^\circ$  rotation of the magnet, shown on the left-hand side, the magnetic flux coupled into the yoke is compensated and the magnetic field at the sample position is zero.

The design of the magnetic setup was determined by the space restrictions of the variable-temperature stage and the commercial scanning probe microscope setup. A detailed sketch of the magnetic field setup without the temperature stage is shown in Fig. 3.13. The permanent magnet is made of NdFeB (neodymium iron boron), a commercially available magnetic material with a very high remanence and energy density. It measures  $5 \times 5 \times 10 \text{ cm}^3$  with the magnetic poles being the side planes of the cuboid [55]. Together with soft iron caps, the cylindrical assembly can rotate freely inside the holder and the magnetic flux is transferred effectively to the yoke. The yoke is made of soft iron in order to obtain a low remanent field and a high saturation magnetization [6]. After machining the parts, they were annealed in a vacuum oven under hydrogen atmosphere to reduce the remanence. The field across the sample depends on the distance between the ends of the yoke. With a sample space of  $3 \times 1.2 \text{ cm}^2$ , a maximum field of 236 mT can be obtained. Higher field values are possible by narrowing the gap between the ends of the yoke at the cost of the free sample space.

The magnetic field at the sample position depends on the rotation angle in the assembly and was calibrated using a commercial Hall probe [88]. For larger field values, the rotational position of the magnet determines the field within an error of about 1%. The mechanical hysteresis, which is a result of the tolerance of the mechanical drive system, is significant for small field values. Thus, for obtaining the precise field values, a Hall probe is permanently fixed to the setup. It is used to measure the stray field of the yoke during MFM experiments, which is calibrated with respect to the field at the sample position. Systematic errors are therefore reduced, as the magnetic field applied to the sample can be directly monitored during MFM experiments and readjusted when necessary.

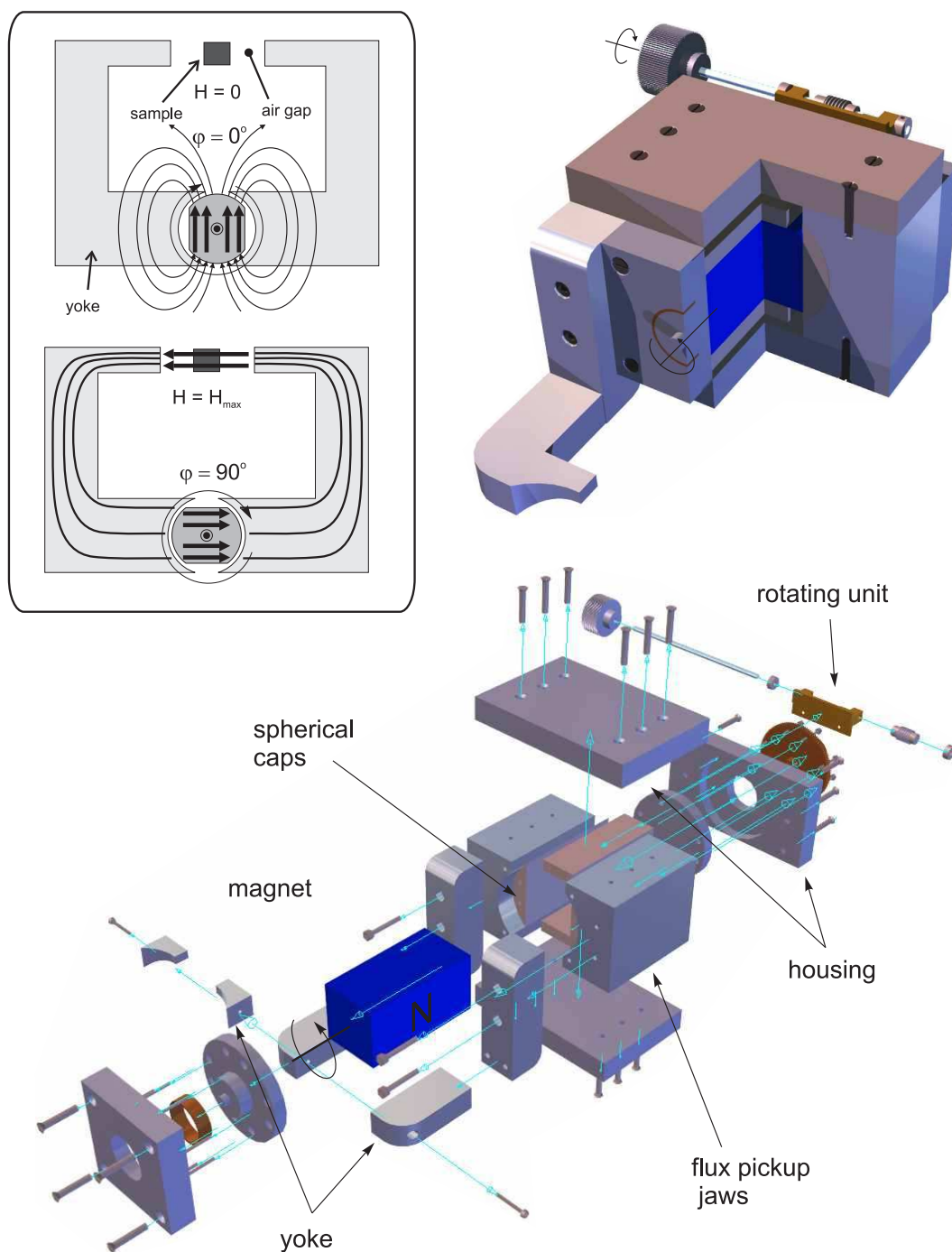


Figure 3.13: Sketch of the magnetic field assembly consisting of the permanent magnet, its rotating unit, as well as the yoke which serves as a flux guide. On the top right of the figure, a 3-dimensional cutaway sketch of the assembled rotating permanent magnet is shown. Inset: Schematic of the magnetic field setup: variable amounts of magnetic flux can be guided towards the sample by a rotation of the permanent magnet. On the top, the magnetic flux is shunted and the magnetic field at the sample position is zero. In the other extreme case the maximum flux is picked up.

# Chapter 4

## The micromagnetic simulator

Micromagnetics is the continuum theory of magnetic moments that describes the magnetic microstructure. It is an approach for deriving and explaining the magnetization distribution of a ferromagnet and its dynamics. It is considered as the theoretical basis of domain analysis. This apparatus is essential for a complete understanding of the formation of magnetic domains, as no experimental procedure allows for the direct observation of the interior of a ferromagnet. Therefore micromagnetic simulations can be considered as a supplement to the experimental observations.

Micromagnetics is based on the variational principle that allows for the determination of the magnetization distribution with the minimum total energy. The use of the variational calculus was first introduced by Landau and Lifshitz [68]. Brown [15] essentially extended the theory by taking the demagnetization effect into account, i.e. the energy of the stray field originating by the magnetization distribution. This leads to a set of differential equations, the so-called micromagnetic equations, which are nonlinear and nonlocal. This set of equations can only be solved analytically in some rare cases, mostly by the introduction of strong simplifications which leads to unrealistic approximations and therefore overidealized models.

Since the mid 1980s the ability to use large-scale computer power engendered a renaissance of micromagnetism, because it enabled to study more complex problems on large-scale magnetic samples in great detail. To date, there exist several numerical micromagnetics packages [14, 25, 35, 117] which are partly open-source projects. However, the demands for the simulation of MnAs films with thicknesses of more than 100 nm and with lateral dimensions of up to  $5 \times 5 \mu\text{m}^2$  are challenging, as for an adequate numerical treatment of the problem around  $20 \times 10^6$  interacting magnetic moments are required, and the introduction of parallel processing principles becomes necessary. To simulate three-dimensional magnetic structures of comparable size in general

and MnAs in particular, a numerical scheme has been developed.

In this chapter, the basics of micromagnetics are reviewed with a focus on the approximations of this classical theory. The details of the implementation of the developed numerical scheme is explained and a comparison with other simulation schemes is presented. The capabilities of the developed micromagnetic simulator are furthermore increased by the realization of a routine to calculate the MFM response using a realistic tip model introduced in Subsec. 3.3.2.

## 4.1 Basics of micromagnetism

Micromagnetics describes magnetic properties of a ferromagnet on an intermediate length scale, larger than the lattice constant but small enough to resolve the internal structure of domain walls [53]. The total energy of a micromagnetic system is given by

$$E_{\text{tot}} = E_{\text{ex}} + E_{\text{ani}} + E_{\text{d}} + E_{\text{ext}}. \quad (4.1)$$

It includes contributions such as the exchange energy  $E_{\text{ex}}$ , the magnetocrystalline anisotropy energy  $E_{\text{ani}}$ , as well as the magnetostatic energy  $E_{\text{d}}$  and the Zeeman energy  $E_{\text{ext}}$  due to an external field, which will be explained in detail below. The first two energy contributions are much stronger compared to the classical field energy but for a large ensemble of magnetic moments the latter, weak, long range energy contributions are becoming increasingly important. On an intermediate length scale, none of these energy contributions can be neglected and the detailed behavior depends on the balance of the individual terms to the total energy.

Although the origin of the collective phenomenon of magnetism is of pure quantum-mechanical nature, it is not possible to treat micromagnetic problems quantum-mechanically, for example by adding the anisotropy and magnetostatic energy terms as a perturbation to the exchange energy [37]. Currently the only realistic approach is to ignore the atomic nature of matter, to neglect quantum mechanical effects, and to use classical physics in a continuum description of a magnetic material. The transition from the quantum-mechanical theory to the classical continuum theory of micromagnetism is performed by replacing the spin by a classical vector of magnetic moment and by approximating their lateral distribution by a continuous vector field [27]. The validity of such a theory rests in the fact that all energy contributions are small compared to the exchange energy. They can only slightly misalign parallel magnetic moments at neighboring lattice points. Therefore it seems

legitimate to approximate the distribution of magnetic moments with a continuous function. As a consequence, sums over lattice points are replaced by integrals over a volume and the technique of variational calculus becomes applicable [15].

### 4.1.1 Energy contributions in micromagnetism

The inner energy of a ferromagnet is uniquely determined by the magnetization field  $\mathbf{M}(\mathbf{r})$  for a given set of temperature-dependent material parameters. The total Gibbs free energy<sup>1</sup> is given by the integration of the contributing energy densities over the magnetized volume

$$E_{\text{tot}} = \int_V (\epsilon_{\text{ex}} + \epsilon_{\text{ani}} + \epsilon_{\text{d}} + \epsilon_{\text{ext}}) dV . \quad (4.2)$$

The magnetization  $\mathbf{m}$  is considered to be the only independent variable in Eq. 4.2, with  $\mathbf{m}(\mathbf{r}) = \mathbf{M}(\mathbf{r})/M_s$  under the constraint  $|\mathbf{m}| = 1$ . Here,  $M_s$  is the saturation magnetization of the material. Only the direction of magnetization is assumed to be a spatial function, while the saturation magnetization is constant throughout the sample. The energy terms are formulated as follows:

**Exchange energy density:** The exchange energy density is the term that represents the quantum mechanical coupling originating the collective character of magnetism. The exchange interaction in the classical approximation is given by the Heisenberg Hamiltonian

$$\epsilon_{\text{ex}} = -2 \sum_{i < j} J_{ij} \mathbf{S}_i \cdot \mathbf{S}_j = -2 \sum_{i < j} J_{ij} \cos(\phi_{ij}) , \quad (4.3)$$

where  $J_{ij}$  is referred to as the exchange integral of interacting spins  $S_i$  and  $S_j$  located at the lattice sites  $\mathbf{r}_i$  and  $\mathbf{r}_j$ , where  $\phi$  is the angle between interacting spins, which is assumed to be small. The transition to micromagnetics is performed replacing the spin operators by the continuous function of averaged magnetic moments  $\mathbf{m}(\mathbf{r})$  at their respective positions. For small angles  $\cos(\phi_{ij}) \approx 1 - 1/2\phi_{ij}^2$ , Taylor expansion of  $\mathbf{m}(\mathbf{r})$  up to second order under the constraint  $|\mathbf{m}| = 1$  reveals for the exchange energy density [27, 53]

$$\epsilon_{\text{ex}} = \sum_{i,j,k} A_{ij} \frac{\partial m^k(\mathbf{r})}{\partial x_i} \frac{\partial m^k(\mathbf{r})}{\partial x_j} , \quad (4.4)$$

---

<sup>1</sup>In the theory of micromagnetism, neither temperature fluctuations nor temperature-induced disorder are taken into consideration. Thus, the Gibbs free energy and the inner energy  $U$ , are identical ( $E_{\text{tot}} = U - TS$  with  $T$  temperature and  $S$  entropy).



where  $A_{ij}$  is the exchange stiffness tensor. The exchange energy term is typically assumed to be isotropic in micromagnetism. In this case,  $A_{ij} = A \cdot \delta_{ij}$ , which reduces Eq. 4.4 to the exchange stiffness expression  $\epsilon_{\text{ex}} = A [\nabla \cdot \mathbf{m}(\mathbf{r})]^2$ , usually used in micromagnetics. It is a convenient approximation for cubic crystals where the exchange is governed by the nearest-neighbor interaction [50].

For all non-cubic crystals, anisotropic exchange can be present and the implementation of the exchange stiffness tensor is needed. Here, the exchange anisotropy is solely related to the different bonding in the crystal. This must not be confused with the rather weak relativistic anisotropies, which involve spin-orbit coupling and depend on the angle between magnetization and the crystal axes. The exchange energy density in Eq. 4.4 is isotropic with respect to the magnetization, but anisotropic with respect to the Nabla operator  $\nabla = \partial/\partial x_i$ , reflecting a bonding-related anisotropy [130].

The exchange interaction tensor is defined to be positive to ensure an increase of the energy with a change in the magnetization. It is assumed to be symmetric, because an antisymmetric part is canceled out in Eq. 4.4 due to the permutation of the derivatives.

The experimental determination of the exchange constant is rather inaccessible and the quantity is most often derived indirectly from the Curie point or the temperature dependence of the magnetization. An attempt has been made to directly measure the spinwave stiffness constant and thus the exchange constant of MnAs thin films [147]. The estimated value of  $A = 1.7 \cdot 10^{-14}$  J/m is orders of magnitude smaller than typical values, ranging from  $10^{-11} \dots 10^{-12}$  J/m. Recently, it has become possible to determine the exchange stiffness for materials from first principles [13, 115]. Unfortunately, no calculation of the exchange stiffness tensor or the stiffness constant have been performed for MnAs so far. Therefore, the stiffness constant is estimated using the Curie-temperature  $T_C = 130^\circ\text{C}$ , the Boltzmann constant  $k_B$  and the lattice constant between nearest neighbor Mn lattice sites  $c/2$ :  $A(T = 0) \cdot c/2 \approx k_B \cdot T_C$  to  $A \approx 1.9 \cdot 10^{-11}$  J/m. For higher temperatures the exchange stiffness decreases. For the micromagnetic calculations of MnAs an exchange stiffness constant of  $A = 1 \cdot 10^{-11}$  J/m was used throughout.

**Magnetocrystalline anisotropy energy density:** The energy of a ferromagnet depends on the direction of magnetization relative to the structural axes of the material. This effect is called magnetocrystalline anisotropy and is attributed to the spin-orbit interactions, which couples the spin moment to the lattice. An expansion of the power series of magnetization components relative to the crystal axes is used to describe the most important

contributions.

Rarely more than the first two significant terms have to be considered, since thermal agitation of the spins tends to average out the higher-order contributions [53].

The magnetocrystalline anisotropy of the ferromagnetic  $\alpha$ -phase of hexagonal MnAs is thus a function of only one parameter, the angle  $\theta$  between the  $c$ -axis and the direction of magnetization

$$\epsilon_{\text{ani}} = K_0 + K_{u_1} [\mathbf{u} \times \mathbf{m}(\mathbf{r})]^2 + K_{u_2} [\mathbf{u} \times \mathbf{m}(\mathbf{r})]^4 + \dots \quad (4.5)$$

The subscript  $u$  is used here to refer to the uniaxial symmetry and  $\mathbf{u}$  is the unit vector of the anisotropy axis. The coefficients are temperature-dependent constants and their values can be taken from experiments. For bulk MnAs they are given in Tab. 2.1. For MnAs films grown on GaAs they have been extracted from SQUID [118] and from ferromagnetic resonance measurements [69], confirming a magnetically hard axis behavior along the  $c$ -axis. Crystals with an easy axis along  $\mathbf{u}$  are described by  $K_{u_1} > 0$ , and with an easy plane perpendicular to  $\mathbf{u}$  are described by  $K_{u_1} < 0$ . Therefore, MnAs exhibits a 'planar' magnetic anisotropy, that reflects itself in a negative  $K_{u_1}$ . Figure 4.1 shows a graphic representation of the anisotropy energy

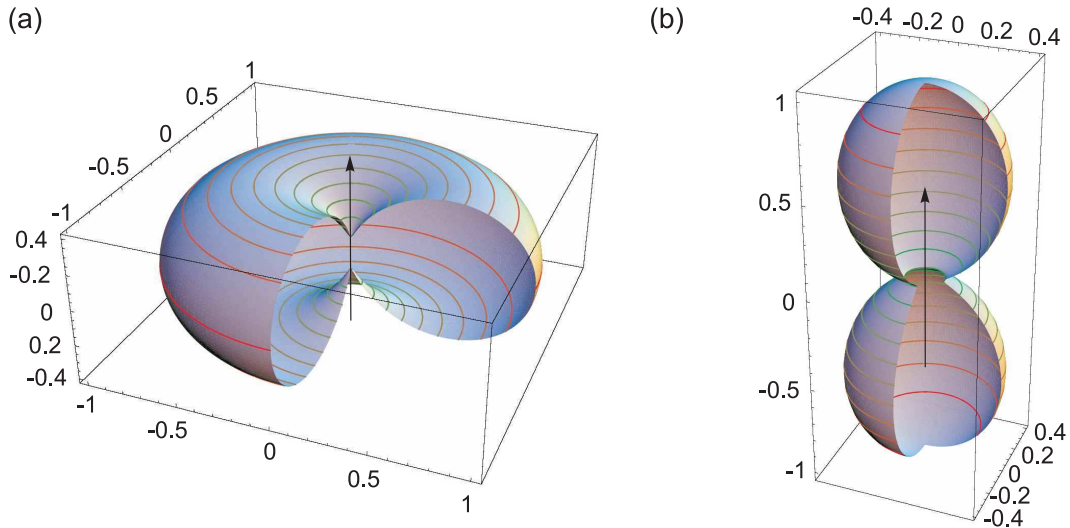


Figure 4.1: Anisotropy energy surfaces plotted (a) an axial  $K_{u_1} > 0$  and (b) a planar  $K_{u_1} < 0$  symmetry. The contours of equal energy are added with different colors for directions of the magnetization associated with high energy (red) and low energy (green).

contribution for an uniaxial and a planar magnetocrystalline anisotropy. It visualizes the local energetic environment of a magnetic moment in a ferromagnet. The constant  $K_0$  has no influence of the energy dependence on the magnetization direction. In the simulation it is used to balance the energy contribution to reduce numerical errors and to improve the convergence.

**Magnetic field energy:** The magnetic field energy consists of two parts, namely Zeeman energy due to an external field  $E_{\text{ext}}$  and the demagnetization energy associated with the stray field. The total energy of the system can be influenced by externally applied magnetic fields. The external field  $\mathbf{B}_{\text{ext}}$  is independent of the magnetization distribution and assumed to be spatially constant. The associated Zeeman energy is:

$$E_{\text{ext}} = - \int_{(\text{sample})} \mathbf{M}(\mathbf{r}) \cdot \mathbf{B}_{\text{ext}} dV . \quad (4.6)$$

The second part of the magnetic field energy is the most cumbersome contribution to the total energy. The stray field originates from the magnetization vector field itself. The energy connected to the stray field is

$$E_{\text{d}} = \frac{\mu_0}{2} \int_{(\text{all space})} \mathbf{H}_{\text{d}}^2(\mathbf{r}) dV = -\frac{\mu_0}{2} \int_{(\text{sample})} \mathbf{M}(\mathbf{r}) \cdot \mathbf{H}_{\text{d}}(\mathbf{r}) dV . \quad (4.7)$$

Here,  $\mu_0 = 4\pi \cdot 10^{-7} \text{ V}\cdot\text{s}/\text{A}\cdot\text{m}$  is the vacuum permeability. The first integral, extending over all space, shows that the demagnetization energy is always positive. For the calculation of the demagnetization energy it is more practical to evaluate the second integral. The stray field originating from a magnetization vector field is generally given by a scalar potential in the absence of current densities [58]. In the magnetostatic case ( $\nabla \cdot \mathbf{B} = \mu_0 \nabla \cdot (\mathbf{H}_{\text{d}} + \mathbf{M}) = 0$ ,  $\nabla \times \mathbf{H} = 0$ ) it can be described introducing the scalar magnetic potential  $\Phi_{\text{M}}$

$$\mathbf{H}_{\text{d}}(\mathbf{r}) = -\nabla_{\mathbf{r}} \cdot \Phi_{\text{M}}(\mathbf{r}) , \quad (4.8)$$

resulting in the Poisson equation for the scalar magnetic potential  $\Delta\Phi_{\text{M}} = \nabla \cdot \mathbf{M}$ . If there are no boundary surfaces, the solution is

$$\Phi_{\text{M}}(\mathbf{r}) = -\frac{1}{4\pi} \int \frac{\nabla_{\mathbf{r}'} \cdot \mathbf{M}(\mathbf{r}')}{|\mathbf{r} - \mathbf{r}'|} dV' . \quad (4.9)$$

If  $\mathbf{M}$  is well-behaved and localized, an integration by parts can be performed yielding

$$\Phi_{\mathbf{M}}(\mathbf{r}) = \frac{1}{4\pi} \int \mathbf{M}(\mathbf{r}') \cdot \nabla_{\mathbf{r}'} \left( \frac{1}{|\mathbf{r} - \mathbf{r}'|} \right) dV'. \quad (4.10)$$

The solution 4.10 is generally applicable, even for the limit of discontinuous distribution of  $\mathbf{M}$ , because a limiting procedure can still be introduced in order to discuss discontinuities in  $\mathbf{M}$  [58].

The internal magnetic field  $\mathbf{H}$  of a uniformly magnetized body  $\mathbf{M}$  can be conveniently expressed in terms of a demagnetizing tensor  $\underline{\underline{\mathbf{N}}}$  to  $\mathbf{H} = \underline{\underline{\mathbf{N}}} \cdot \mathbf{M}$  with the demagnetization energy  $E_d = -\mu_0/2 \mathbf{M} \cdot \underline{\underline{\mathbf{N}}} \cdot \mathbf{M}$ . However, this holds exactly only for an ellipsoidal body [15].

The tensor formulation can be used to develop an expression for the macroscopic magnetic field in non-uniformly magnetized bodies of arbitrary shape [95]. For a uniformly magnetized body with the magnetization  $\mathbf{M}'$ , the scalar magnetic potential (Eq. 4.10) is given by

$$\Phi_{\mathbf{M}}(\mathbf{r}) = \frac{\mathbf{M}'}{4\pi} \int \nabla_{\mathbf{r}'} \left( \frac{1}{|\mathbf{r} - \mathbf{r}'|} \right) dV', \quad (4.11)$$

where the integration is over the magnetized region  $V'$ . If  $V$  is a different volume, which may overlap with  $V'$ , the average magnetic field in  $V$  is

$$\langle \mathbf{H}_d \rangle_V = \frac{1}{V} \int_V -\nabla_{\mathbf{r}} \cdot \Phi_{\mathbf{M}}(\mathbf{r}) dV = -\mathbf{M}' \cdot \underline{\underline{\mathbf{N}}}, \quad (4.12)$$

where

$$\underline{\underline{\mathbf{N}}} = \frac{1}{4\pi V} \int_V \int_{V'} \nabla_{\mathbf{r}} \nabla_{\mathbf{r}'} \left( \frac{1}{|\mathbf{r} - \mathbf{r}'|} \right) dV' dV. \quad (4.13)$$

The energy in the volume  $V$  due to the field  $\mathbf{H}_d$  is now

$$E_d = -\frac{\mu_0}{2} \mathbf{M} \cdot \underline{\underline{\mathbf{N}}} \cdot \mathbf{M}' V. \quad (4.14)$$

In chapter 4.2.1 it will be shown, how the demagnetization tensor formalism can be efficiently used in a generalized form to describe the demagnetization energy of a stepwise constant magnetization distribution.

## 4.1.2 Equation of motion

To calculate the equilibrium magnetization configuration, the total free energy has to be minimized with respect to the magnetization  $\mathbf{m}(\mathbf{r})$ . The equilibrium state of the system can be obtained using the variational calculus introduced by Brown [15]:

$$\frac{\delta E_{\text{tot}}}{\delta \mathbf{m}(\mathbf{r})} = 0. \quad (4.15)$$

leading to the micromagnetic equations

$$\mathbf{m}(\mathbf{r}) \times \left( \mathbf{H}_{\text{ext}} + \frac{\mathbf{H}_d(\mathbf{r})}{2} - \frac{2}{\mu_0 M_s} \sum_{i,j} A_{ij} \cdot \frac{\partial^2 \mathbf{m}(\mathbf{r})}{\partial x_i \partial x_j} + \frac{\delta \epsilon_{\text{ani}}}{\delta \mathbf{m}(\mathbf{r})} \right) = 0. \quad (4.16)$$

This is not the general form of the micromagnetic equations, as magnetostrictive terms and external stress are not included in the total energy. The second term of the vector product in Eq. 4.16 can be considered as an effective magnetic field  $\mathbf{H}_{\text{eff}}(\mathbf{r})$ , which offers a simple interpretation of the micromagnetic equations. The effective field provides a torque acting on the magnetization. In equilibrium  $\mathbf{M}(\mathbf{r}) \times \mathbf{H}_{\text{eff}}(\mathbf{r}) = 0$ , the magnetization is aligned in the effective field and the torque, which acts on the magnetization, vanishes. The effective magnetic field can be derived from the total energy

$$\mathbf{H}_{\text{eff}}(\mathbf{r}) = -\frac{1}{\mu_0} \frac{\delta \epsilon_{\text{tot}}(\mathbf{r})}{\delta \mathbf{M}(\mathbf{r})}. \quad (4.17)$$

The variational procedure also yields boundary conditions. Surface and interface effects enter at this point. For MnAs films surface and interface effects of the exchange and the magnetocrystalline anisotropy have not been reported so far. Therefore the von Neumann-type boundary condition  $\partial \mathbf{m} / \partial \mathbf{n} = 0$  is chosen.

A number of numerical minimization schemes are applicable to solve the stationary state of a micromagnetic problem [125]. However, the energy landscape of realistic magnetization distributions is rather complex, revealing many local maxima, minima and saddle points. Therefore, the choice of the initial magnetization distribution strongly influences the result [124]. A more realistic approach to find the equilibrium magnetization is provided by taking advantage of the magnetization dynamics. Literally spoken, the path through the energy landscape is calculated, starting from the initial magnetization and moving towards the energy minimum.

The equation of motion for a magnetization was derived by Landau and Lifshitz [68] and describes the time evolution of the magnetization in a magnetic field

$$\begin{aligned} \frac{d\mathbf{M}(\mathbf{r}, t)}{dt} = & - \frac{\gamma}{1 + \alpha^2} \mathbf{M}(\mathbf{r}, t) \times \mathbf{H}_{\text{eff}}(\mathbf{r}, t) \\ & - \frac{\alpha \gamma}{(1 + \alpha^2) \cdot M_s} \mathbf{M}(\mathbf{r}, t) \times [\mathbf{M}(\mathbf{r}, t) \times \mathbf{H}_{\text{eff}}(\mathbf{r}, t)]. \end{aligned} \quad (4.18)$$

where  $\gamma = 2.21 \cdot 10^5$  m/A·s is the gyromagnetic ratio of the free electron spin and  $\alpha$  is a phenomenological damping constant.

As illustrated in Fig. 4.2 (a) the first term in Eq. 4.18 describes the precession of the magnetization around the effective field and the second term the energy dissipation. The latter finally causes the alignment of the magnetization along the magnetic field as the system proceeds towards equilibrium. The energy minimum is reached when the magnetic moments are aligned with the effective field. The intrinsic time scale is determined by the Larmor frequency; the precession time is smaller than nanoseconds. A deeper understanding of the damping process is needed to precisely simulate the magnetization dynamics. In the phenomenological description of micromagnetics, the possible damping processes are taken care of in the parameter  $\alpha$ , which is usually set to a value between 0.1 and 1. The influence of the damping parameter on the magnetization dynamics is shown in Fig. 4.2(b). Although a large damping constant inhibits the motion of the magnetization and thus affects the possibility to access different energy states, its choice is not critical, if the Landau-Lifshitz-Gilbert equation (LLG) is only used to evolve the system towards equilibrium, i.e. calculating a static micromagnetic problem.

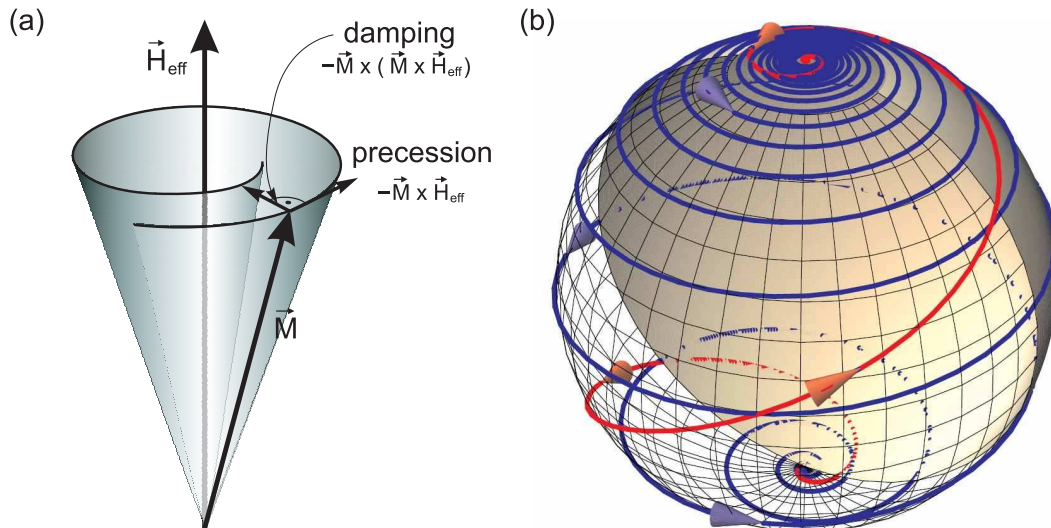


Figure 4.2: (a) Sketch of the gyromagnetic precession motion. (b) Calculated trajectories of a normalized magnetic moment on the unit sphere for two different damping parameters ( $\alpha = 0.5$  red curve,  $\alpha = 0.1$  blue curve) according to Eq. 4.18 after reversal of the effective field.

The Landau-Lifshitz-Gilbert equation is the most widely used approach in micromagnetic simulations to find the equilibrium magnetization distribution. Besides, it is the starting point of any dynamic description of micromagnetic processes.

## 4.2 Description of the implementation

### 4.2.1 Discretization of the magnetization distribution and the effective magnetic field

To calculate the effective magnetic field and to solve Eq. 4.18, the magnetization vector field is discretized in space and time. The spatial discretization was achieved by introducing a grid with cuboidal cells with the dimensions  $(\Delta x, \Delta y, \Delta z)$  and a volume of the subelements of  $\Delta V = \Delta x \cdot \Delta y \cdot \Delta z$ . The magnetization is approximated by one vector for each cell, which represents an average magnetic moment of the cuboid.

The required discretization level has to be chosen to ensure that the numerical conversion of the continuous to a stepwise constant magnetization distribution is sufficiently accurate to give meaningful results. The typical length scales are the magnetocrystalline and the magnetostatic exchange lengths,  $l_{\text{ex}} = \sqrt{A/K}$  and  $l_{\text{stat}} = \sqrt{2A/\mu_0 \cdot M_s^2}$ , respectively [53]. The cell dimensions have to be smaller than the smallest of both to ensure a convergence of the LLG [112]. For MnAs with a magnetocrystalline anisotropy constant  $K = 7.2 \cdot 10^5 \text{ J/m}^3$ , an exchange stiffness constant of  $A = 10^{-11} \text{ J/m}$  and saturation magnetization of  $M_s = 8 \cdot 10^5 \text{ A/m}$  result in  $l_{\text{ex}} = 3.7 \text{ nm}$  and  $l_{\text{stat}} = 5 \text{ nm}$ .

The discretization of the effective magnetic field is straightforward for the finite-mesh system. The partial derivatives of  $\mathbf{m}(\mathbf{r})$  were approximated by finite difference quotients, and the integration over the volume by a summation over cuboidal subelements for each energy term. The energy and the contributions to the effective magnetic field of applied field and the local interactions, like magnetocrystalline anisotropy energy and exchange energy, are needed. For a cell with index  $i$  the fraction of the effective magnetic field due to the uniaxial magnetocrystalline anisotropy is

$$\mathbf{H}_{\text{ani}}^i = -\frac{1}{\mu_0} \cdot \frac{\delta \epsilon_{\text{ani}}}{\delta \mathbf{M}(\mathbf{r})} = \frac{2K_{u_1} + 4K_{u_2}}{\mu_0 M_s} (\mathbf{m}^i \cdot \mathbf{u}) \mathbf{u} - \frac{4K_{u_2}}{\mu_0 M_s} (\mathbf{m}^i \cdot \mathbf{u})^3 \mathbf{u}. \quad (4.19)$$

The contribution of the exchange interaction to the effective magnetic field in a three-point difference scheme in cell  $i$  is

$$\begin{aligned}
\mathbf{H}_{\text{ex}}^i &= -\frac{1}{\mu_0} \cdot \frac{\delta \epsilon_{\text{ex}}}{\delta \mathbf{M}(\mathbf{r})} \\
&= -\frac{2}{\mu_0 M_s} \sum_{k,l} A_{kl} \frac{\mathbf{m}_{k+1,l+1}^i - \mathbf{m}_{k-1,l+1}^i - \mathbf{m}_{k+1,l-1}^i + \mathbf{m}_{k-1,l-1}^i}{4 \Delta_k \Delta_l},
\end{aligned} \tag{4.20}$$

where  $\Delta_k$  and  $\Delta_l$  are distances between neighboring cells along the respective directions. Other discretization schemes for the exchange energy have been investigated [26, 156] and it was found out, that a five-point discretization produces effectively stiffer exchange interaction between the spins. The influence is small, however, a five-point approximation is less likely to produce magnetization states in which neighboring magnetic moments have large angles between them. For an appropriate consideration of the boundary condition  $\partial \mathbf{M} / \partial \mathbf{n} = 0$  in the numerical scheme, this is only necessary for the calculation of the discretized exchange energy of boundary cells. Obeying the von Neumann boundary condition the grid is extended outside the boundary by mirroring the cells.

The calculation of the demagnetization field in the discretization scheme is the most complicated part, as Eq. 4.7 has to be evaluated. Fortunately, in the approximation of a magnetization distribution  $\mathbf{M}(\mathbf{r})$  with a stepwise constant magnetization, the calculation of the demagnetization energy can be performed using a generalized demagnetization tensor [95]. Applying Eq. 4.14 to an ensemble of subcubes, which approximate a ferromagnet in the manner as described above, the demagnetization field of the cell with index  $i$  at the position  $\mathbf{r}_i$  is given by the sum over all subcells  $j$

$$\mathbf{H}_{\text{d}}^i = - \sum_j \underline{\underline{\mathbf{N}}}(\mathbf{r}_i - \mathbf{r}_j) \cdot \mathbf{M}^j, \tag{4.21}$$

and the demagnetization energy

$$E_{\text{d}} = -\frac{\mu_0}{2} \cdot \Delta V \sum_n \mathbf{M}^n \cdot \mathbf{H}_{\text{d}}^n = -\frac{\mu_0}{2} \cdot \Delta V \sum_{i,j} \mathbf{M}^i \cdot \underline{\underline{\mathbf{N}}}(\mathbf{r}_i - \mathbf{r}_j) \cdot \mathbf{M}^j, \tag{4.22}$$

where the demagnetization tensor is reduced to surface integrals, according to Eq. 4.13 and changes to

$$\underline{\underline{\mathbf{N}}}(\mathbf{r}_i - \mathbf{r}_j) = \frac{1}{4\pi\Delta V} \oint_{S_i} \oint_{S_j} \frac{d\mathbf{S}_i d\mathbf{S}_j}{|\mathbf{r}_i - \mathbf{r}_j|}. \tag{4.23}$$

The principle of applying the generalized demagnetization tensor is explained for two interacting subelements of cuboidal shape separated by a



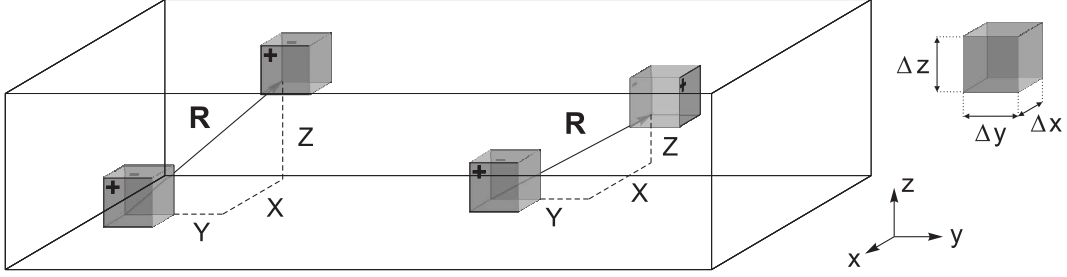


Figure 4.3: Calculation of the generalized demagnetization tensor components for the magnetostatic interaction between two subcubes at distance  $\mathbf{R}$ . The charged surfaces involved in the calculation are indicated, on the left for the component  $N_{xx}$  and on the right for  $N_{xy}$ .

relative distance  $\mathbf{R} = (X, Y, Z)$ . The distance vector is defined between the local reference points of the cubes and the local coordinates of each cube are connected to the reference points, as shown in Fig. 4.3. Each component of the demagnetization tensor involves interactions between two pairs of rectangular surfaces, because the normals of the faces are perpendicular to each other. For the  $N_{xx}$  component four interactions between the parallel faces have to be considered

$$N_{xx} = \frac{1}{4\pi\Delta V} [2F(X, Y, Z) - F(X + \Delta x, Y, Z) - F(X - \Delta x, Y, Z)] , \quad (4.24)$$

with

$$F(X, Y, Z) = \int_0^{\Delta z} \int_0^{\Delta y} \int_0^{\Delta z} \int_0^{\Delta y} \frac{dz dy dz' dy'}{\sqrt{X^2 + (y + Y - y')^2 + (z + Z - z')^2}} . \quad (4.25)$$

The negative sign comes from the interaction of faces with opposite signs. The formulas for the component  $N_{xy}$  can be deduced in a similar way:

$$N_{xy} = \frac{1}{4\pi\Delta V} [G(X, Y, Z) - G(X - \Delta x, Y, Z) - G(X, Y + \Delta y, Z) + G(X - \Delta x, Y + \Delta y, Z)] , \quad (4.26)$$

with

$$G(X, Y, Z) = \int_{Y-\Delta y}^Y \int_{Z-\Delta z}^Z \int_z^{z+\Delta z} \int_X^{X+\Delta x} \frac{dy dz dz' dx'}{\sqrt{x'^2 + y^2 + z'^2}} . \quad (4.27)$$

The integrals in Eqs. 4.25 and 4.27 can be calculated straightforwardly resulting in analytic functions, which are summarized in Ref. [95]. The demagnetization tensor is symmetric and the diagonal elements correspond to interactions, where the faces of the two interacting cubic elements are parallel, while the off-diagonal elements represent the interaction between perpendicular faces. Thus all tensor components have the same form, either  $N_{xx}$  or  $N_{xy}$ , and can be obtained by permutating the variables  $X, Y, Z$  and the cell dimensions  $\Delta x, \Delta y, \Delta z$ , revealing

$$\underline{\underline{\mathbf{N}}}(\mathbf{r}_i - \mathbf{r}_j) = \underline{\underline{\mathbf{N}}}\begin{pmatrix} X \\ Y \\ Z \end{pmatrix} = \begin{pmatrix} N_{xx}(X, Y, Z, \Delta x, \Delta y, \Delta z) & N_{xy}(X, Y, Z, \Delta y, \Delta x, \Delta z) & N_{xy}(X, Z, Y, \Delta x, \Delta z, \Delta y) \\ & N_{xx}(Y, X, Z, \Delta y, \Delta x, \Delta z) & N_{xy}(Z, Y, X, \Delta z, \Delta y, \Delta x) \\ & & N_{xx}(Z, Y, X, \Delta z, \Delta y, \Delta x) \end{pmatrix}. \quad (4.28)$$

The evaluation of the long-range magnetostatic field is the most time-consuming part. For the calculation of the demagnetization energy, the double sum of Eq. 4.22 has to be calculated. A direct calculation of the demagnetization energy requires  $O(N^2)$  operations, where  $N$  is the total number of interacting subelements. For large data fields, the computation can be substantially accelerated by using the convolution theorem and the fast Fourier transformation (FFT), thereby reducing the number of operations to  $O(N \log_2 N)$  [159]. The magnetization distribution and the demagnetization tensor are Fourier-transformed and their product yields the demagnetization field in frequency space, which has to be inversely transformed. For a three-dimensional grid, six fast Fourier transformations are needed for one evaluation of the demagnetization field.

To generalize the fast Fourier transformation technique to any boundary condition, the finite size effect of the system is considered, applying the standard zero padding techniques. The number of cells in each dimension must be a power of two and no less than twice the original dimensions [105]. The utilization of the demagnetization tensors separates the geometry of the particle and the magnetization distribution. The geometrical factors of the demagnetization tensor remain constant and only need to be calculated once.

Taking advantage of the convolution theorem, the Fourier transformation is stored in an array and can be repeatedly used, which greatly reduces the computational effort.

### 4.2.2 Time discretization

To solve a static micromagnetic problem, the LLG (Eq. 4.18) is used. The evolution to equilibrium is performed by time integration for each cell. A system of ordinary differential equations (ODE) with initial values has to be solved

$$\frac{dm}{dt} = f(t, m), \quad m \in \mathbb{R}^{3N}, \quad m(t_0) = m_0. \quad (4.29)$$

Explicit numerical schemes, such as Euler or fourth-order Runge-Kutta methods [152], and different types of Adam formulas are commonly used methods for the simulation of the Landau-Lifshitz-Gilbert equation [74, 83, 137]. Although explicit schemes achieve a high order of accuracy in space and time, the time step size is limited by the stability of the numerical scheme. For micromagnetic problems with a small damping factor  $\alpha$ , time steps smaller than picoseconds are required [36] and implicit schemes become more efficient. The stiffness of the Landau-Lifshitz-Gilbert equation has been investigated by solving the system of ordinary differential equations for different micromagnetic problems with an implicit and an explicit scheme [150]. For non-stiff problems, explicit schemes and for stiff problems, implicit schemes are recommended. For the latter technique, a nonlinear algebraic system must be solved, which results in a more time-consuming procedure, however, the appropriate time step can be much larger compared to explicit methods. The stiffness of the problem can be interpreted as the ratio of computation time needed for the evolution of the magnetization distribution. It has been shown that a micromagnetic problem becomes more stiff, if the spatial discretization is small or the exchange term becomes dominant. For systems with a high magnetocrystalline anisotropy, the degree of stiffness for the ODE system decreases. The choice of an appropriate numerical method depends on the stiffness of the differential equation and therefore the algorithm to solve the Landau-Lifshitz-Gilbert equation has to be well-suited for the characteristics of the system [150].

So far, the Euler scheme is implemented. It is an explicit scheme, only the right hand side of the Landau-Lifshitz Gilbert equation has to be evaluated. The new magnetization vector of a cell with index  $i$  is

$$\mathbf{m}_{t+\Delta t}^i = \mathbf{m}_t^i + \Delta t \left[ -\frac{\gamma}{1 + \alpha^2} \mathbf{m}_t^i \times \mathbf{h}_t^i - \frac{\alpha \gamma}{(1 + \alpha^2)} \mathbf{m}_t^i \times (\mathbf{m}_t^i \times \mathbf{h}_t^i) \right]. \quad (4.30)$$

To reduce the accumulation of errors, an integration step is followed by a renormalization procedure, i.e. all magnetization vectors are normalized to fulfill the constraint  $|\mathbf{m}| = 1$ . This guarantees that the norm does not drift away during time evolution and the stability of explicit schemes is significantly improved. The choice of implementing explicit schemes can be justified for MnAs, as it exhibits a high magnetocrystalline anisotropy constant. However, for testing and benchmarking the micromagnetic simulator by applying it to the standard micromagnetic problem, a high computational effort results from the stiffness.

### 4.3 Parallelization scheme and general algorithm

For a realistic simulation of the domain features of large structures, calculations on a parallel computer were performed. The most time-consuming step during a calculation is the fast Fourier transformation, which is calculated using the 'Fastest Fourier Transform in the West' package FFTW [39]. For the parallelization, the message passing interface standard MPI is used [93], as an MPI compatible version is available for FFTW.

In the parallelization scheme, two processors set up a unit that automatically accounts for the implemented generalized boundary conditions of the FFT. Additionally, a simple grid partitioning scheme was applied, where the largest dimension of the real grid is divided into parts, which equals twice the number of available processors.

As illustrated in Fig. 4.4, for the case of four processors the grid was divided into two parts at the midpoint of the largest grid dimension. This scheme can be easily extended to an arbitrary even number of processors. For the Fourier transformation of the magnetization distribution and the inverse Fourier transformation of the demagnetization field, the FFTW routine takes advantage of all processors. For the local energy contributions the processors calculate the contributions of each subcube of its subgrid independently. The magnetization components of the edge cells of the subgrid were transferred to the processor evaluating the neighboring subgrid to calculate the exchange stiffness energy and the effective field contribution of the edge cells to the neighboring subgrid. The introduction of these ghost cells avoids

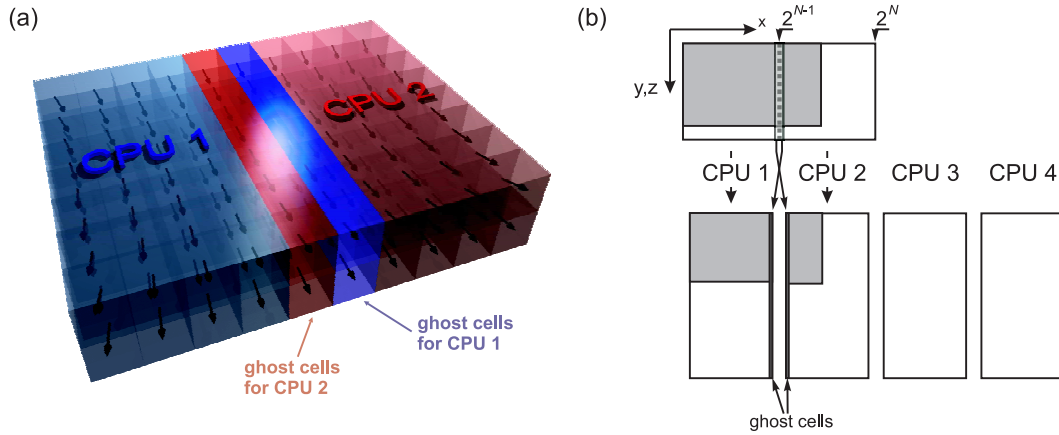


Figure 4.4: (a) Parallelization scheme for four processors (CPUs). (b) Memory allocation scheme for four processors. The memory space occupied for the magnetization vector field (dark) is first extended in all dimensions to the next power of two  $N$  by filling with zeros (white). The grid is then divided and sent to CPU 1 and CPU 2. CPU 3 and CPU 4 support CPU 1 and CPU 2 with FFT calculations. Their memories are initially padded with zeros.

latency and reduces bandwidth constraints between the processors, as only the information of the magnetization vector at the boundary has to be sent.

A flowchart of the general algorithm is shown in Fig. 4.5. In the initialization routine, first the problem definition, i.e. the dimensions of the simulated volume, the size of the subcells and all necessary micromagnetic constants, is loaded. The grid is extended and subdivided for the processors according to the parallelization scheme described above. The memory resources are allocated, the demagnetization tensor and its Fourier transform are calculated and the latter is stored. After the preconditioning, the initial magnetization distribution, given in the problem definition, is read in.

In the routine 'update  $E_{\text{tot}}/\mathbf{H}_{\text{eff}}$ ' the energies and the effective field is computed for the given magnetization array. First, the data at the inner edges of the subgrid introduced by the parallelization are exchanged via ghost cells, and the magnetocrystalline, exchange and Zeeman energy contributions are calculated directly. The demagnetization energy is calculated by taking advantage of all processors. Finally the effective field and the total energy of the magnetization state is determined.

Now the effective magnetic field of the initial magnetization is known and the relaxation algorithm for energy minimization can be applied. A

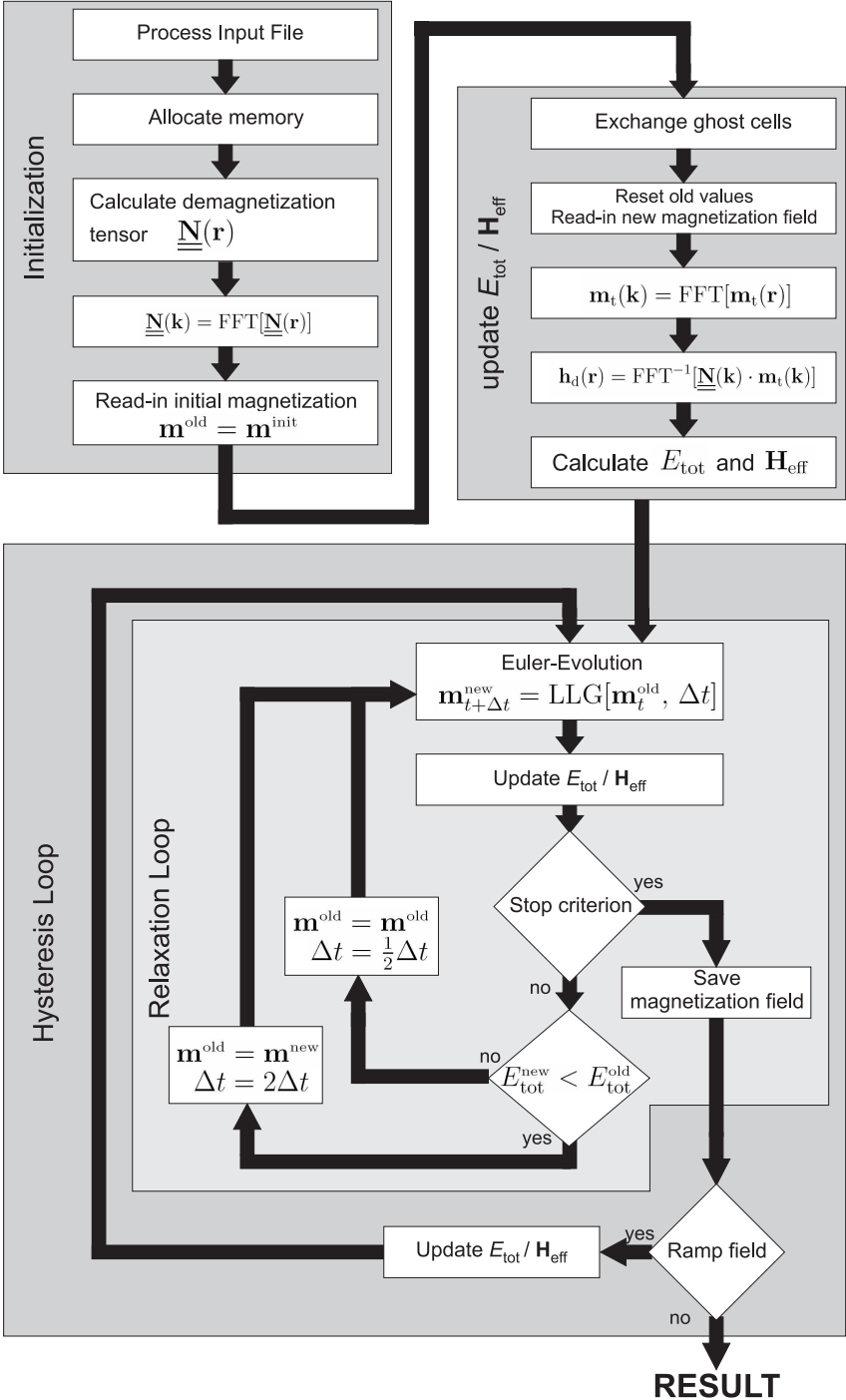


Figure 4.5: Flow chart of the micromagnetic simulator.

new state is determined using the LLG equation with a given time step  $\Delta t$  and with subsequent renormalization of the magnetization. The energy and the effective field associated with the new magnetization distribution are then updated using the routine 'update  $E_{\text{tot}}/\mathbf{H}_{\text{eff}}$ '. If the total energy of the new state is decreased  $E_{\text{tot}}^{\text{new}} < E_{\text{tot}}^{\text{old}}$ , the new state is accepted and the next iteration is performed with a time step increased by a factor of two. If  $E_{\text{tot}}^{\text{new}} > E_{\text{tot}}^{\text{old}}$ , the evolution of the old magnetization state is reevaluated for an iteration with a time step decreased by a factor of two.

The implementation of an adaptive time step algorithm allows to dynamically adjust the time step. In combination with a permanent energy comparison and renormalization of the magnetization distribution after an iteration step, a stable explicit scheme is ensured. The energy minimum cannot be overshoot due to an unadjusted time step, because in this case the LLG is reevaluated with a smaller time step. Several stop criterions are implemented to terminate the relaxation loop:

- difference between new and old magnetization state is smaller than a desired value
- minimum time step size has been reached and the total energy is increasing
- the torque acting on the magnetization due to the effective field is smaller than the desired value
- maximum total iteration step number has been reached

If one of the stop criterions is fulfilled, the magnetization distribution is considered as the equilibrium magnetization distribution. The state is saved in an output file together with the corresponding energy contributions. If according to the problem definition the external field is changed, the relaxation loop is restarted.

## 4.4 Test of the numerical code

To test the reliability of the micromagnetic simulator, the micromagnetic standard problem #1 ( $\mu\text{MAG}$  #1) has been solved and compared with published results [81]. For this purpose, a complete hysteresis loop for a thin permalloy film of 20 nm thickness and cuboidal shape with the lateral dimensions  $1 \times 2 \mu\text{m}^2$  is calculated from +50 mT to -50 mT with a constant step size of 1 mT. The magnetic field is applied along the long ( $x$ -axis) and

the short axis ( $y$ -axis) of the rectangle, respectively (cf. Fig. 4.6). The material parameters are chosen to be  $A = 1.3 \cdot 10^{-11}$  J/m,  $M_s = 8.0 \cdot 10^5$  A/m and a magnetocrystalline anisotropy  $K_{u_1} = 500$  J/m<sup>3</sup> with an easy axis along the long axis of the rectangle. The direction of the applied field was rotated by 1° counter-clockwise off the nominal axis to break the symmetry of the problem. As an initial configuration, a fully saturated magnetization along the applied field direction was assumed. Two different discretization levels have been used: a cell size of 20 nm for a direct comparison with the reported data, termed [cz20], and a cell size of 10 nm to assure a discretization of the grid comparable to the magnetostatic exchange length  $l_{\text{stat}} = \sqrt{2A/\mu_0 M_s^2} = 10$  nm, termed [cz10].

The published data for  $\mu$ MAG #1 [81] of calculated coercivity, remanent states and switching fields do not compare well. Besides possible programming errors, these differences can be attributed to the inappropriate methods applied for the calculation of the demagnetization energy. As pointed out in Subsec. 4.2.1 for a correct approximation of the magnetization distribution, the cell dimensions have to be on the order of the characteristic micromagnetic lengths. Two contributors calculated the demagnetization energy directly. To get a result in a reasonable time, they strongly reduced the number of interacting subcells to 800 [fr96a] and 814 [du96a]. A third contributor [lu96a] introduced 1800 cells but reduced the computational effort of the direct evaluation of the demagnetization energy by the truncation of magnetostatic interaction range. The coarse discretization, and a possibly inadequate cut off of the interaction, led to an apparent inconsistency of the submitted results. Therefore, the data from contributions [fr96a], [du96a] and [lu96a] were omitted. The coercive field and the average magnetization at remanence are summarized in Tab. 4.1. The results of the developed numerical code [cz20] and [cz10] agree with the published data [81] and demonstrate the reliability of the simulator.

The magnetization distribution at remanence after saturation, shown in Fig. 4.6 (e) and (f), is not affected by the grid discretization. The remanent magnetization pattern of the simulation is a typical flux closure pattern known from permalloy which is termed 'S' state. In absence of a magnetic field, a surprising variety of possible magnetic states exists as metastable solutions and their occurrence is strongly affected by the initial configuration. The 'S' state is not the ground state of the  $\mu$ MAG problem #1. For saturation, the high field state converts into the 'C' state, which is energetically slightly preferred over the 'S' state [111]. The main domain is magnetized along the long axis to minimize the magnetocrystalline and the magnetostatic energies. To further reduce the stray field energy, the magnetization also lines up along the short edges by forming edge states at the cost of



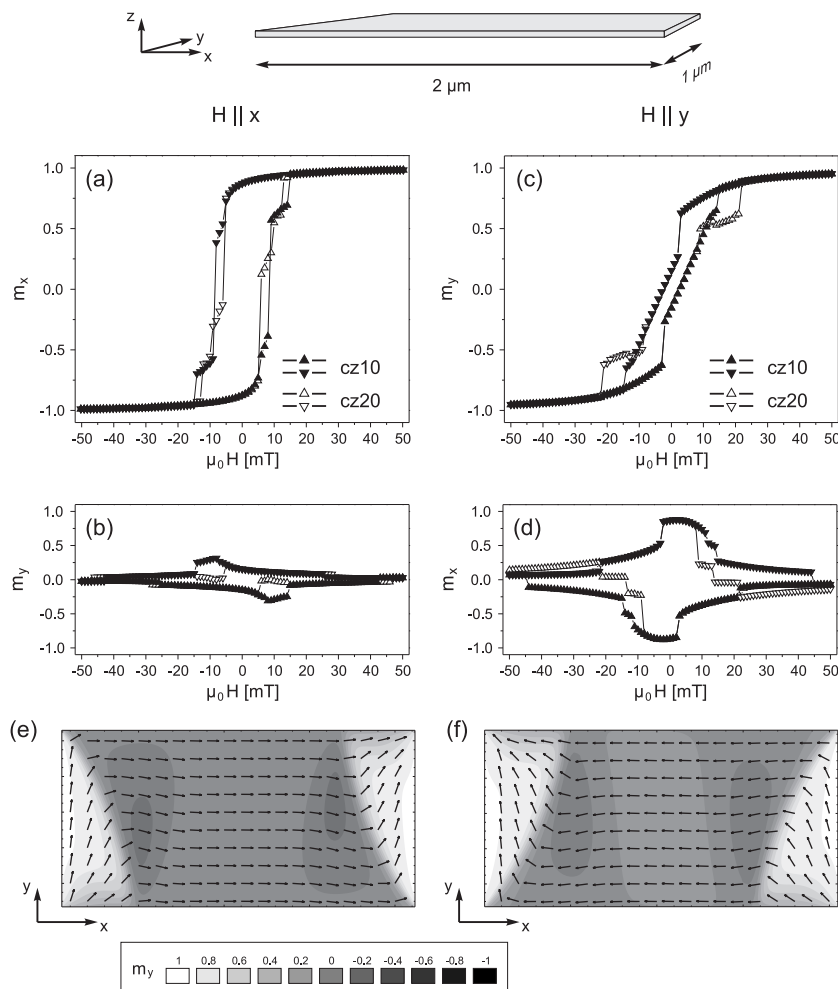


Figure 4.6: Results of the standard  $\mu$ MAG problem #1. The geometry is shown above; the largest dimension is along the  $x$ -axis. Hysteresis loops applying the field along the long axis ( $x$ -axis) and the short axis ( $y$ -axis) for both magnetization components, parallel and perpendicular to the applied field, are visualized. (a) Magnetic field along the long axis and magnetization parallel to the field, (b) magnetic field along the long axis and magnetization perpendicular to the field, (c) magnetic field along the short axis and magnetization parallel to the field, (d) magnetic field along the short axis and magnetization perpendicular to the field. The magnetization distribution at remanence after saturation along the long axis and the short axis are shown in (e) and (f). The legend indicates the magnetization values of  $m_y$ .

exchange and magnetocrystalline energy. The orientation of the magnetization pattern depends on the initial saturation and the direction of the applied field. Since the applied field was rotated  $1^\circ$  counter-clockwise off the nominal axis, a magnetization along the  $+y$ -direction is preferred for the edge domains in Fig. 4.6 (e). For a field applied along the short axis, the  $-x$ -direction is preselected by the field, see in Fig. 4.6 (f). Saturating the moments along the long axis or the short axis does not affect the remanent state of the structure, independent of the discretization depth.

The hysteresis curves presented in Fig. 4.6(a-d) are depending on the cell size. For the calculation of the hysteresis along the short axis ( $y$ -axis), they only differ in the annihilation field of the edge domains, which is higher for the result of [cz20] [cf. Fig. 4.6(c)]. Similar results were obtained for the coercitivity and average magnetization. This is in accordance with [mo96a] and the average components of magnetization  $\langle m_x \rangle$  and  $\langle m_y \rangle$  also agree. Besides [zn97a], the other contributions to the standard problem #1 did not reveal an 'S' state as the remanent state but a magnetization distribution with a Landau state-like pattern. It has to be noticed that in case of [pb97a] an 'S' state is formed at an applied field of  $-1$  mT. The reason for the deviation of the remanent pattern of [ts96a] and [ts96b] can be possibly attributed to the differences of the applied methods. Here a finite element

Table 4.1: Comparison of coercive fields and remanent magnetization of the standard problem #1 of the calculated results with published data from Ref. [81]. The names are according to the submission codes of the NIST Center for Theoretical and Computational Materials Science (CTCMS). The names [cz20] and [cz10] are the results of this simulator for a cell size of 20 nm and 10 nm, respectively.  $\langle m_x \rangle$  and  $\langle m_y \rangle$  are the averaged components of magnetization.

		literature results					simulator	
		[mo96a]	[ts96a]	[ts96b]	[pb97a]	[zn97a]	[cz20]	[cz10]
long axis	$\mu_0 H_c$	4.9	13.0	5.3	4.9	13.8	5.8	9.3
	$\langle m_y \rangle$	0.15	0.00	0.13	0.16	0.24	0.15	0.15
	$\langle m_x \rangle$	0.87	0.75	0.86	0.86	0.89	0.87	0.87
short axis	$\mu_0 H_c$	2.5	9.3	7.5	3.4	6.6	2.2	2.2
	$\langle m_y \rangle$	0.15	0.37	0.27	0.60	0.28	0.15	0.15
	$\langle m_x \rangle$	0.87	0.01	0.09	0.53	0.88	0.87	0.87

method has been applied to  $\mu$ MAG #1 with average cell dimensions of  $103 \times 103 \times 8.0 \text{ nm}^3$  and  $66.0 \times 67.3 \times 20.0 \text{ nm}^3$ , respectively.

The data of [cz20] and [cz10] for the calculation of the hysteresis loop along the  $x$ -axis is also affected by the discretization. The coercive field is different, revealing a larger value of 9.3 mT [cz10] for a smaller cell size compared to 5.8 mT [cz20] [cf. Fig. 4.6(a)].

Although both values are in the range of published results (compare Tab. 4.1) it is worth to discuss the discrepancy. A detailed investigation of the switching behavior of thin-film elements of this size has revealed two irreversible magnetization jumps in the hysteresis curve: a small first jump at 4.9 mT and a second jump corresponding to the switching field (8.8 mT) [111]. At the first jump, a relatively stable three-domain configuration is formed. The areas of almost initiated reversal in front of the edge domains branch off and merge in the middle of the structure. At the second jump, the switching is completed and an antiparallel 'S' state forms. For a large cell size of 20 nm [cz20] the merging middle domain already nucleates at 5.8 mT, accompanied by the generation of four vortices. The reason is a faded tendency to correctly determine the energy of a vortex due to the coarse discretization [112]. Two vortices are driven out at 10 mT, while at 17 mT all vortices are annihilated. For the calculation with a finer grid only a single vortex nucleates during reversal at  $-10$  mT which is finally annihilated at  $-16$  mT.

By applying the simulator to the  $\mu$ MAG problem #1 and comparing with the published data [81, 112] it has been shown that the results of the developed micromagnetic simulator are consistent with the reported data. Deviations can be attributed to the insufficient discretization level used in the reported simulation. The hysteresis loop for fields applied along the long axis is in good agreement with the the investigation of the switching behavior of thin-film elements, where the number of cells ( $256 \times 128 \times 2$ ) is equivalent to the cell size used in [cz10].

## 4.5 Extension to realistic MFM response

Using the micromagnetic simulator, the contribution of the individual energy terms to the total energy, the averaged components of the magnetization as well as the vector field of the magnetization is calculated. These results can be readily correlated to SQUID or XMCDPEEM measurements. However, a direct connection of simulator and MFM results is desired along with the capability to calculate the MFM response of realistic micromagnetic structures. With the extension to calculate a realistic MFM response the simulator is becoming the key element for micromagnetic investigations, bridging the two

complementary experimental techniques and allows for the study of the internal micromagnetic structure. It is considered as an improvement of the analytical method presented in Subsec. 3.3.2. The main advantage of this approach is that arbitrary, three-dimensional sample and tip magnetization distributions can be simulated in reasonable times.

**Description of the simulation procedure:** Since the stray field and the demagnetization field are of same origin — the first is defined outside, the latter inside the ferromagnetic volume — the stray field is evaluated extending the grid of the simulator above the sample. This leads to an even larger array and calculating the demagnetization energy by the use of the Fast Fourier transformation and convolution theorem is the more advantageous. The magnetostatic energy between tip and sample is given by

$$E_{\text{ms}} = \sum_i \mathbf{M}_{\text{tip}}(\mathbf{r}_i) \cdot \mathbf{H}_{\text{s}}(\mathbf{r}_i), \quad (4.31)$$

where  $\mathbf{M}_{\text{tip}}(\mathbf{r}_i)$  is the magnetization of the tip and  $\mathbf{H}_{\text{s}}(\mathbf{r}_i)$  the stray field of the sample at tip cell  $i$ . Under the assumptions made in Subsec. 3.3.2, namely that magnetization of tip and sample are absolutely hard and normal vector of the cantilever oscillation is parallel to sample normal  $\mathbf{n} = \mathbf{e}_z$ , the MFM response is thus proportional to the second derivative of the magnetostatic energy between tip and sample with respect to the  $z$ -direction. The common 5-point approximation is used for obtaining the second derivative of the magnetostatic energy by numerical differentiation:

$$E''_{\text{ms}} = [-E_{\text{ms}}(z_0 - 2\Delta z) + 16E_{\text{ms}}(z_0 - \Delta z) - 30E_{\text{ms}}(z_0) + 16E_{\text{ms}}(z_0 + \Delta z) - E_{\text{ms}}(z_0 + 2\Delta z)]/12(\Delta z)^2. \quad (4.32)$$

The complete MFM image is then obtained by raster-scanning the tip across the sample in steps of  $\Delta x$  and  $\Delta y$  and calculating  $E''_{\text{ms}}$  at each scan position.

For the implementation of the MFM response in the simulator, a tip of finite size is placed at a certain height  $z_0$  above the magnetic sample, and the entire structure is discretized in all three dimensions (cell size:  $\Delta x \times \Delta y \times \Delta z$ ). The tip is assumed to have a constant magnetization and a tip shape defined by the radius of curvature  $r_{\text{tip}}$ , the side angle  $\gamma$  and a coating thickness  $\delta$ , see Fig. 4.7 (b). It has to be noted that, in principle, arbitrary tip magnetization can be included in the simulation. This also applies to magnetization distributions obtained for completely relaxed tip-sample systems. In the present case, the tip is approximated by a cone with

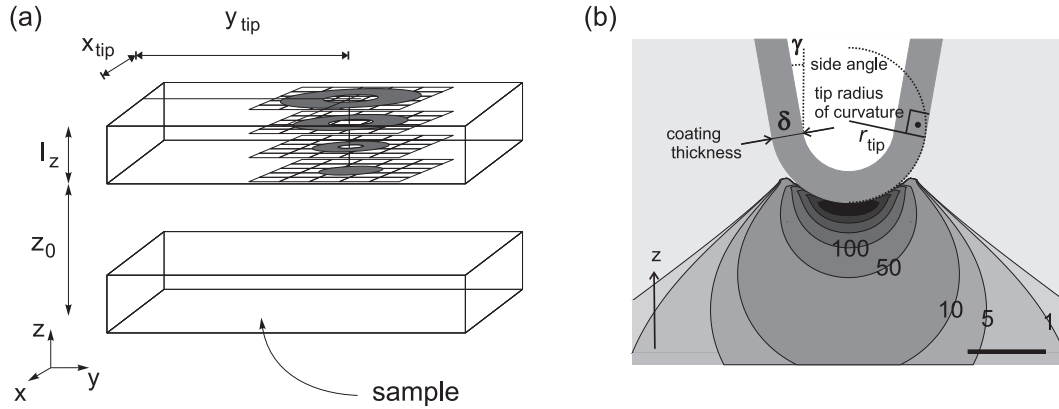


Figure 4.7: (a) Sketch of the implementation of the MFM response in the micromagnetic simulator. The grid is extended above the sample and the demagnetization field is calculated. The second derivative of the magnetostatic energy of tip and sample is calculated for each tip position  $(x_{tip}, y_{tip})$ , forming an MFM response image. (b) Geometrical model of the tip showing the cone opening angle  $\gamma$ , the coating thickness  $\delta$ , and the tip radius of curvature  $r_{tip}$ . Contours of the  $z$ -component of the calculated tip stray field are shown for  $\gamma = 10^\circ$ ,  $\delta = 40$  nm, and  $r_{tip} = 100$  nm. The values are given in mT in the figure. The bar on the lower right hand-side represents a length of 100 nm.

opening angle  $\gamma$  with a continuous transition to a spherical tip cap of radius  $r_{tip}$ .

For simplicity, the magnetization is further assumed to be oriented along the  $z$ -axis. A finite tip height  $l_z$  is considered, yielding  $n = l_z/\Delta z$  number of layers in the tip using the discretization mentioned above. Each layer consists of a ring of magnetic material. The simulation of arbitrary shapes in cartesian coordinates leads to structural boundaries. To account for these effects, the magnetization at the boundary cells are weighted by the number of cornerpoints within the magnetic tip coating. Figure 4.7 (b) shows the simulated stray field of the tip with the same parameters used for the tip in Subsec. 3.3.2.

**MFM response:** Figure 4.8(a) shows a gray-scale image of the MFM response at a working distance of  $z_0 = 100$  nm for the sequence of three oppositely magnetized, neighboring domains (cf. Fig. 3.9). The simulated structure is the same used for the calculation using the analytical approach presented in Subsec. 3.3.2 to allow a comparison of both methods. The contrast is dominated by bright and dark areas, located at the ends of the three

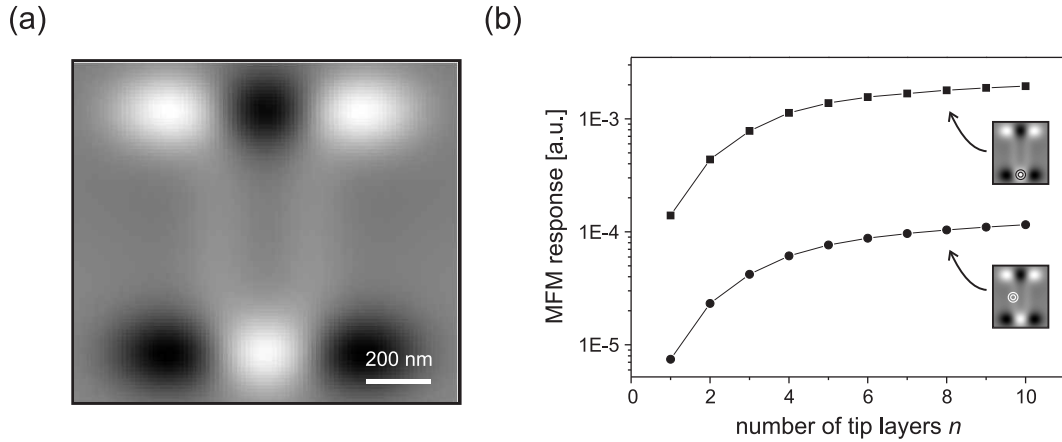


Figure 4.8: (a) Simulated MFM image of the micromagnetic domain structure (cf. Fig. 3.9) using the micromagnetic simulator. (b) Logarithmic plot of the MFM response as a function of the number of tip layers ( $\Delta z = 10$  nm) above an area of maximum contrast caused by an in-plane domain (upper curve) and an out-of-plane magnetization (Bloch wall, lower curve), respectively. The positions are indicated in the respective insets. The working distance is  $z_0 = 100$  nm.

simulated domains, the bright areas are centered around the borders of the geometrical dimensions of the domains (length  $\times$  width =  $700 \times 190$  nm). Between the domains, the Bloch wall yields a much weaker contrast than the dominating contrast from the in-plane domains ( $\approx 1/10$ ). As a consequence, a series of oppositely magnetized domains appears as a meander-like structure in MFM experiments.

The influence of the tip sampling has to be carefully investigated. For this purpose the MFM response atop of an area of maximum contrast caused by an in-plane domain and an out-of-plane magnetization (Bloch wall) is evaluated. Figure 4.8 (b) shows logarithmic plots of the MFM response as a function of the number of tip layers  $n$  for the in-plane domain maximum (upper curve) and the out-of-plane contrast maximum (lower curve), respectively. The step size in the  $z$ -direction is 10 nm. As expected, the MFM signal is about an order of magnitude weaker above the center of a Bloch wall compared to an in-plane magnetized domain. From the curves, it is obvious that the MFM response starts to converge for  $n$  at least  $> 10$ .

Finally a quantitative comparison of the two simulation methods on the basis of the analyzed three-domain structure (cf. Fig. 3.9), incorporating simplified Bloch walls where the rotation of the magnetic moments points

out of the sample plane is given. In both cases, a step size of 10 nm was used for the calculation. The simulation parameters were:  $M_{\text{tip}}^{\text{rem}} = 800$  kA/m,  $M_{\text{sample}}^{\text{rem}} = 700$  kA/m, working distance  $z_0 = 100$  nm,  $r_{\text{tip}} = 100$  nm,  $\delta_{\text{tip}} = 40$  nm, and  $\delta_{\text{sample}} = 180$  nm. Figure 4.9 shows linescans across an in-plane domain (labeled ①, above) and across the two Bloch walls (②, below), as indicated in the image. For both types of contrast features, the plots agree qualitatively very well. In general, it is observed that the magnitude of the signal obtained using the micromagnetic simulator is smaller than using the analytical method. This is a result of the coarse discretization of the tip. The tip shape is not sufficiently approximated by the cells causing an underestimation of the magnetization of the boundary cells in the case of a cell dimension of 10 nm.

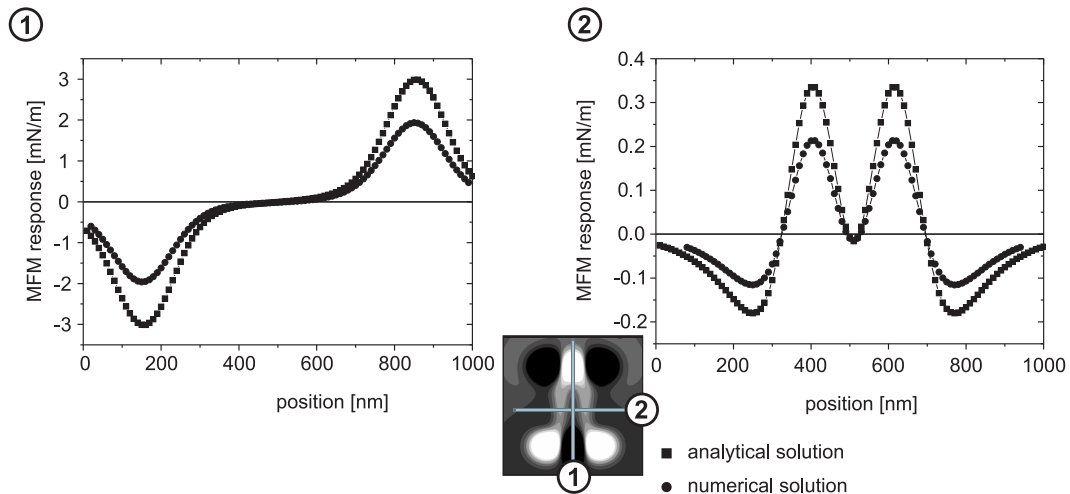


Figure 4.9: Comparison of the calculated MFM response employing the analytical method (squares) and the numerical method (circles). The plots along the lines of maximum contrast across an in-plane domain are labeled ① and the across a (simplified) Bloch wall ②.

The advantages and limitations of the analytical method can be summarized as follows. First of all, quantitative results are obtained for the MFM response. In order to simulate real MFM problems, the van der Waals interaction can be easily implemented to account for topographically-induced contrast. Moreover, arbitrary tip shapes can be approximated by a distribution of dipoles as described above. The major limitation is the large computational effort. Moreover, only the interaction between magnetically hard tips and samples can be simulated, i.e. relaxed tip magnetization cannot easily be obtained by iterative energy minimization.

The numerical method implemented in the micromagnetic simulator is characterized by the fact that arbitrary sample and tip magnetization can be treated. This also includes the possibility to relax the tip and the sample, or the entire tip-sample system in order to investigate their mutual influence [75, 116]. An additional advantage of the method is the fast computing speed (for an unrelaxed tip-sample system) which is due to the fact that the convolution theorem is employed for the calculation of the stray field. The main shortcoming is the necessary discretization of the system, especially of the tip, which leads to an underestimation of the magnetization for coarse grids. This can be somewhat compensated for by a denser sampling grid, however, due to the involved fast Fourier transform, the size of the grid is limited by the memory that can be handled by the processor.

Table 4.2 lists the comparison of the figures-of-merit for the two methods. In principle, there is independent of the approach a trade-off between precision, i.e. the quantitative character of the results, and computing speed. In terms of the ease of simulating a given experimental problem, the analytical method has a clear advantage as it allows for a straightforward translation into the initialization file. In case of the analytical problem, the implementation is tedious and more time-consuming. The precision of the results obtained with the two methods is, in principle, comparably high. The analytical solution delivers quantitative results, whereas for the numerical solution, the precision strongly depends on the discretization of the problem. However, the density of the simulation grid is limited by the addressable computer memory for the fast Fourier transform. The numerical method is characterized by its fast computing properties. For the equivalent problem (cell size dimension  $\sim 10$  nm), only 600 s are necessary to obtain the MFM image compared to  $> 1.6 \cdot 10^5$  s in case of the analytical method. In general, the computing

Table 4.2: Comparison of the capabilities of the analytical versus the numerical method.

	Analytical method	Numerical method
Ease of implementation	straightforward	time-consuming
Precision	high	depends on discretization
Computation speed	slow	fast
Flexibility	low	high
Extensibility	difficult	easy



time scales with  $N \log N$  for the numerical method compared to  $N^2$  for the analytical method, where  $N$  is the number of grid points. Moreover, the advantages of the numerical method are the flexibility, i.e. the capability to deal with arbitrary sample and tip magnetization, and the extensibility, i.e. the possibility to implement the mutual tip-sample disturbance.

## Chapter 5

# The micromagnetic structure of MnAs-on-GaAs

In this Chapter, the experimental investigation of the micromagnetic structure by MFM, XMCDPEEM and of micromagnetic simulations is presented. The focus is on the regular stripe structure. First, the MFM results are explained by qualitative MFM response simulations (Subsec. 3.3.2) introducing a domain classification scheme. The assumption of more than one domain across the width of the stripes allows for a good agreement between simulation and MFM response, as confirmed by XMCDPEEM measurements. Nevertheless, the classification scheme involves head-on domains, which are energetically highly unfavorable.

Micromagnetic simulations reveal that the domain transition between head-on domains is a domain wall only right at the surface of the film. In depth, a diamond domain with an out-of-plane magnetization separates the head-on domains. The symmetry of the magnetocrystalline anisotropy favors the magnetization in the basal plane, thus for film thicknesses larger than a critical value, a nucleation of out-of-plane magnetized domains is energetically possible.

In Sec. 5.1, the classification scheme and the simple micromagnetic model based on MFM results is analyzed, and supporting simulations are presented. These investigations are extended in Sec. 5.2 by the use of the micromagnetic simulator, confirming the basic domain types of complex three-dimensional structure. In Sec. 5.3, a description of zig-zag-shaped domain transitions finalizes the discussion about the intra-stripe domain structure. The inter-stripe coupling is analyzed in detail in Sec. 5.4, followed by the investigation of the micromagnetic structure of MnAs/GaAs(111)B in Sec. 5.5.

## 5.1 Simple micromagnetic model

The classification of the magnetic domains in MnAs films on GaAs(001) is based on the number of domains across the width of the ferromagnetic stripe, i.e. along the easy axis direction. A typical MFM image is shown in Fig. 5.1. Three MFM-response patterns are highlighted in Fig. 5.1, marked (I), (II), and (III). The in-plane  $a$ -axis is the easy axis of magnetization and the relatively large effective anisotropies ensure that virtually all magnetic moments are aligned along the easy axis. In the simplest configuration, type (I), the stripe is either magnetized parallel or antiparallel to the in-plane  $a$ -axis direction. In the demagnetized state, the individual bar magnets line up with alternating orientation along the stripe. In the transition region between two antiparallel aligned domains the magnetization gradually rotates from parallel to antiparallel in the plane of the domain wall, parallel to the wall normal. The reason is a smaller effective anisotropy normal to the film plane. Therefore, the domain transition is a  $180^\circ$  Bloch wall. The bar magnet-like domains, together with the  $180^\circ$  Bloch wall, lead to the meander-shaped contrast in MFM (cf. Subsec. 3.3.2).

The type (II) domains have two possible configurations of the two subdomains, illustrated in Fig. 5.2, with the moments facing or pointing away from each other. Triple-split domains [type (III)] have a more complex appearance. They also exist in an unevenly split subdomain partitioning (see Fig. 5.1). From MFM temperature cycles it is known that the third subdomain appears gradually upon cooling, leading to an even partitioning ratio at room temperature.

In order to understand the domain structure that leads to the apparent MFM image, simulations of the MFM contrast are performed. The domain structure is modeled by an arrangement of bar magnets with constant magnetization using the MFM response model introduced in Subsec. 3.3.2. For the calculations, the tip is assumed to be spherically shaped with a radius of curvature of 120 nm. The tip magnetization is assumed to be completely oriented along the tip axis. The tip magnetization (Si cantilevers coated with a 80 nm Cr-Co ferromagnetic layer [82]) is saturated along the tip axis with a permanent magnet, which makes the MFM predominantly sensitive to the out-of-plane component of the sample's stray field. A reasonable arrangement of the domains based on the proposed classification scheme is used. The total stray field consists of two different contributions: domains with an in-plane magnetization along the easy axis and the Bloch walls exhibiting an out-of-plane magnetization. This results in different distance dependencies of the in-plane and out-of-plane magnetic stray field components in the

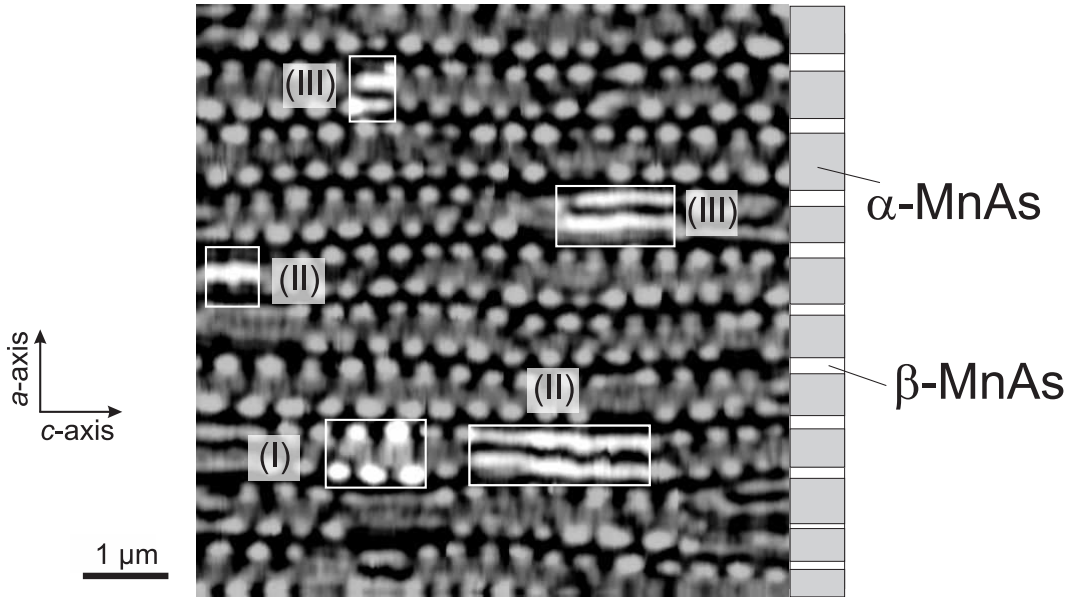


Figure 5.1: Typical domain pattern of a 180-nm-thick MnAs film at room temperature. Characteristic domain configurations, classified by the number of subdomains along the  $a$ -axis direction, are highlighted. The type (I), (II) and (III) configuration refer to one, two, and three subdivisions, respectively.

$z$ -direction. The thickness of the Bloch wall  $w_{\text{BW}} = 2\sqrt{A/K_{\text{eff}}^{(1\bar{1}00)}}$  was estimated to be roughly 10 nm. Domain types (I) - (III) has been modeled for a 700 nm wide ferromagnetic stripe and the MFM contrast has been calculated for a working distance of 100 nm.

Figure 5.2 shows a comparison of the measured and the simulated MFM contrast for the proposed domain configurations of Fig. 5.1. Type (I) domains, where the stripes are single domain across their width, are typical for the upper and lower temperature limit in the  $\alpha$ - $\beta$  coexistence region. Very narrow stripes tend to be also single domain along the MnAs[0001] direction; their length is up to several  $\mu\text{m}$ . At higher resolution, bright areas are visible at the ends of the antiparallely magnetized bar magnets. In-between the domains, the contrast is due to differently oriented Bloch walls, either rotating the moments through the direction pointing out of or into the surface plane, respectively. This contrast is modeled correctly, as shown on the left-hand side of Fig. 5.2, assuming the sketched distribution of magnetic moments. It has to be noted that for domain types (II) and (III), neither a Bloch nor a Néel domain wall along the length of the stripes was included in the simulations.

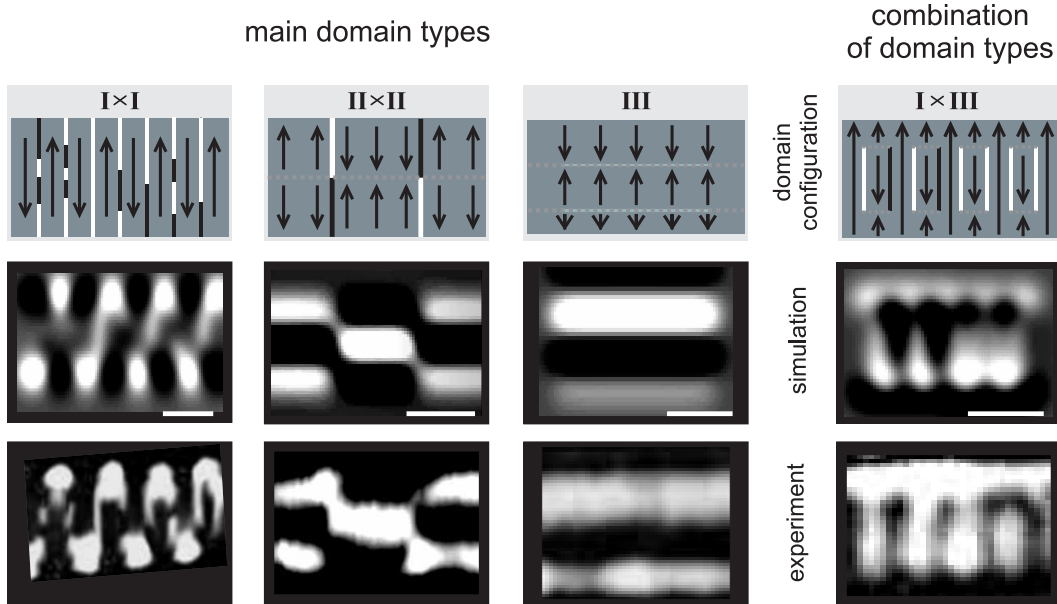


Figure 5.2: Comparison of the measured domain patterns (bottom) with the simulated MFM contrast (middle) for the common domain types (I)-(III) in MnAs films of Fig. 5.1. Black and white lines in the domain configuration picture (top) indicate Bloch walls pointing out of and into the surface plane, respectively. The dotted gray lines mark the border between subdomains. The bars correspond to 500 nm.

More complex MFM patterns can be deduced from the classification scheme by arranging different domain types along the MnAs[0001] direction ( $c$ -axis). Two prominent patterns, termed (II×II) and (I×III) according to the involved domain types, are shown in Fig. 5.2. The asymmetry in the MFM picture is not due to the tip shape, but due to Bloch walls between the two subdomains as indicated by black and white lines in the domain configuration images. The orientation of the Bloch wall was obtained by finding the best agreement with the simulated image. Similarly, the Bloch wall orientation also affects the appearance of the (I×III) domain pattern. Basically, the (I×III) pattern is supposed to be a sequence of type (I) and type (III) domains with variable length and width of the subdivision. The width and the length were used as fitting parameters for the simulation.

XMCDPEEM measurements support the classification scheme of the observed domains according to the number of sub-domains. Figure 5.3 shows a XMCDPEEM image of a 180-nm thick MnAs film at room temperature [10], yielding the magnetization component of the surface layers of the sample

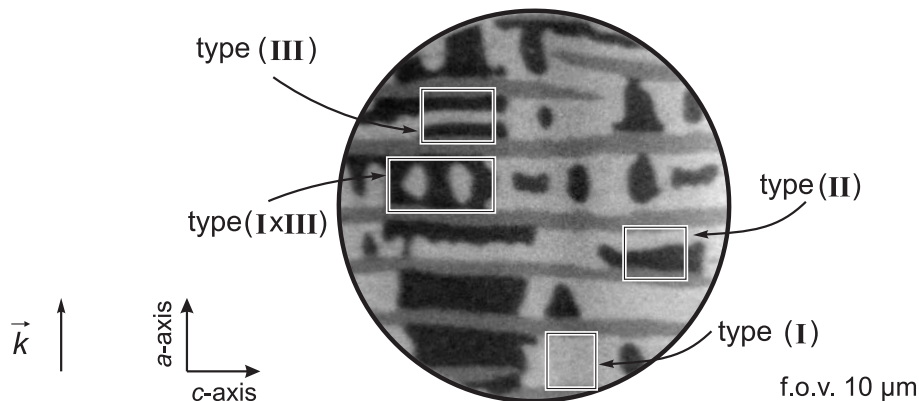


Figure 5.3: XMCDPEEM image of a 180-nm-thick MnAs film at room temperature revealing the different domain types (I), (II), and (III) [10]. The direction of incidence of the light is along the  $a$ -axis.

in the direction of incident photon beam. The ferromagnetic stripes can be identified by the areas of black ( $\vec{M} \uparrow \parallel \vec{k}$ ) and white ( $\vec{M} \downarrow \parallel \vec{k}$ ) contrast in the magnetic image. They are separated by non-magnetic areas (gray contrast). The XMCDPEEM image clearly indicates that the ferromagnetic  $\alpha$ -MnAs stripes break up into sub-domains of opposite magnetization along the easy  $a$ -axis. Typically up to three subdomains [cf. areas marked by rectangles in labeled (I)-(III)] and also the (I $\times$ III) sequence are observed.

Although the simple micromagnetic model of bar magnets is consistent with the experimental results obtained from independent imaging techniques, it has a major drawback: it is physically unreasonable. A domain transition along the main direction of magnetization is energetically unfavorable. This inconsistency stimulated three-dimensional micromagnetic simulations of the domain structure of MnAs stripes that will be discussed in the next Section.

## 5.2 The intra-stripe domain structure

So far, MnAs was treated as a system with an easy axis in-plane and an out-of-plane intermediate hard axis. The inconsistency of the proposed simple domain arrangement model makes it necessary to revisit the micromagnetic properties of MnAs. In fact, the hexagonal basal plane of MnAs is an easy plane of magnetization since the magnetocrystalline anisotropy constant  $K_{u_1}$  has a large negative value [23]. Shape anisotropy in thin films selects the in-plane  $a$ -axis as the easy axis of magnetization. As a consequence of the

easy-plane property of MnAs, thicker films exhibit truly three-dimensional magnetization patterns, where the domain structure in the easy plane (i.e. in-depth) resembles closure domains.

For the simulation of the magnetization distributions, we have assumed the following values for the magnetic parameters of MnAs: saturation magnetization  $M_s = 4 \cdot 10^5$  A/m, exchange stiffness constant  $A = 1 \cdot 10^{-11}$  J/m, and magnetocrystalline anisotropy constants  $K_{u_1} = -7.2 \cdot 10^5$  J/m<sup>3</sup> and  $K_{u_2} = -3.6 \cdot 10^5$  J/m<sup>3</sup>. The dimensions of subelements of the simulation grid were chosen to be on the order of the magnetocrystalline and the magnetostatic exchange lengths. Different thicknesses of the ferromagnetic stripe, ranging from 50 to 200 nm, and ratios of width over thickness were assumed. To account for the stripe structure, the dimension along the  $c$ -axis was always at least three times larger than the width. As a starting configuration, the ferromagnetic stripes were assumed to be randomly magnetized. The distribution was relaxed towards the energy minimum in the absence of an external magnetic field.

Figure 5.4 shows cross-sectional views in the easy plane of the resulting pattern of ferromagnetic  $\alpha$ -MnAs stripes. In general, four different remanent magnetization states are found depending on the geometry of the structure: (a) 'S' state, (b) Landau state, (c) diamond state, and (d) double diamond

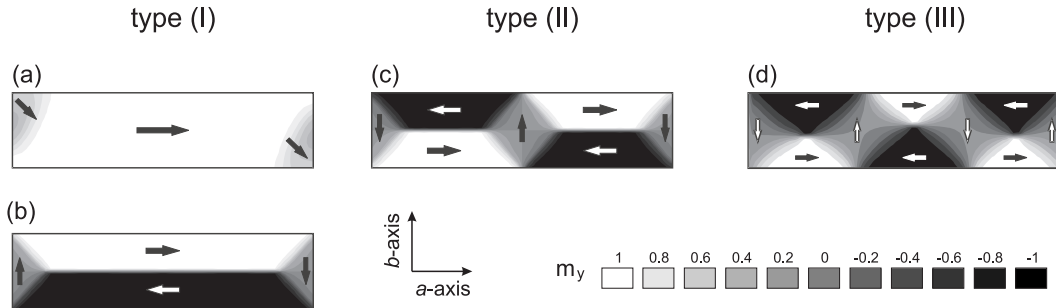


Figure 5.4: Magnetization states of MnAs in the easy plane (cross-sectional view in-depth cut along the  $a$ -axis direction): (a) 'S' state, (b) Landau state, (c) diamond state and (d) double diamond state, obtained by three-dimensional micromagnetic simulations. The 'S' and the Landau states lead to the observed type (I) domains, the diamond state results in the type (II) domains and the double diamond state in type (III) domains, respectively. The magnetization component ( $m_y$ ) along the  $a$ -axis is represented in grayscale. The legend indicates the magnitude of  $m_y$ . Arrows are added to indicate the magnetization directions.

state. They give rise to the commonly observed type (I) (a,b), type (II) (c), and type (III) (d) domains. The magnetic pattern in the basal plane are known from soft magnetic thin film elements with low anisotropy and sufficiently large size. The shape of these films allows only an in-plane magnetization, and the low magnetocrystalline anisotropy does not prefer an easy magnetization direction. Thus the demagnetization energy can be reduced by the formation of flux-closure patterns at the cost of exchange energy [53]. In the case of MnAs stripes, the flux closure pattern can be formed in the basal plane (the plane with no preferred magnetocrystalline anisotropy), which is oriented perpendicular to the film plane. The  $c$ -axis is the hard axis, which strongly impedes a magnetization component in this direction. It has the same function as the shape anisotropy in soft magnetic thin film elements. The easy plane character of the magnetocrystalline anisotropy acts like an additional ‘degree of freedom’, giving rise to out-of-plane magnetized domains. This is also the reason for the inconsistency of the simple bar magnet model, as this was inspired by the integral magnetic properties of MnAs films. The domain transition along the  $a$ -axis is neither of Bloch wall nor of Néel wall type, but an out-of plane magnetized domain in depth.

The formation of out-of-plane magnetized domains, and consequently the occurrence of type (II) and type (III) domains, is mainly governed by the thickness of the MnAs film. For sufficiently thick films, it is energetically favorable to nucleate an out-of-plane magnetized domain by the introduction of domain walls, i.e. at the cost of exchange energy. The critical thickness is estimated to be around 100 nm. Again, it has to be noted that this out-of plane magnetized domain does not create an additional stray field but allows for the formation of a flux-closure pattern and thus an overall reduction of demagnetization energy. The magnetization states are not only affected by the thickness of the film, but also by the geometrical ratio of depth-over-width, which is tuned by the temperature.

In the following, the appearance of the three-dimensional intra-stripe structure in MFM and XMCDPEEM will be compared and discussed. Figure 5.5 shows the micromagnetic contrast obtained by XMCDPEEM (a) and MFM (b) of a 180-nm-thick MnAs film. For the XMCDPEEM images only the topmost layers contribute to the contrast. On first sight, the MFM contrast is by far more complex. As MFM is sensitive to the out-plane component of the stray field, the measured contrast is a result of the stray field associated with the sub-domains and stripes being separated by nonmagnetic material. Thus, in MFM the effect of a reduced stray field should be recognized. Indeed, a strong bright contrast of the type (I) domain, revealing a large stray



field at the edges of the stripe, is measured compared to the stray field of type (II) domains. Furthermore, in the case of type (II) domains another feature is visible in MFM at the edge of  $\alpha$ -MnAs, which is not apparent in XMCDPEEM. In areas of repulsion (dark contrast) a thin white line is visible [cf. in Fig. 5.5(b)]. This is a convolution artifact introduced by measuring in constant frequency shift mode. To maintain the frequency shift, the cantilever is positioned at very short tip sample distances, where topographic features are becoming strongly pronounced.

In general, the statistics of the three domain types yield the same results for both methods averaged over many images. Besides the good agreement of simulated intra-stripe structure and experimental MFM and XMCDPEEM results, two main discrepancies of stray field pattern and surface magnetization distribution are apparent. First, MFM shows that type (I) domains are typically an alternating sequence of oppositely magnetized areas along the  $c$ -axis, whereas they appear as a single domain state extending along the  $c$ -axis in XMCDPEEM. The alternating sequence of oppositely magnetized type (I) 'segments' is observed in MFM for MnAs films with thicknesses down to 80 nm. In contrast, for thicknesses below 80 nm, the stripes appear to be single domain along the  $c$ -axis also in MFM measurements. Second, type (II) and type (III) domains reveal a striking substructure in MFM composed of fine straight or tilted comb-like features.

The remaining differences can be understood in the context of invasive ef-

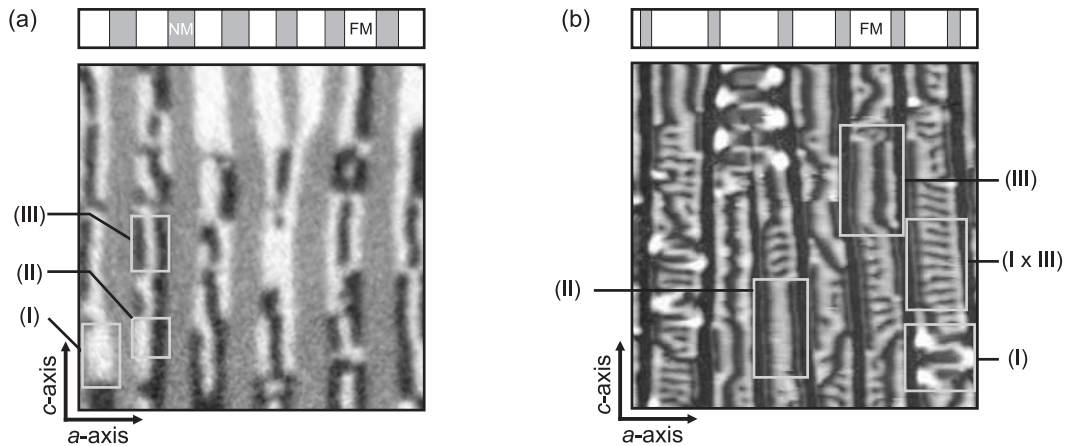


Figure 5.5: Comparison of the micromagnetic imaging ( $5 \times 5 \mu\text{m}^2$ ) of a 180 nm thick MnAs film by (a) XMCDPEEM and (b) MFM at different spots. The position of the ferromagnetic (FM) and nonmagnetic (NM) stripes is indicated above.

fects of the MFM tip. First, the situation for films with thicknesses up to the critical thickness of 100 nm is discussed. The preferred domain configuration is the 'S' state, associated with a high stray field. Single ferromagnetic stripes exhibit a high demagnetization energy for type (I) domains extending along the  $c$ -axis, which can be efficiently reduced by an antiparallel alignment of neighboring domains. In XMCDPEEM no activation processes are involved in the measurement procedure to provide an energy to transform to a sequence of antiparallel domains. However, in MFM experiments the magnetic tip is operated near the sample surface. Simulations of the tip's stray field yield a strength of 5 mT at working distances of 50 nm, i.e. the magnetic tip provides a laterally confined field. The tip field seems to be sufficient to flip parts of the stripes to form antiparallel domains along the  $c$ -axis. It is remarkable that for extended alternating type (I) domains the width is comparable to the film thickness – a signature of an optimal demagnetization.

Once the stripe reveals an antiparallel arrangement, further scanning the area with the magnetic tip does not alter the domain configuration; the initial switching is irreversible. Sudden tip jumps due to an interaction are rarely observed in experiments and it is assumed that the initial switching occurs already upon approaching the sample surface with the tip. The invasive effect of the MFM tip is not observed for thinner films, as stated above. This can be attributed to the thickness dependence of the coercive field [20, 118]. For films thicknesses below 100 nm the coercive field increases and the stray field of the tip is not sufficient to induce domain flipping.

For larger film thicknesses the situation is more complicated since now the tip may influence the in-depth structure. The comb-like structure [cf. Fig. 5.5(b), labeled (I) $\times$ (III)] is more often observed in MFM than in XMCDPEEM images and can thus most likely be attributed to a tip-induced effect. The interaction of tip and sample is smaller due to the reduced stray field of type (II) and type (III) domains. For MFM experiments in the constant force gradient mode, the tip is positioned closer to the sample surface to maintain the total force gradient, causing a stronger distortion of the sample magnetization by the stray field of the tip. There are a few possible scenarios. As the easy-plane character of the basal plane of MnAs allows domains with out-of-plane magnetization, the tip magnetization is aligned with one of the vertically magnetized regions. Thus, the tip might be able to drag these diamond domains across the stripe, which causes bright fine lines elongated in the  $a$ -axis direction possibly resulting in the comb-like structure. On the other hand, the tip's stray field is not large enough to drive out type (II) and type (III) domains.

To finally answer the question of tip-induced distortions of all domain types, micromagnetic simulations of both tip and sample are needed. For

the calculation of these effect, the MFM-response simulation tool (Sec. 4.5) has to be extended to a dynamic simulation of the combined tip and sample system.

### 5.3 Zig-zag domain transitions

The investigation of thicker MnAs films ( $\gtrsim 200$  nm) revealed three types of characteristic zig-zag shaped domain transitions separating head-on domains, i.e. two domains facing each other with opposite magnetization. First, type (II) and (III) domains exhibit a very characteristic zig-zag pattern along the  $c$ -axis direction. To study the nature of zig-zag domain walls in detail, their occurrence and characteristic as a function of ferromagnetic stripe width and film thickness is investigated. Micromagnetic simulations consistently explain the zig-zag domain walls as a result of the energy minimization of the system. Second, a V-shaped domain configuration was found at the transition between type (II) domains of opposite magnetization that will be explained by micromagnetic simulations as well. Finally, the nucleation of oppositely magnetized domains in thick films proceeds via the formation of zig-zag shaped edge domains.

**Thickness dependence:** Figure 5.6 shows four XMCDPEEM images of (a) 120 nm, (b) 215 nm, (c) 300 nm and (d) 500 nm thick MnAs films [33]. The ferromagnetic stripes can be identified as areas with black and white contrast. As discussed above, the stripe period  $p$  increases with the film thickness. For the analysis of the thickness dependence of the zig-zag pattern, the temperatures were chosen such that the ratio of the widths of the  $\alpha$ - and  $\beta$ -stripes  $w_\alpha/w_\beta$  is constant. Furthermore, only narrower stripes are taken into account where the influence of inter-stripe coupling can be neglected.

The micromagnetic contrast for the 120-nm-thick film [Fig. 5.6(a)] is governed by type (I) and (II) domains, whereas the thicker films show type (III) domains as well. The domain boundaries between type (I) domains of opposite magnetization (running along the  $a$ -axis direction) show a large tilt for thin films and straight walls for thick films [cf. white circles in Figs. 5.6(a) and (b)]. Type (II) domains are characterized by two oppositely magnetized head-on domains separated by a domain transition running along the  $c$ -axis direction. These walls are straight for the 120 nm thick film but they become increasingly structured in thicker films. The 300 and 500 nm thick films exhibit fully developed zig-zag walls [cf. white rectangles in Figs. 5.6(c) and (d)]. Type (III) domains are never observed below a film thickness of ap-

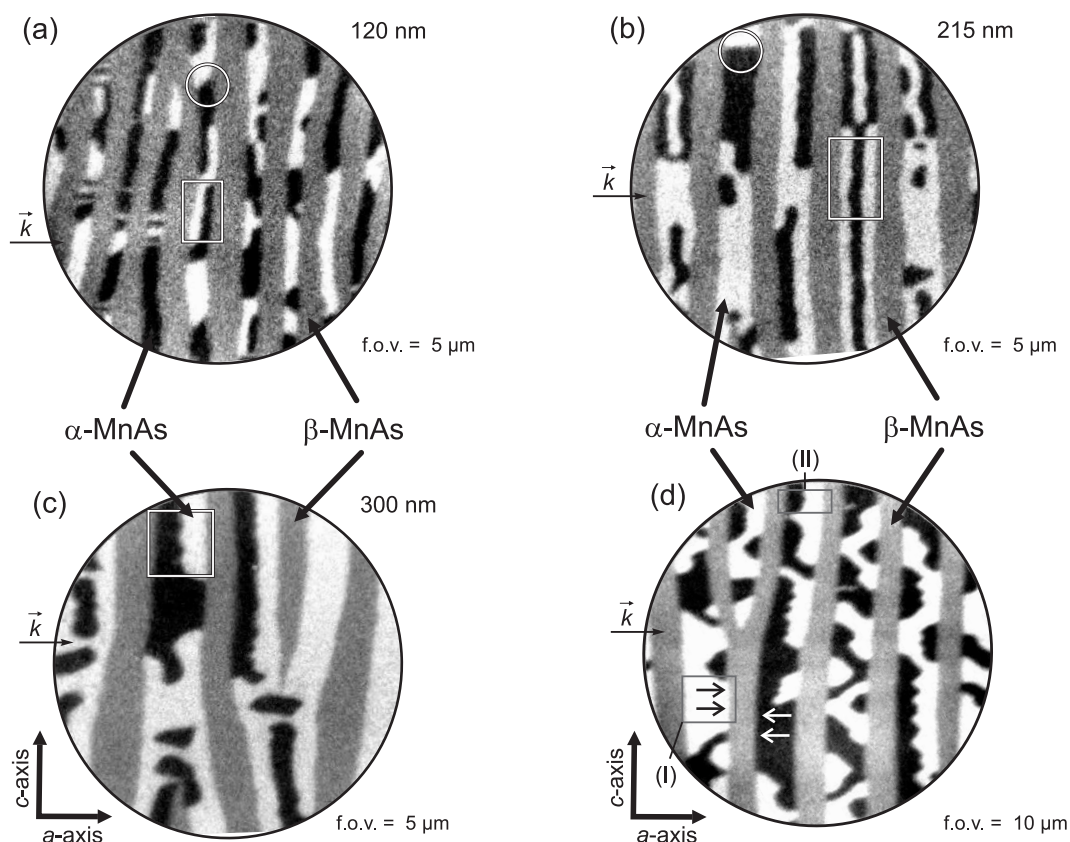


Figure 5.6: Thickness dependence of the micromagnetic domain structure in MnAs films: (a) 120 nm, (b) 215 nm, (c) 300 nm and (d) 500 nm, probed by XMCDPEEM.  $\vec{k}$  indicates the direction of incidence of light.

proximately 150 nm. In the 215-nm-thick film, extended type (III) domains show a zig-zag pattern along both domain boundaries [see rectangle in Fig. 5.6(b)]. This has also been observed in the narrower stripes of the 300-nm-thick film. In contrast, wide ferromagnetic areas are characterized by tilted domain boundaries closer to the edges of the stripe and less extended type (III) domains.

In case of the 500-nm-thick film another type of zig-zag-shaped domain configuration is observed which extends over the whole stripe – in contrast to the zig-zag domain walls. In Fig. 5.6(d) a white circle marks a V-shaped domain configuration. It presents another type of transition between oppositely magnetized type (II) domains, however, associated with an inclined type (III) domain segment. The V-shaped domain configuration was also

found for thinner films.

**Dependence on the stripe width:** To probe the dependence of the domain structure on the ferromagnetic stripe width, temperature-dependent XMCDPEEM measurements on a 500-nm-thick film were performed. As previously mentioned, thicker films exhibit a larger variety of domain structures, and the dynamics of many different structures can be observed simultaneously. Figure 5.7 presents a selection of images obtained during a heating sequence. To ensure a magnetically well-defined state, the sample was cooled through the phase transition to a temperature well below 0°C. In the complete  $\alpha$ -phase, the sample shows no magnetic features on the probed length scale until  $\beta$ -MnAs dots start to form at a temperature of approximately 10°C. At 22°C,  $\beta$ -MnAs reorganizes and forms stripe segments before it finally exhibits a well-ordered stripe structure near 30°C. The formation of regular structures occurs at lower temperatures in thinner films.

With increasing separation of the ferromagnetic stripes in thick films,

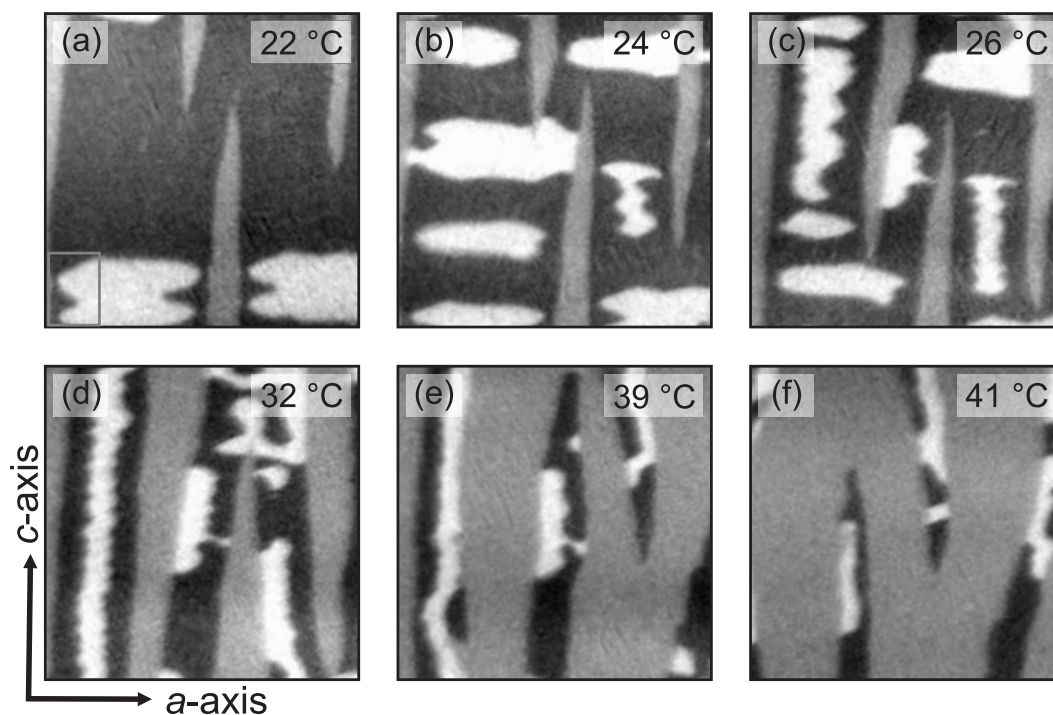


Figure 5.7: Temperature dependence of the micromagnetic domain structure of a 500-nm-thick MnAs-film: (a) 22°C, (b) 24°C, (c) 26°C, (d) 32°C, (e) 39°C, and (f) 41°C. The XMCDPEEM images measure  $5 \times 5 \mu\text{m}^2$ .

they demagnetize by flipping the middle part of a stripe [cf. lower part of Fig. 5.7(a)]. The partial flipping of the stripe leads to a type (III) domain configuration with zig-zag domain boundaries near the edges of the stripe [cf. rectangle in Fig. 5.7(a)]. This third type of zig-zag domain configuration in MnAs represents a typical closure domain configuration in MnAs films.

At around 24°C, the flipped areas separate and then start to extend along the stripe as the stripe narrows between 26 and 32°C [cf. Fig. 5.7(c) and (d)]. The extended type (III) domains show a zig-zag pattern of both domain boundaries, and the walls exhibit a partially correlated arrangement of the zig-zag angles. In the narrower parts of the ferromagnetic stripe network, only type (II) domains are found at 26°C [cf. Fig. 5.7(c)]. This trend continues until at approximately 35°C, at which point type (II) domains are predominant. At higher temperatures close to the phase transition temperature, the remaining stripe segments are primarily in a single domain state.

**Zig-zag domain wall statistics:** After the qualitative description of the influence of the geometrical parameters, namely film thickness and ferromagnetic stripe width, on the micromagnetic domain pattern, a statistical analysis of the zig-zag domain wall angle is obtained from a number of measurements. For this purpose, characteristic parameters of a zig-zag wall are introduced: the periodicity  $P$ , the angle  $2\theta$ , and the amplitude  $2A$ , as illustrated in Fig. 5.8(b).

From the analysis of type (II) zig-zag domains performed on a series of temperature-dependent XMCDPEEM images, the mean values for  $2A$ ,  $P$ , the maximum  $\alpha$ -stripe width up to which type (II) domains are observed  $w_{\alpha}^{max}(\text{II})$ , and the minimum  $\alpha$ -stripe width down to which type (III) domains are still visible  $w_{\alpha}^{min}(\text{III})$ , are listed in Tab. 5.1 for a 300 and a 500-nm-thick film. Type (I) domains exist under all conditions. For the 300 nm film, type

Table 5.1: Mean values for the zig-zag amplitude  $2A$ , the period  $P$ , the ratio  $2A/P$ , the maximum  $\alpha$ -stripe width up to which type (II) domains are observed  $w_{\alpha}^{max}(\text{II})$ , and the minimum  $\alpha$ -stripe width down to which type (III) domains are still visible  $w_{\alpha}^{min}(\text{III})$ .

MnAs thickness [nm]	$2A$ [nm]	$P$ [nm]	$2A/P$	$w_{\alpha}^{max}(\text{II})$ [nm]	$w_{\alpha}^{min}(\text{III})$ [nm]
300	367	517	0.70	555	544
500	464	742	0.63	784	976

(II) domains vanish as soon as type (III) domains nucleate. This does not imply that upon increasing the temperature suddenly only type (II) domains are found. In fact, the dynamic strain balance during the phase transition leads to a distribution of stripe widths  $w_\alpha$  at a given temperature. For the 500 nm film, the remarkable finding is that between a  $\alpha$ -stripe width of between 800 – 1000 nm neither type (II) nor type (III) domains are present. This is partially due to the formation of type (I) domains and due to the fact that only a few segments of the stripes have a width in this range.

From the mean values of amplitude and period, one can calculate the average zig-zag angle using  $\tan \theta = P/4A$ , yielding  $2\theta = 79^\circ$  for the 300-nm-thick film and  $85^\circ$  for the 500-nm-thick film.

As the individual stripe geometry affects the domain structure and thus the zig-zag angle statistics, the zig-zag angle is analyzed as a function of  $\alpha$ -stripe width for the 300-nm-thick film. Again, only type (II) domain boundaries were considered, as the formation of coupled zig-zags in type (III) domains further complicates the analysis [cf. Fig. 5.7(d) on the left-hand side]. As particularly evident in the 500-nm-thick film, the formation

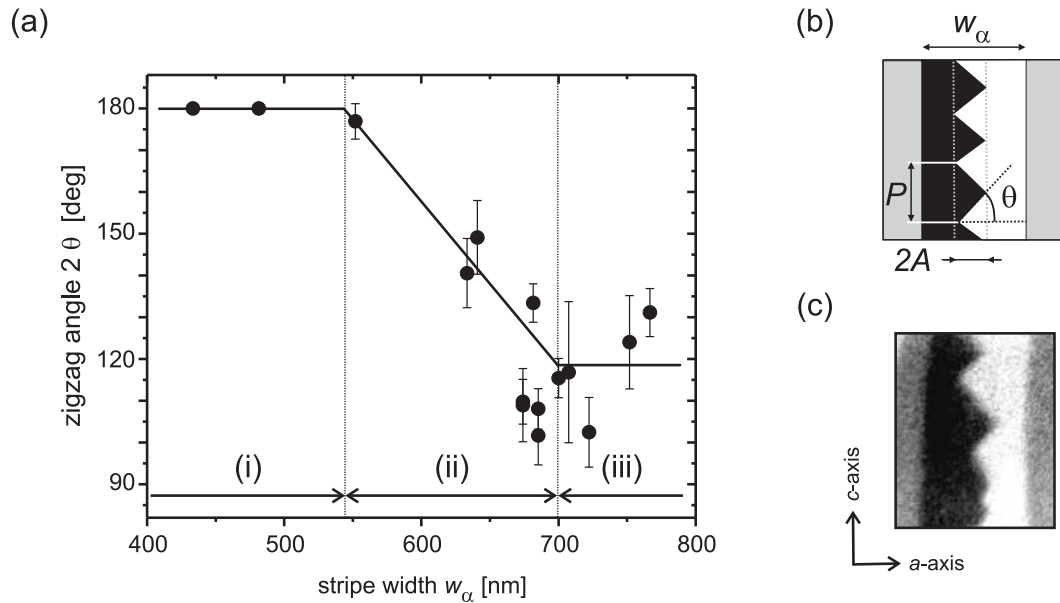


Figure 5.8: (a) Plot of the zig-zag angle  $2\theta$  as a function of  $\alpha$ -stripe width  $w_\alpha$  for a 300-nm-thick MnAs film. Three regimes can be distinguished, as indicated in the graph. (b) Definition of the angle  $\theta$ , the period  $P$ , and the amplitude  $2A$  for a zig-zag wall [in a type (II) domain]. (c) XMCDPEEM image of a zig-zag wall. The analyzed angles are indicated by black lines.

of zig-zag type (III) domains proceeds via the coupling of both zig-zag domain boundaries, partially forming an elongated hexagonal structure.

Figure 5.8(a) plots the zig-zag angle  $2\theta$  as a function of stripe width  $w_\alpha$ . The stripe width was measured locally along with the angle for the complete set of data from 10 – 40°C in steps of  $< 1^\circ\text{C}$ . The data points correspond to the average angles and the error bars to the standard deviation. The plot of the zig-zag angle exhibits three distinct regimes. In regime (i), below a critical stripe width of 540 nm, a constant angle of  $180^\circ$  is found, i.e. a straight domain wall. Straight walls are also characteristic for films thinner than 150 nm (not shown) – independent of  $w_\alpha$ . Contrary to that, the 500-nm-thick film (not shown) exhibits a straight domain wall only for very narrow stripes ( $w_\alpha < 250$  nm).

In the intermediate regime (ii) from 540 to 700 nm the zig-zag angle decreases linearly with increasing stripe width. Regime (iii) is again exhibiting a constant angle, however, being approximately  $115^\circ$  for  $w_\alpha > 700$  nm. For thicker films, the lower limit for  $2\theta$  is  $90^\circ$  and it is observed for  $\alpha$ -stripes wider than 725 nm.

It is now interesting to focus on the stripe width below which the domain boundaries straighten, i.e. when the zig-zag boundaries are no longer energetically advantageous for the system. We find  $w_\alpha = 540$  nm for the 300-nm-thick film and  $w_\alpha = 250$  nm for the 500-nm-thick film, i.e. geometrical ratios of  $w_\alpha/t = 1.8$  and  $0.5$ , respectively. This finding excludes the possibility that the geometrical ratio, and thus the shape anisotropy, is the governing factor for the observed zig-zag wall behavior, because otherwise one should find a critical ratio  $(w_\alpha/t)_{\text{crit}}$  which is universal for the material system.

**The origin of zig-zag domain walls in MnAs:** Zig-zag shaped domain transitions are rarely observed. A prerequisite for the appearance of zig-zag domain walls is a reduction of the total energy by the formation of zig-zag domain walls. On first sight it seems peculiar, since the elongation of a domain wall is at the cost of exchange energy. However, one possible zig-zag configuration is the formation of head-on domains in Gd-Co films. Domain walls between head-on domains are strongly charged, since different normal components of the magnetization on both sides of a domain wall are apparent[144]. Usually charged walls are most likely occurring in samples with low saturation magnetization or very thin films, as charges dramatically increase the magnetostatic energy. For Gd-Co films the nucleation of a zig-zag-shaped wall reduces the charge density per domain length, the shape is a energetic compromise between magnetostatic energy associated with the



charge on the wall and anisotropy energy associated with deviation of the magnetization from the easy axis over a wide region [38]. In other words, the sheer reduction of the charge density per domain length at the cost of exchange and anisotropy energy is taken place. The zig-zag angle is inversely proportional to the film thickness  $t$  with the proportionality constant being determined by the exchange constant and the saturation magnetization. The zig-zag amplitude  $2A$  scales with film thickness as  $t^3$ .

For the system MnAs-on-GaAs, we find apparent head-to-head domains, however the domain transition is not a wall. Moreover, the domain wall angle is not a result of the shape anisotropy, as we should observe the same angle for identical  $\alpha$ -stripe width-to-thickness ratios  $w_\alpha/t$ . Considering the three-dimensional magnetization pattern that is the basis of a type (II) domain – namely the diamond state – the previously discussed model for the formation of zig-zag domains is not appropriate. In the following, the discussion is restricted to single zig-zag domains, i.e. type (II) domains, as zig-zag patterns in type (III) domains couple across the stripe which further complicates the situation. The model of the zig-zag domain wall in type (II) domain structures is shown in Fig. 5.9(a). It is known from other systems, such as iron whiskers, and commonly termed V-line [22]. It will be shown that the zig-zag shape of this boundary is a result of the reduction of demagnetization energy.

For the simulation of the zig-zag domain walls, a ferromagnetic stripe measuring length  $\times$  width  $\times$  thickness =  $1024 \times 384 \times 120 \text{ nm}^3$  with a cell size of 8 nm was considered. The dimensions and the cell size are a compromise between computation time and precision. As a starting configuration, a diamond state extending along the stripe was assumed. Upon relaxation of the initial magnetization configuration, the straight domain boundary separating the oppositely magnetized stripe areas exhibits a zig-zag shape. The results of the simulation are shown in Fig. 5.9(b). On the left, the in-plane component of the magnetization  $m_y$ , and on the right, the out-of-plane component  $m_z$  is depicted at the surface of the structure (top), in the middle, and at the interface with the substrate (bottom). The in-plane component at the surface – that corresponds to the contrast observed in XMCDPEEM – exhibits a zig-zag shape. The modulation becomes even clearer in the image of the out-of-plane component of the magnetization on the right. The amplitude of the modulation further increase towards the middle plane and finally decreases again towards the interface (bottom layer). The energy of the initial magnetization distribution was  $3.231 \cdot 10^4 \text{ J/m}^3$ , which reduces to  $3.139 \cdot 10^4 \text{ J/m}^3$  for the relaxed zig-zag structure. The formation of the zig-zag pattern is at the cost of exchange energy ( $1.665 \cdot 10^4 \text{ J/m}^3 \rightarrow 1.741 \cdot 10^4 \text{ J/m}^3$ ), while the demagnetization energy is reduced ( $1.561 \cdot 10^4 \text{ J/m}^3 \rightarrow 1.397 \cdot 10^4 \text{ J/m}^3$ ). The change in anisotropy energy is more than a magnitude smaller and can

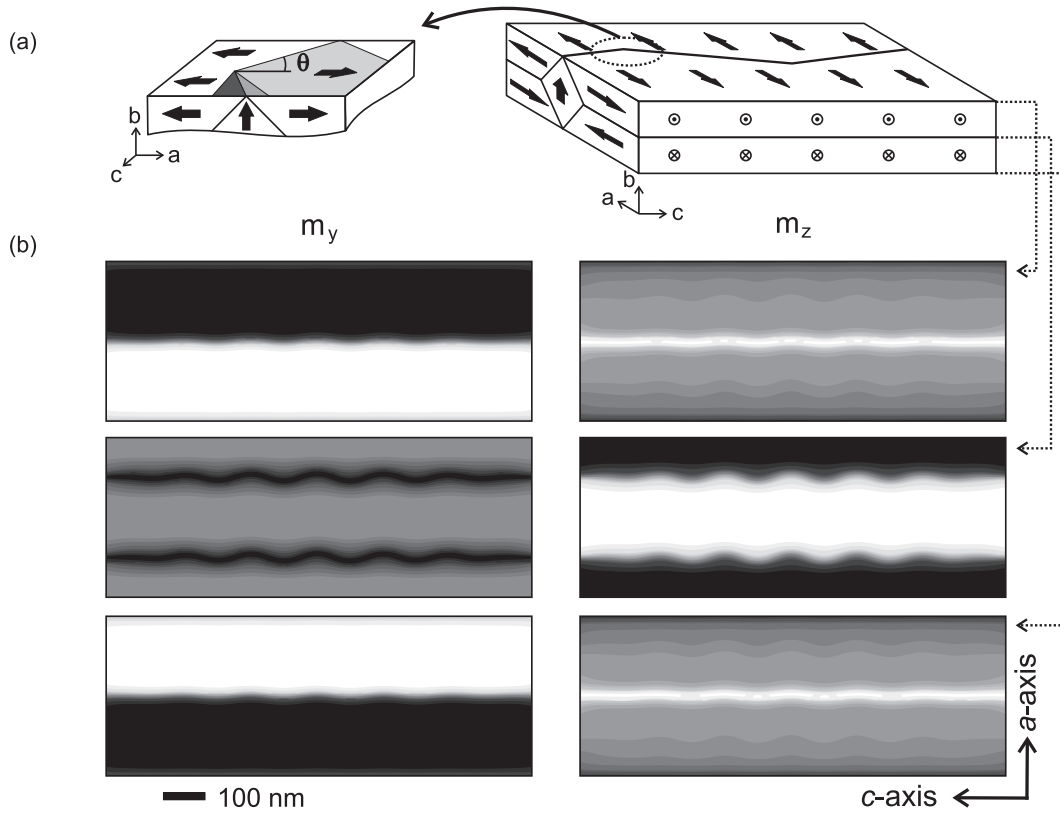


Figure 5.9: (a) Model of a zig-zag domain wall in MnAs films. The underlying domain structure shows a diamond state. The rotated close-up illustrates the zig-zag angle and tilt of the diamond state. (b) Simulated magnetization distribution [top view of the surface (top), the middle and the interface layer (below)] indicating the micromagnetic nature of the zig-zag domain wall in MnAs. On the left, the in-plane component of the magnetization ( $m_y$ ) and on the right, the out-of-plane component ( $m_z$ ) is shown.

thus be neglected. Thus, it can be concluded that the driving mechanism of the zig-zag formation in MnAs is the minimization of the stray field of a diamond state.

Within this context, the dependence of the zig-zag angle on the stripe width can be understood. In case of wide stripes [cf. Fig. 5.8(a), regime (iii)], a constant angle of  $115^\circ$  is found. This angle corresponds to the minimum energy of type (II) domains for the given film thickness. In regime (ii), the zig-zag angle is a linear function of the stripe width. As the fully developed diamond domain requires a certain space in the  $a$ -axis direction, the stripe

dimensions restrict the movement of the diamond domain. Consequently, the amplitude of the zig-zag is reduced and thus the angle increased. The required space for a symmetric diamond domain is on the order of the film thickness. Finally, if the stripe width is below twice the film thickness, the space is becoming too small for the diamond domain to establish a zig-zag pattern.

**Explanation of the V-shaped domain configuration:** The second type of domain configuration exhibiting a zig-zag shape is the V-shaped structure. It extends across the whole stripe width and is commonly observed for thick films [cf. white circle in Fig. 5.6(d)]. It represents a transition between type (II) domains via a skewed type (III) domain resembling a V-shape. For the micromagnetic simulation, a sample measuring length  $\times$  width  $\times$  thickness =  $1024 \times 340 \times 120 \text{ nm}^3$  with a cell size of 8 nm and an initial completely random magnetization was used. Figure 5.10 presents a detailed look on one half of a simulated V-shaped structure. On top, an image of the in-plane magnetization component  $m_y$  of the uppermost layer is shown, corresponding to the observed XMCDPEEM contrast. Below, cross-sections of the out-of-plane magnetization component  $m_z$  at the respective positions indicated in the image above are depicted.

Starting on the left, a type (II) with a stretched diamond domain is observed. In contrast to the case described above, where the position of the diamond domain oscillates with a zig-zag shape along the stripe, the diamond domain overstretches [cross-section (2)] and is ripped apart (3). An antiparallel diamond domain nucleates (4) in the middle of the stripe that drives out the edge domains (5). The transitional type (III) domain can be found in the 4<sup>th</sup> cross-section. The stretched edge domains (dark) start to retract (6) until the inverse of the initial type (II) domain configuration is reached again (7). In cross-section (8), the reverse process starts again.

Comparing the results for the zig-zag domain wall and the V-shaped domain configuration, it is found that in both cases the governing underlying domain pattern is a stretched diamond domain. The difference lies in the correlation of the upper and lower tip of the diamond. Whereas the zig-zag domain is due to an oscillatory in-phase movement of both tips, the V-shaped transition is characterized by an out-of-phase stretching. In other words, the position of the zig-zag pattern on the top and bottom layer of the film is identical for the zig-zag domain and mirrored for the V-shaped domain.

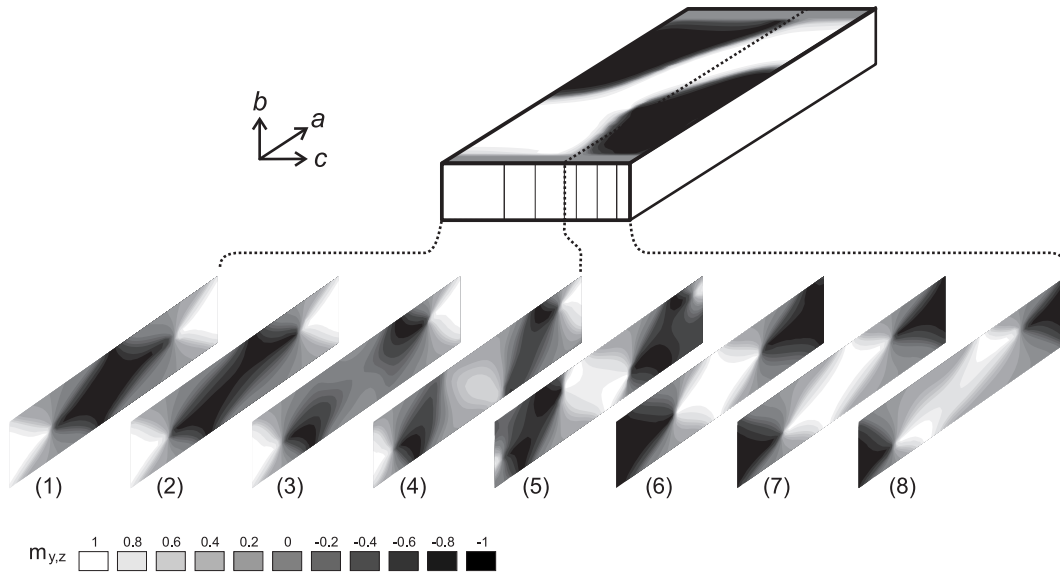


Figure 5.10: Micromagnetic simulation of the V-shaped domain transition. For clarity, the out-of-plane component  $m_z$  is depicted. Top: image of the in-plane component ( $m_y$ ) of the magnetization of the uppermost layer; bottom: corresponding cross-sectional cuts of the out-of-plane components of the magnetization in the hexagonal plane. Their positions along the stripe are indicated in the image above.

## 5.4 Inter-stripe coupling

Besides the micromagnetic properties of individual ferromagnetic stripes, the ensemble of the self-organized ferromagnetic structure can lead to effects in the magnetic properties of the system. So far, the intra-stripe structure along has been discussed in detail. Now, the interaction between the stripes is investigated. The study has been performed relying on MFM and XMCDPEEM data which reveal consistent results. I will restrict the discussion to XMCDPEEM experiments, as a straight-forward quantitative analysis is possible. Films of four different thicknesses, 120, 180, 300, and 500 nm were investigated. Before every measurement, after the removal of the As cap layer, the samples were cooled down well below  $0^\circ\text{C}$  rendering the films are in the pure  $\alpha$ -phase.

Figure 5.11 shows a sequence of XMCDPEEM images recorded at increasing temperatures in the same area of a 120-nm-thick film. In the complete  $\alpha$ -phase ( $0^\circ\text{C}$ ), the film exhibits very large single domain areas (compared to the f.o.v. of  $5\ \mu\text{m}$ ). Upon heating to the nucleation of the  $\beta$ -phase at  $10^\circ\text{C}$ ,

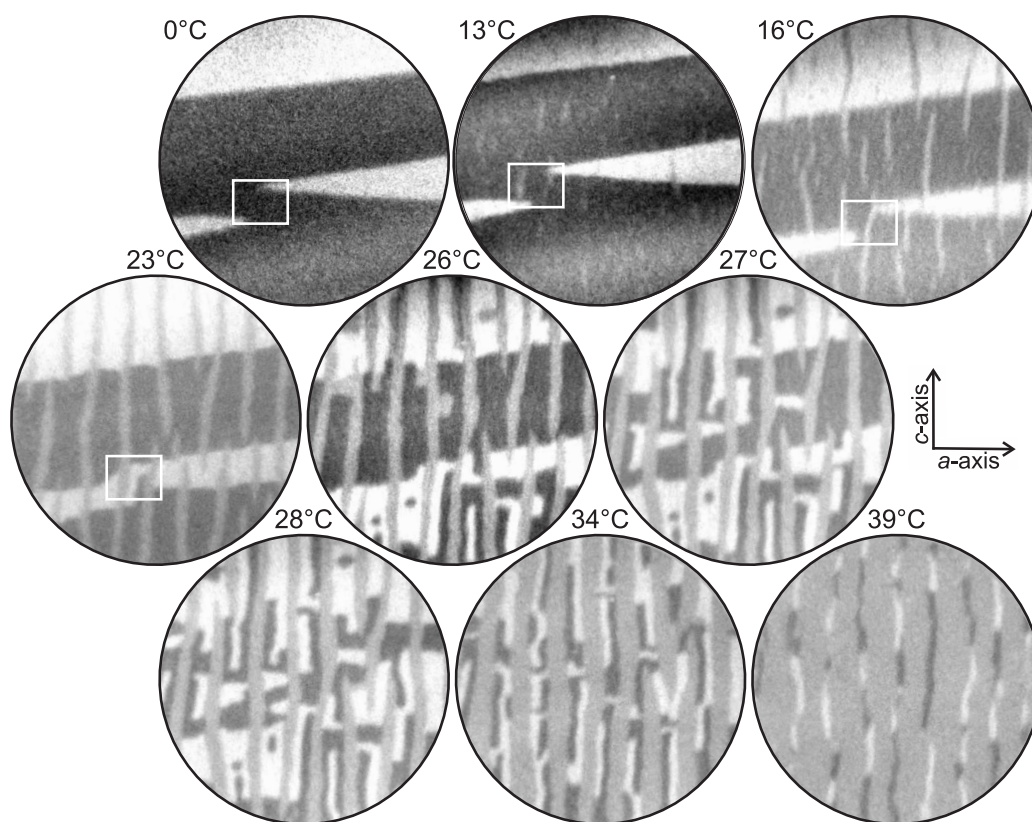


Figure 5.11: Influence of inter-stripe coupling on domain patterns of a 120-nm-thick MnAs film on GaAs(001) imaged by XMCDPEEM (f.o.v. diameter: 5  $\mu\text{m}$ ).

no change in magnetization is observed. At 13°C, the  $\beta$ -phase material (gray contrast) is largely unordered and its presence has no apparent influence on the micromagnetic domain structure. At 16°C, the  $\beta$ -phase material tends to form a regular stripe array, and slight changes in the domain structure become apparent. At 23°C, the  $\beta$ -phase is fully ordered and the common, regular  $\alpha$ - $\beta$ -stripe structure is present. At this temperature, domain flipping may occur due to the separation of the extended ferromagnetic domains into smaller compartments by the introduction of the  $\beta$ -stripes. As indicated in Fig. 5.11 by a rectangle, two tails of the domain with bright contrast have almost formed one extended domain in pure  $\alpha$ -phase. However, the development of an extended domain does not occur until  $\beta$ -stripes are incorporated, which separate the antiparallel domains and reduces the size of the compartment sandwiched between two bright domains at neighboring stripes. Then

the antiparallel domain flips, indicating a magnetostatic biasing effect of the neighboring stripes and thus inter-stripe coupling.

It has to be noted that the commonly observed domain walls in the pure  $\alpha$ -phase are inclined with respect to the easy axis. Inclined domain walls exhibit an additional stray field contribution to the total energy, compared to straight domain walls, and become unstable as soon as the large domains get separated by the introduction of  $\beta$ -MnAs. The domains extending across the stripes favor domain walls running along the  $a$ -axis direction as this eliminates the contribution of the stray field. The inter-stripe regime is therefore characterized by extended domains across the stripes, the formation and the flipping of compartments.

The micromagnetic structure undergoes a dramatic change at 26 °C. Within the extended domains, areas of opposite magnetization nucleate. Now, the demagnetization of the individual stripes is favored at larger stripe separations and closure domain intra-stripe structures are preferred. If only type (I) domains are present, the demagnetization results in a sequence of oppositely magnetized domains [cf. Fig. 5.11]. In the present case, however, higher order domains are also observed that are not extended across the stripes but still show an intra-stripe structure. Above 28°C, all type (I) domains transform into type (II) domains until the stripes become so narrow that they transform back to single domain again. Close to the phase transition at 40°C, the  $\alpha$ -stripes finally decompose into isolated ferromagnetic dots.

From the discussion of the decoupling behavior of the 120-nm-thick film, two main results can be deduced: the inter-stripe coupling, i.e. correlated domains over several  $\alpha$ -stripes, governs the micromagnetic properties of the stripe structure up to the temperature of 26°C. Once the inter-stripe coupling breaks down due to an increasing distance between the ferromagnetic stripes, intra-stripe structures with small demagnetization fields nucleate. The formation of relatively dense antiparallel domains or type (II) domains leads to a reduction of the stray field energy at the cost of exchange energy.

The samples investigated with XMCDPEEM are nominally demagnetized. This is usually reached by cooling them down from the  $\gamma$ -phase (typically from above 300°C) in zero applied field. However, as the field-of-view is on the micron-scale, an effective net magnetization is observed, i.e. only by averaging over larger film areas the film proves to be not magnetized. By analyzing the net magnetization and domain wall boundary length as a function of temperature (or, similarly, stripe separation), a quantitative insight into the decoupling of the stripes can be achieved. Plots of the relative areas of a ferromagnetic stripe occupied by the parallelly and antiparallely magnetized domains and the respective domain wall lengths between the parallelly

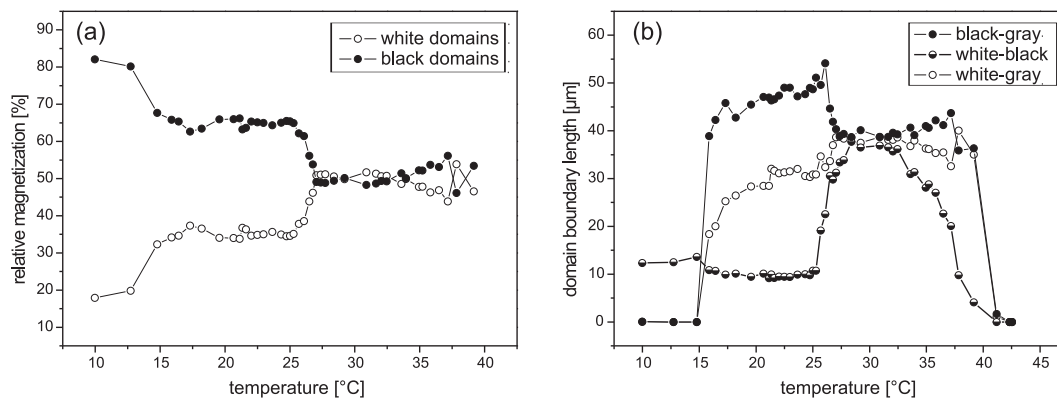


Figure 5.12: Quantitative analysis of the inter-stripe coupling behavior of a 120-nm-thick MnAs film. (a) Plot of the parallel and antiparallel magnetized fraction of the ferromagnetic areas. The curves correspond to the relative area of black and white contrast of the XMCDPEEM images, shown in Fig. 5.11. (b) Boundary length of regions with white and gray, white and black, and black and gray contrast, respectively.

(white) and antiparallely (black) magnetized domains and the nonmagnetic areas (gray contrast) are shown in Fig. 5.12 for a 120-nm-thick film.

Two regimes can be clearly distinguished in the plots of the relative magnetization [Fig. 5.12(a)]. Large relative magnetization values are found at low temperatures. A plateau with moderate smaller net magnetization is reached between 16 and 23°C. In this plateau regime, the extended domains are more ordered across the stripes by domain flipping and domain wall movement as a result of inter-stripe coupling. Between 26 and 27°C, the net magnetization vanishes as type (II) domains that show no net magnetization are introduced, replacing type (I) domains. The balancing of the different magnetization direction indicates the effective demagnetization of individual ferromagnetic stripes. This occurs most likely due to the nucleation of flux-closure domains, whereby the inter-stripe coupling is lost. Accompanied by the sudden drop of the ratio of parallel and antiparallel domains, a large increase in the domain boundary length between oppositely magnetized domains is found [cf. Fig. 5.12(b)].

The two coupling regimes are an universal property of the stripe array and, to a certain degree, independent of film thickness. Figure 5.13 shows the plots of the net magnetization and domain wall length for three additional film thicknesses: 180, 300, and 500 nm. For the thinner films, a f.o.v. window of 5  $\mu\text{m}$  was analyzed and for the 500-nm-thick film a window of 10  $\mu\text{m}$ .

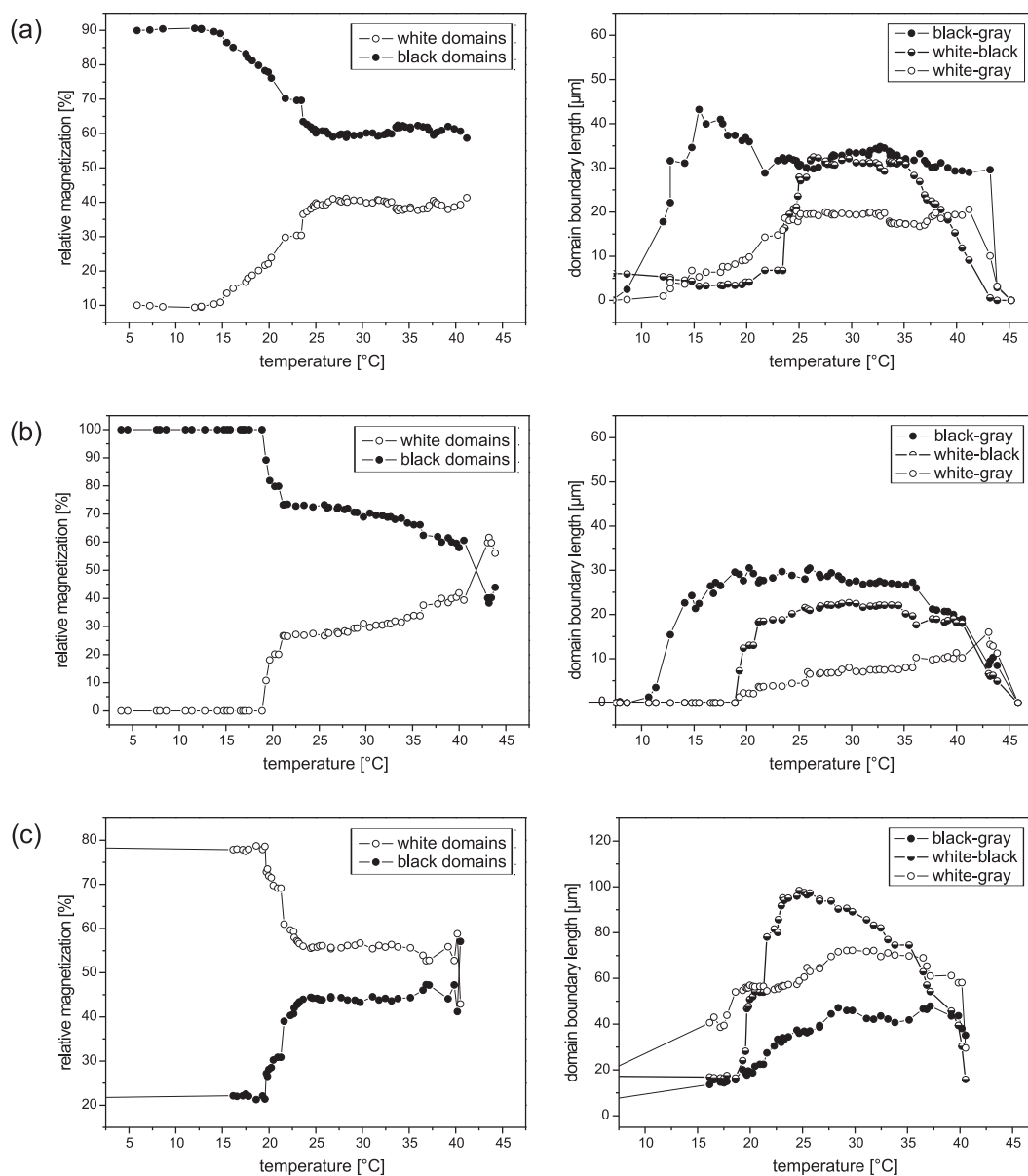


Figure 5.13: Quantitative analysis of the inter-stripe coupling behavior of (a) a 180-nm-thick MnAs film, (b) a 300-nm-thick MnAs film and (c) a 500-nm-thick film. For all film thicknesses, the relative amount of parallel and antiparallel magnetized domains (left-hand side) and the corresponding boundary lengths (right-hand side) are shown.



The ratio of the oppositely magnetized areas is different for the starting configurations. For the 180-nm-thick sample a gradual decrease of the net magnetization is observed due to a sample drift during the heating cycle. No complete demagnetization is reached up to the maximum temperature that was analyzed. In case of the 300-nm-thick film (b), the observed area is completely magnetized in one direction and the decrease of the polarization starts at  $\sim 20^\circ\text{C}$ . Above that temperature, the relative magnetization decays very slowly in case of the 300-nm-thick film and stays roughly the same in case of the 500-nm-thick film. Again, no complete microscopic demagnetization was observed up to the phase transition temperature. In fact, the net magnetization after the breakdown of the inter-stripe coupling depends on the magnetization ratio at the beginning of the heating cycle and on the film thickness. This effect can be attributed to the limited field-of-view and to the formation of three-dimensional magnetization patterns in thicker films. As mentioned above, XMCDPEEM is only sensitive to the topmost layer.

All films show a steep increase in the length of the domain wall separating areas of black and white contrast at the temperature coinciding with the formation of a plateau with reduced net magnetization. This onset temperature shifts to lower values for thicker films. In general, the length of the domain wall between areas of black and white contrast is a measure of the gain of the total energy by the formation of flux-closure domains. Upon further heating, the domain wall length goes to zero as the break-up of the continuous  $\alpha$ -stripes close to the phase transition temperature renders the stripe segments in a single domain state. Furthermore, it should be noted that the plotted domain boundary lengths are absolute values and not corrected for the amount of ferromagnetic material. In case of the 500-nm-thick film that is known to exhibit complex three-dimensional domains, a second step increase of the domain wall length to a value of  $100\ \mu\text{m}$  is observed above  $22^\circ\text{C}$ . As in case of the thinner films, at higher temperature and thus narrower  $\alpha$ -stripes, the domain wall length decreases again as the single domain state is energetically preferred. It has to be noted that the tendency of thick films to form type (III) domains limits the information value of the net magnetization at the surface concerning the demagnetization of individual stripes. Thus, it cannot be concluded from the remaining net magnetization in case of the thicker films that the domains are not able to decouple completely.

The tendency to form enclosed domains, i.e. areas of opposite magnetization within a larger domain, can be obtained from looking at the length of the domain boundaries between ferromagnetic areas of the respective magnetization and the nonmagnetic areas. The 120-nm-thick film exhibits an equal domain boundary length for both magnetization directions with  $\beta$ -

MnAs upon complete demagnetization [cf. Fig. 5.12 (b)]. On the contrary, the thicker films (180 and 300 nm) show a preference of one magnetization direction over the other in the plateau region [cf. Fig. 5.13(a) and (b)]. However, as the domain wall length between the ferromagnetic domains increases, enclosed domains form that reduce the stray field energy by their domain structure in-depth and not by the sole compensation of the surface magnetization.

To obtain a deeper insight into the inter-stripe coupling due to magnetic interaction, two-dimensional micromagnetic simulations were performed. From the experiments, it can be concluded that the relevant magnetic features are domains that extend across ferromagnetic stripes (in the  $a$ -axis direction). Thus, in order to describe the coupling, the initial magnetic intra-stripe structure is not of primary importance. Since MnAs films exhibit an easy plane of magnetization perpendicular to the  $c$ -axis that plays an increasing role with decreasing contribution of the shape anisotropy for thicker films, a three-dimensional micromagnetic simulation code should, in principle, be employed. However, as three-dimensional simulations of a large array of coupling ferromagnetic stripes are very time-consuming and as closure domain-like structures do not result in a significant stray field (the magnetic interaction between stripes is strong for domains that exhibit a large stray field), less computing-intensive two-dimensional simulations are presented.

The  $\alpha$ - $\beta$ -phase coexistence is modeled by placing nonmagnetic material between three ferromagnetic stripes. The sample is  $1280 \times 1280 \text{ nm}^2$  ( $128 \times 128$  grid points) and the ferromagnetic stripe width is varied from 420 nm down to 10 nm. The following parameters for MnAs were used in the two-dimensional simulation: exchange stiffness constant  $A = 1.0 \cdot 10^{-11} \text{ J/m}$ , saturation magnetization  $M_s = 8 \cdot 10^5 \text{ A/m}$ , and magnetocrystalline anisotropy constants  $K_{u_1} = -7.2 \cdot 10^5 \text{ J/m}^3$  and  $K_{u_2} = 3.6 \cdot 10^5 \text{ J/m}^3$ . The  $y$ -axis of the coordinate system of the simulator corresponds to the magnetocrystalline hard axis ( $c$ -axis). The goal of the simulations is not to reproduce the micromagnetic fine structure, but to get an insight into the coupling between the stripes. Therefore, the commonly observed type (II) and (III) domains will not appear in the simulated magnetization distributions as they are in fact three-dimensional magnetization patterns.

As an initial configuration, the ferromagnetic  $\alpha$ -stripes of a chosen separation  $w_\beta$  were assumed to be randomly magnetized. The random magnetization was allowed to relax at zero applied field. The results as a function of stripe separation are shown in Fig. 5.14. At a separation of  $w_\beta = 10 \text{ nm}$  ( $\hat{=} 11^\circ\text{C}$ ), domains typically extend over several stripes (in the  $a$ -axis direction) and few domain walls are present, in accordance with the experimental observations. Furthermore, the domains which are not coupled across all

three stripes show slightly tilted domain walls (with respect to the  $a$ -axis). As the width of the ferromagnetic stripes is decreased, the magnetization of some areas of the stripes flips. This results in domains that extend over all three stripes, which is a fingerprint of the inter-stripe coupling. The flipping of the domains occurs predominantly for domains with previously tilted domain walls. Upon further decreasing the ferromagnetic stripe width (increasing the width of the nonmagnetic spacer), the spatial ordering of the domain structures vanishes as the magnetic coupling between the stripes becomes too weak. The ferromagnetic stripes then try to minimize their stray fields individually, resulting in an increased number of domain walls. Upon complete decoupling of the stripes, the domain width (in the  $c$ -axis direction) becomes the same for all stripes. At a separation of  $w_\beta = 610$  nm, the simulations show that the narrow stripes exhibit a predominant out-of-plane magnetization as the stripes are now narrower (20 nm) than they are thick (50 nm). The respective plot of the relative magnetization is shown

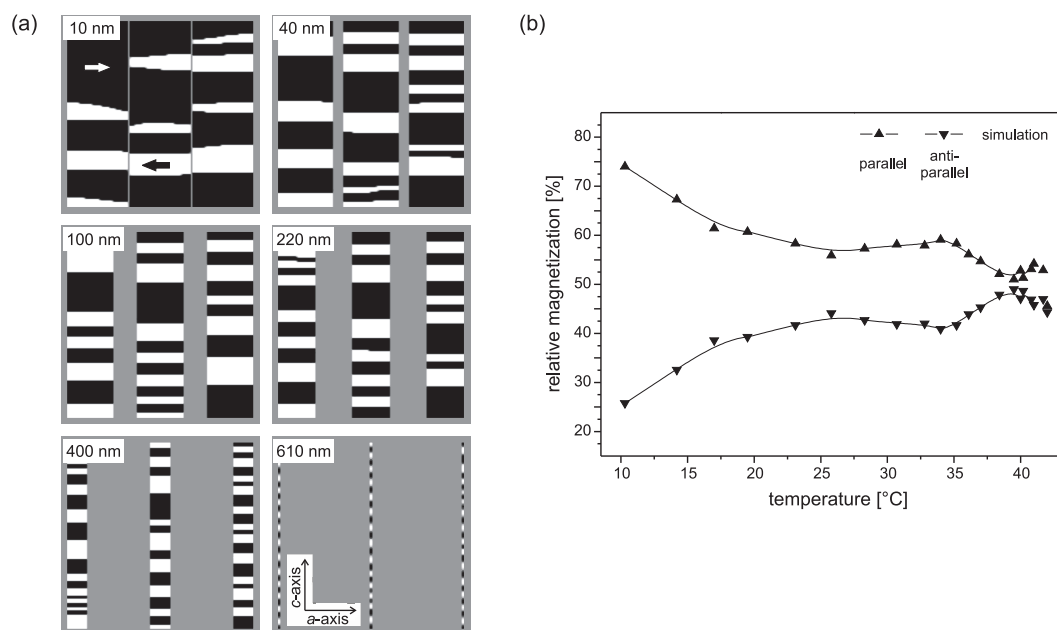


Figure 5.14: (a) Micromagnetic simulation of the domain structure of coupled ferromagnetic stripes. The stripe separation  $w_\beta$  is indicated above the images. White and black contrast: parallel and antiparallel magnetization, respectively; gray: nonmagnetic areas. (b) Plot of the parallel and antiparallel magnetized fraction of the ferromagnetic areas of the simulated structure as a function of temperature.

in Fig. 5.14(b). As in the experimental data, clearly two regimes can be distinguished. In contrast to the experiments on the 120-nm-thick film, the first decay of the net magnetization happens more gradually and is connected with the formation of extended domains across the stripes. The second decay of the net magnetization is due to the formation of compartments as the stripes are completely decoupled. Since two-dimensional simulations are not able to yield type (II) domains, the simulated demagnetization is solely due to the reduction in magnetic dipole interaction.

The inter-stripe interaction and the coupling behavior may also have an impact on the magnetization reversal. As long as the films are thinner than the critical film thickness for the nucleation of in-depth domains, the inter-stripe coupling can have a magnetostatic biasing effect. To reverse the magnetization, the applied magnetic field has to overcome the coercive field and the biasing field of neighboring stripes.

## 5.5 Micromagnetics of MnAs-on-GaAs(111)B

For MnAs films on GaAs(001), the magnetization distribution in the basal plane is experimentally not accessible by imaging techniques. However, a cross-sectional view of the ferromagnetic stripes would complete the investigation of the micromagnetic structure of MnAs-on-GaAs(001). Unfortunately, cleaved samples have elastic and thus micromagnetic properties that differ from the regular  $\alpha$ - $\beta$ -stripe structure. In order to gain insight into the domain structure of the basal plane at remanence, XMCDPEEM measurements have been performed on MnAs films on GaAs(111)B [21]. It was found that MnAs on GaAs(111)B exhibits a self-organized structure on the nanoscale [136]. However up to now, no correlation between the topographic structure and the magnetic properties have been found [85]. Here, the discussion is mainly focussed on the type of domains in the basal (0001) plane of MnAs.

Figure 5.15 shows an XMCDPEEM image of MnAs/GaAs(111)B at remanence, after a decapping procedure to completely remove the As protection layer and cooling down to 19°C. The plane of incidence of the light was slightly misaligned to the MnAs $[\bar{2}110]$  axis. The magnetic contrast reaches from dark to bright, corresponding to the magnetization ranging from fully parallel to fully antiparallel, respectively. Neutral gray contrast is obtained for nonmagnetic areas, as well as for a vanishing projection of the magnetization vector along the selected MnAs $[\bar{2}110]$  axis ( $\vec{M} \perp \vec{k}$ ). The micromagnetic

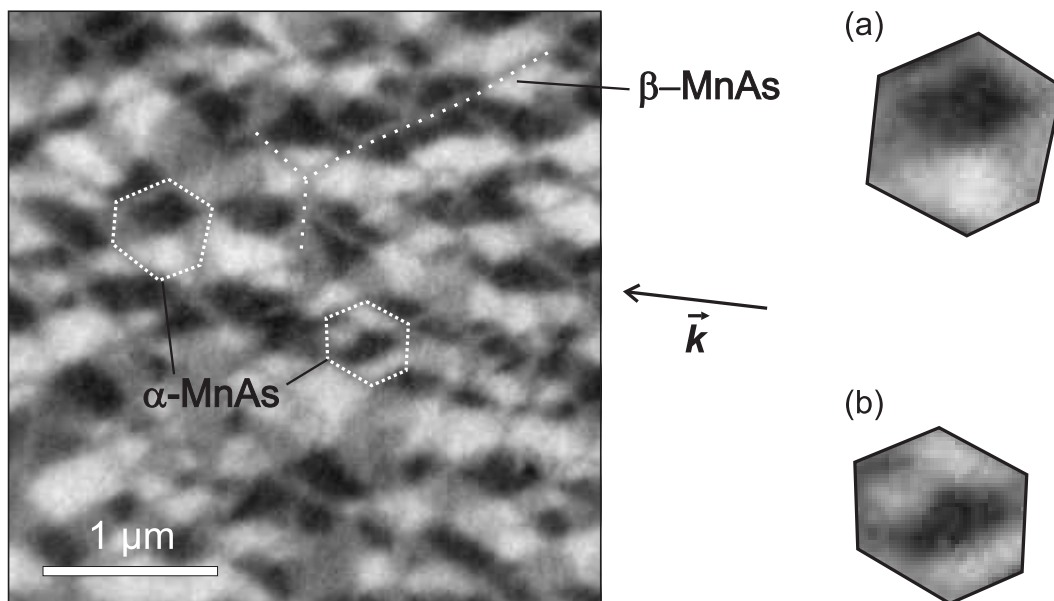


Figure 5.15: Micromagnetic XMCDPEEM image of a 270-nm-thick MnAs film on GaAs(111)B recorded at 19°C. The wave vector  $\vec{k}$  of the incident light is indicated on the right-hand side. Ferromagnetic  $\alpha$ -MnAs arranges in a network of quasi-hexagonal structures, separated by nonmagnetic  $\beta$ -MnAs. Two close-ups of quasi-hexagonal elements reveal the common magnetization patterns: (a) vortex-like domain and (b) distorted stripe domain.

domain pattern obtained by XMCDPEEM imaging [cf. Fig. 5.15] shows a number of discrete contrast levels in the ferromagnetic areas, reflecting the projection of the magnetization  $\vec{M}$  onto  $\vec{k}$ . The coexisting nonmagnetic  $\beta$ -MnAs areas exhibit a neutral gray contrast and form a honeycomb-like network that is indicated by a dotted line. The exact position of the  $\beta$ -MnAs can be obtained from LEEM imaging [10, 11] at the sample spot. Two representative quasi-hexagonal  $\alpha$ -MnAs areas are highlighted and zoomed into in Fig. 5.15(a) and (b). The first structure shown in (a) exhibits three contrast levels, where the dark and bright contrast areas occupy each two of the hexagonal segments, while a similar, neutral gray level is seen in the remaining two segments. This contrast belongs to a vortex-like state, as will be shown later. The second domain pattern depicted in Fig. 5.15(b) shows basically three areas with largely opposite magnetization and it further exhibits a fine structure.

In principle, the magnetic easy plane character of the MnAs(0001) face leads to a number of domain configurations, as no direction is preferred. This can be held responsible for the difficulties in interpreting the MFM

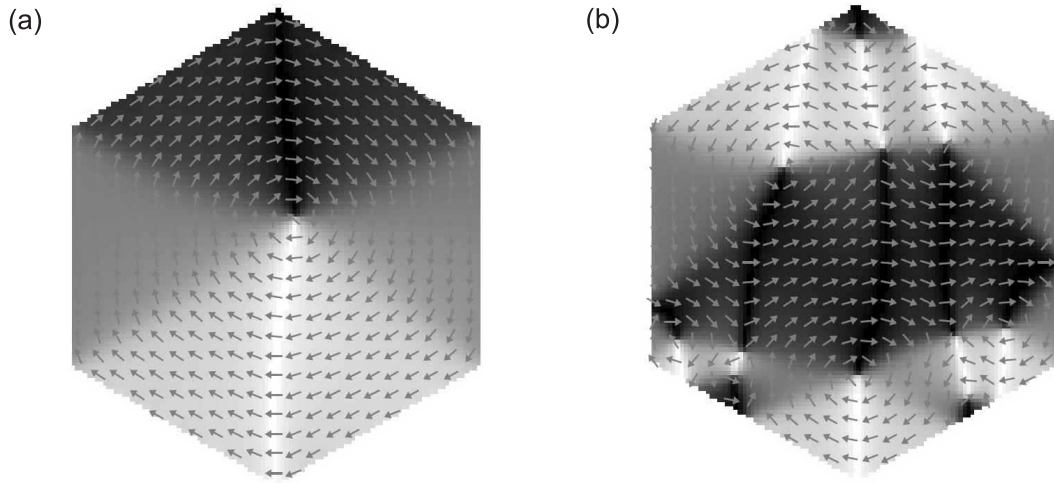


Figure 5.16: Calculated magnetization vector field in the remanent state of two representative domain patterns. (a) Vortex-like domain pattern and (b) (distorted) stripe domain pattern.

observations [85]. To understand the micromagnetic contrast of MnAs-on-GaAs(111)B, two-dimensional micromagnetic simulations are performed [32]. An array of hexagonal, ferromagnetic  $\alpha$ -MnAs columns with a side length of 300 nm, separated by 50 nm wide nonmagnetic material is assumed. Thus, the lateral size of the simulated structure is the same as the average size of the observed quasi-hexagonal structures. The simulated hexagonal pattern measures  $1585 \times 1640 \text{ nm}^2$ . The two-dimensional unit cell of the simulation is chosen to be  $(5 \text{ nm})^2$  which has the same dimensions as the magnetocrystalline and the magnetostatic exchange lengths in MnAs. Reasonable parameters are used for the two-dimensional simulations: exchange stiffness constant  $A = 1.0 \cdot 10^{-11} \text{ J/m}$ , saturation magnetization  $M_s = 8 \cdot 10^5 \text{ A/m}$  (from magnetization curve measurements), and an uniaxial magnetocrystalline anisotropy with the constants  $K_{u_1} = -7.2 \cdot 10^5 \text{ J/m}^3$  and  $K_{u_2} = -3.6 \cdot 10^5 \text{ J/m}^3$ . The axis of the magnetocrystalline anisotropy ( $c$ -axis) is collinear with the  $z$ -axis of the coordinate system. The thickness of the simulated film was set to 50 nm, as a strong thickness-dependence of the magnetization distribution is not expected.

As an initial configuration, the ferromagnetic hexagons were assumed to be randomly magnetized. The simulation of the hexagonal structure in Cartesian coordinates leads to structural boundaries that are approximated by a staircase along the grid lines. The approximated magnetic boundary conditions introduce deviations of exchange and stray field contributions to

the effective field, which can cause discrepancies in the switching mechanism and the formation of vortices near the staircase-approximated boundary [41]. Nevertheless, the remanent magnetic configuration shows that the magnetization vector is parallel to the boundary of the hexagon. Thus, the staircase approximation seems appropriate for the present magnetic problem.

For the simulation, a random magnetization was allowed to relax in zero applied field and the result is shown in Fig. 5.16 for the most two common states – the vortex-like state (a) and the (distorted) stripe state (b). In the vortex-like state, the magnetization is largely parallel to the respective hexagonal boundary, leading to a domain pattern with a six-fold symmetry. This is in correspondence with the magnetization of the ferromagnetic hexagon in Fig. 5.15(a). The arrows represent the direction of the local magnetization  $\mathbf{M}(\mathbf{r})$ . In the stripe state, basically three predominant magnetization directions can be seen, leading to the observed contrast. A closer look at the domain structure reveals a number of neighboring vortex-like states in the vicinity of the staircase boundary, which is a consequence of the staircase approximation.

The stripe state is also governed by coupling across the  $\beta$ -MnAs spacers. Because the magnetocrystalline anisotropy, as well as the shape anisotropy, impede an out-of-plane magnetization, the demagnetization and exchange energies govern the formation of domains. They exhibit the tendency to form flux-closure domains. Thus, MnAs(0001) on GaAs(111)B behaves in this respect like a soft magnetic material.

# Chapter 6

## Field dependence of micromagnetic domain pattern

Magnetization reversal is a key property of magnetic materials and of importance for technological applications. The shape of the hysteresis loop exhibits signatures of different reversal processes. With complementary MFM experiments the domain formation is investigated on a microscopic scale. The combination of both techniques allows for a correlation of both the domain structure and the hysteresis.

In this Chapter, the field dependence of micromagnetic domain pattern is studied. In the first Section, the evolution of the magnetization distribution is investigated starting from a demagnetized state in an applied field by combined SQUID and MFM measurements. Supporting micromagnetic simulations provide an explanation of the field-dependent stability of the domain structure. In the second Section, a detailed analysis of the magnetization reversal characteristics of MnAs films is provided. In the  $\alpha$ - $\beta$ -phase coexistence regime, two distinctively different reversal characteristics are apparent. They are found to be a function of temperature and film thickness. On the basis of micromagnetic simulations, the experimental findings are explained in a consistent way.

### 6.1 The virgin curve

The influence of an external magnetic field on the domain structure of MnAs films on GaAs(001) is studied. A nominally 180-nm-thick MnAs film<sup>1</sup> was investigated at room temperature with the variable-temperature and field

---

<sup>1</sup>Film thickness determined by SEM: 140 nm



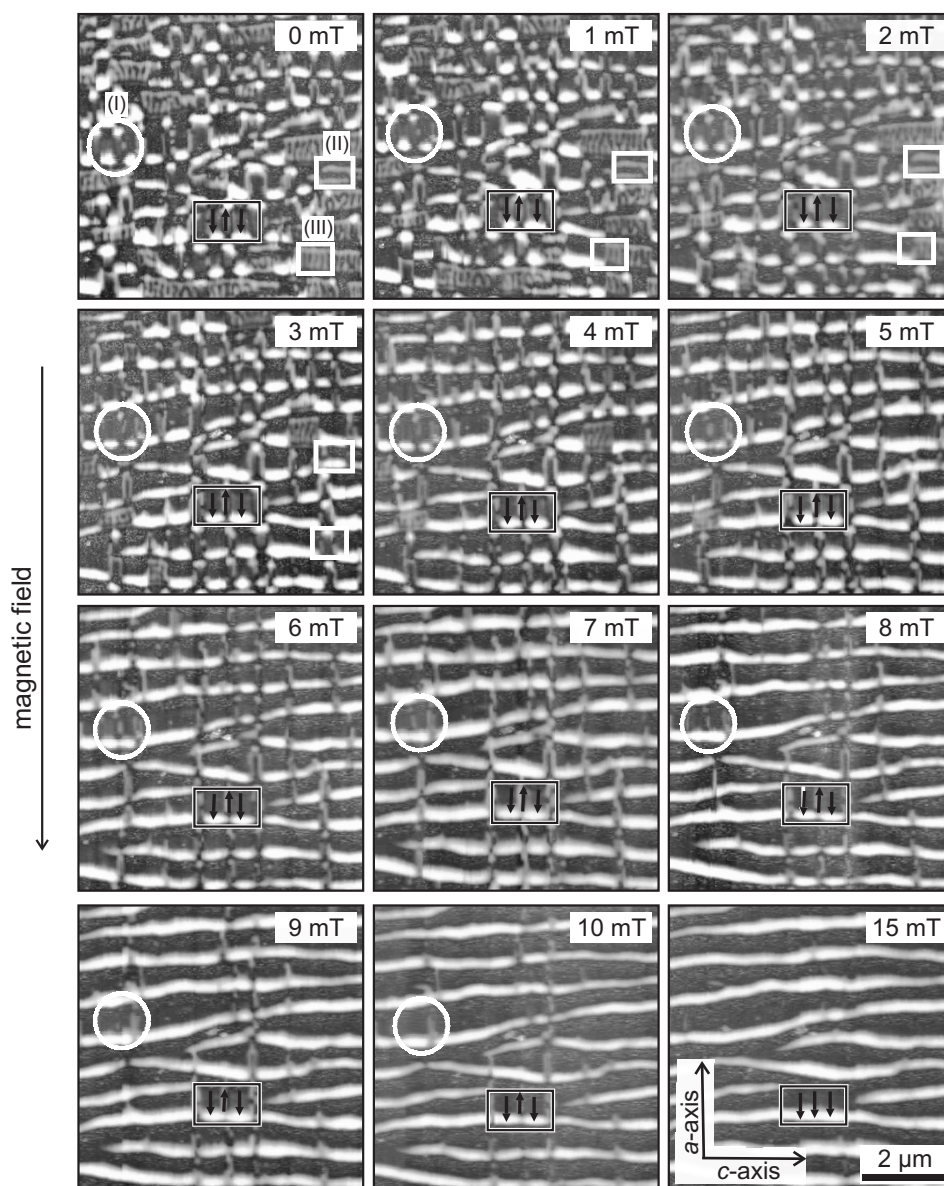


Figure 6.1: Room temperature field-dependent MFM measurements on MnAs-on-GaAs(001): field sequence of selected MFM scans recorded along the virgin curve. The field of 0 to 15 mT was applied along the easy axis direction, as indicated. The development of the three basic domain types can be followed looking at the white circular and rectangular markers. The domain configuration of a particular area with type (I) domains is highlighted (see black rectangle).

setup presented in Subsec. 3.3.2. The sample was aligned with the external magnetic field along the  $a$ -axis of MnAs. The demagnetized state was prepared by heating the film above the phase transition temperature until it was completely in the  $\beta$ -phase and then cooled down to room temperature in zero applied field. The MFM cantilevers had a spring constant of 0.05 N/m and a resonant frequency of 80 kHz. The tip was coated with a 60-nm-thick Cr-Co film, resulting in a radius of curvature at the tip apex of  $\sim 90$  nm [86]. The MFM tips were magnetized along the tip axis. Accompanying measurements of the magnetization hysteresis were carried out with a SQUID magnetometer [109].

Figure 6.1 shows a series of MFM images of the same sample area as a function of applied field. The different field values are indicated in each image. The areas marked by a white rectangles allow for a direct observation of the behavior of the basic domain types in an applied field. The arrows in the area marked by a black rectangle illustrate the magnetization distribution. At a field value between 1 and 2 mT, type (III)-related domains start to transform into type (I) domains. The last type (III)-related domains are driven out between 4 and 6 mT. Type (II) domains, on the other hand, transform into type (I) domains between 2 and 4 mT. Upon further increase of the

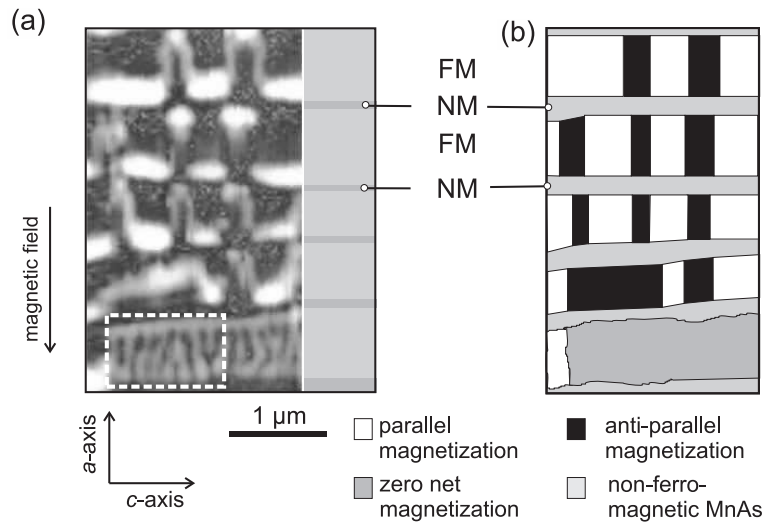


Figure 6.2: (a) MFM image of the MnAs film in a demagnetized state. The ferromagnetic (FM) and nonmagnetic (NM) stripes are indicated on the right-hand side of the figure. (b) Corresponding magnetization distribution showing areas of parallel, antiparallel, and zero net magnetization. The  $\beta$ -phase areas show light grey contrast.

field, the remaining type (I) domains get oriented in the field direction until, above 10 mT, all ferromagnetic stripes are in a single domain state (see black rectangle). Interestingly, the few type (I) domains that remain antiparallel magnetized up to above 10 mT are correlated across the stripes and finally align at 15 mT. At lower fields, these domains further exhibit irregular domain walls, different from the other antiparallel magnetized sections of the film that align at lower fields.

The results of the field-dependent MFM, which can be interpreted on a microscopic scale, are compared to SQUID measurements of the sample at room temperature. A detailed evaluation of the MFM data is shown in Fig. 6.2. The relative magnetization aligned in the direction of the external field is determined by analyzing the width of parallel and antiparallel magnetized type (I) domains of the ferromagnetic stripes along the  $c$ -axis as a function of applied field. Since type (II) domains and more complicated domain structures exhibit an almost vanishing net magnetization along the  $a$ -axis, they are neglected in the analysis. Finally, the absolute values for the magnetization are obtained by multiplying the deduced ratio of parallel and antiparallel magnetized type (I) domains with the magnetization of the fully

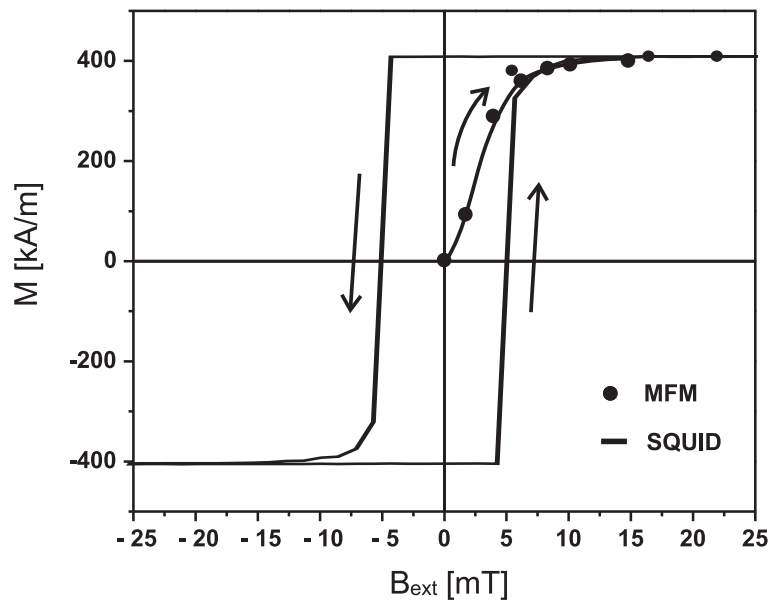


Figure 6.3: Hysteresis curve measured at room temperature with the field applied along the easy  $a$ -axis. The solid line shows the SQUID measurement and the black circles indicate the relative values obtained by field-dependent MFM. The value for the coercive field is  $\pm 5$  mT.

magnetized state measured by SQUID at 15 mT. The estimated values from MFM data analysis (black dots), as well as the hysteresis curve along with the virgin curve measured by SQUID magnetometry at room temperature (solid line), are shown in Fig. 6.3. Prior to the measurement of the virgin curve in SQUID, the sample was demagnetized in an alternating magnetic field.

To get a deeper insight into the intra-stripe domain structure and inter-stripe coupling in an applied field, micromagnetic simulations were performed. The geometry of the striped structure is deduced from the phenomenological phase-coexistence characteristics described in Sec. 2.3. In the beginning of the time-consuming simulation we falsely assumed a film thickness of 180 nm (nominal film thickness of grown layer). SEM measurements reveal a film thickness of 140 nm, however recent results show a qualitatively similar behavior for 140 nm thick films.

For a 180-nm-thick MnAs film the period of the stripes is  $p = 4.8 \cdot 180 \text{ nm} = 864 \text{ nm}$ . At room temperature, the phase fraction of the  $\alpha$ -phase is  $\phi(21^\circ\text{C}) = 0.88$ . Thus, the width of the ferromagnetic stripe is  $w_\alpha = 760 \text{ nm}$  and that of the nonmagnetic stripe  $w_\beta = 104 \text{ nm}$ .

The choice of the in-plane dimensions are a compromise between computational time, numerical convergence and length scale of the investigated phenomena. Since inter-stripe coupling is apparent too, the simulated area consists of at least two ferromagnetic stripes with a width of 760 nm, separated by a 100-nm-wide nonmagnetic stripe. Also, the length along the stripes has to be sufficient for realistic domains to form. The cell dimensions have to be of the order of the micromagnetic exchange length, which is 5 nm in the case of MnAs. For a good compromise between physical demands and calculation time, the sample was divided into  $128 \times 128 \times 14$  cells (length  $\times$  width  $\times$  thickness) of  $(13 \text{ nm})^3$ . The thickness of the film is 182 nm. Along the width of the stripes, the first and the last 60 cells can have a magnetic moment, separated by a buffer layer of 8 cells that corresponds to a width of the  $\beta$ -stripe ( $w_\beta = 104 \text{ nm}$ ). The width of the  $\alpha$ -stripe is slightly overestimated with  $w_\alpha = 780 \text{ nm}$  — a deviation of about 20 nm. Typical micromagnetic parameters for MnAs were used, as discussed in Chapter 4 and given in Sec. 5.2. The  $x$ -axis of the coordinate system of the simulator corresponds to the magnetocrystalline hard axis ( $c$ -axis), the  $y - z$ -plane to the easy plane, and the  $z$ -axis is along the film normal.

In accordance with the SQUID measurements, the ferromagnetic  $\alpha$ -stripes were assumed to be demagnetized in the start configuration. This was realized by initializing a random magnetization distribution with normalized magnetic moments for each cell, which is part of the ferromagnetic stripe. For the  $\beta$ -stripe, no magnetic moment was assumed. The initial magneti-

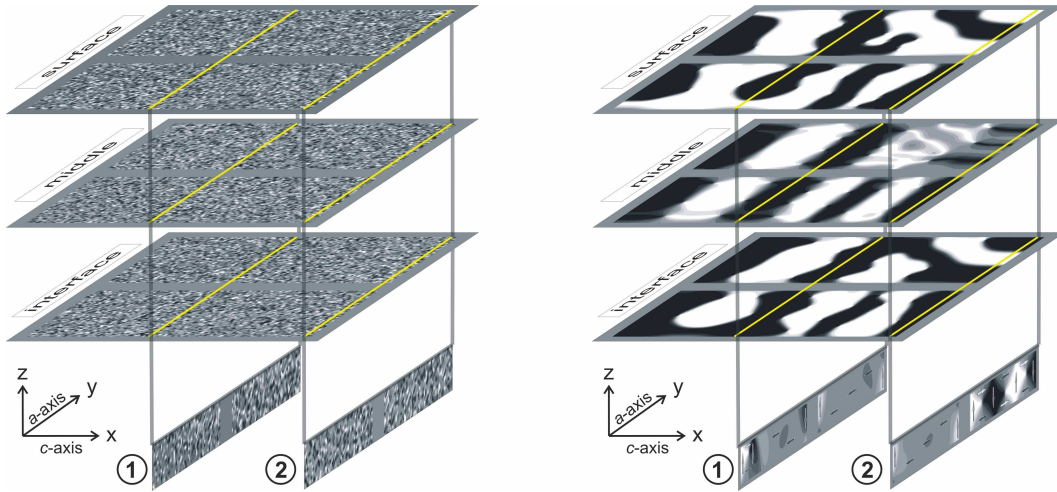


Figure 6.4: Magnetization distribution of (a) the initialized state (randomly magnetized) and (b) the relaxed state at zero applied field. The in-plane magnetization distribution  $m_y$  is visualized at three positions in film depth ( $z = \text{const}$ ): at the surface, in the middle of the film, and at the interface with the substrate. Two cross-sectional cuts along the  $a$ -axis ( $x = \text{const}$ ) show the  $z$ -component of the magnetization  $M_z$  at the positions labeled ① and ②.

zation distribution was allowed to relax at zero applied field. The result is shown in Fig. 6.4 for  $z = \text{const}$  at the surface (top), in the middle of the film (middle), and at the interface with GaAs (bottom). For the representation of the magnetization distribution, the in-plane component of the magnetization along the  $a$ -axis ( $m_y$ ) is chosen. Additionally, the magnetization distribution of the  $z$ -component of the magnetization ( $m_z$ ) in depth of selected cross-sectional cuts labeled ① and ② is shown in Fig. 6.4 (bottom). Note that the  $x$ -component of the magnetization is not shown, because the strong magnetocrystalline anisotropy of the system prevents a magnetization in the  $x$ -direction (the magnitude is always smaller than 1/50 of the total magnetization).

Three main domain types are identified, consistent with the MFM findings: type (I) is characterized by a uniform magnetization along the  $a$ -axis, also largely uniform in depth. A classical domain type (II), where the out-of plane magnetized domain is symmetrically located in the middle of the ferromagnetic stripe is not seen in Fig. 6.4, however domains that originate from oppositely magnetized areas can be identified in cross-section ① below. The simulations show that the surface magnetization distribution that led

to the classification scheme does not reach through the film. In fact, a single 'diamond' state turns out to be the origin of the type (II) stray fields. A type (III) domain is found along line ② top. The initial three-fold separation of the magnetization on the surface splits further up towards the middle of the film and becomes three-fold again close to the interface (inverted magnetization). The cross-section ② (top) reveals that the type (III) domains commonly observed in MFM are due to a double diamond state.

The stability of the simulated domain structure is studied in an applied magnetic field that was applied in the  $+y$ -direction and increased in steps of 2.5 mT up to 10 mT and of 6 mT beyond. The magnetization distribution for selected field values is shown in Fig. 6.5 for the in-plane cross-section ( $m_y$ ) and in Fig. 6.6 ( $m_z$ ) for a cross-sectional view of the easy plane along the cuts indicated in Fig. 6.5. Upon applying a magnetic field of 10 mT, a domain wall movement is obvious, leading to an increase of parallel magnetized domains (white contrast) and a reduction of the overall domain wall length. Both trends decrease the total energy. The straightening of the domain wall decreases the exchange energy and an expansion of parallel magnetized areas increases the Zeeman energy and thus reduces the total energy. An example of a domain wall straightening is apparent in the upper layer for the upper stripe by increasing the external field from 2.5 to 5 mT. The gradual domain wall movement is apparent everywhere in the series up to a complete alignment of the magnetization in the external field.

Additionally, a switching of the domains occurs from 16 mT on. First, type (III) domain changes to type (I), whereas antiparallel type (I) domains remain stable. Only near the boundary of the simulated structure antiparallel type (I) are aligned in the field. However, at this field only type (I) are stable. They are partially extended across the nonmagnetic spacer. Upon further increasing the applied field, the antiparallel domain that does not extend over both stripes, flips at 22 mT. The domain that is correlated remains stable up to 28 mT. This can be attributed to the presence of an inter-stripe interaction. The magnetostatic field of the adjacent ferromagnetic stripe acts like an additional biasing of the local effective field, which enables a switching of type (I) domains that are not correlated at smaller applied fields. For the correlated antiparallel type (I) domain, the stability is increased and a flipping occurs at higher fields. These findings are in accordance to the experimental observations. Type (I) domains is the more stable domains configuration at applied fields, for type (I) domains correlated across the stripes the switching occurs at larger field values.

The cross-sectional views along the indicated positions of the simulated structure, presented in Fig. 6.6, reveals a similar behavior. For the cuts at position ②, the ferromagnetic stripe shows a type (I) domain in an 'S' con-

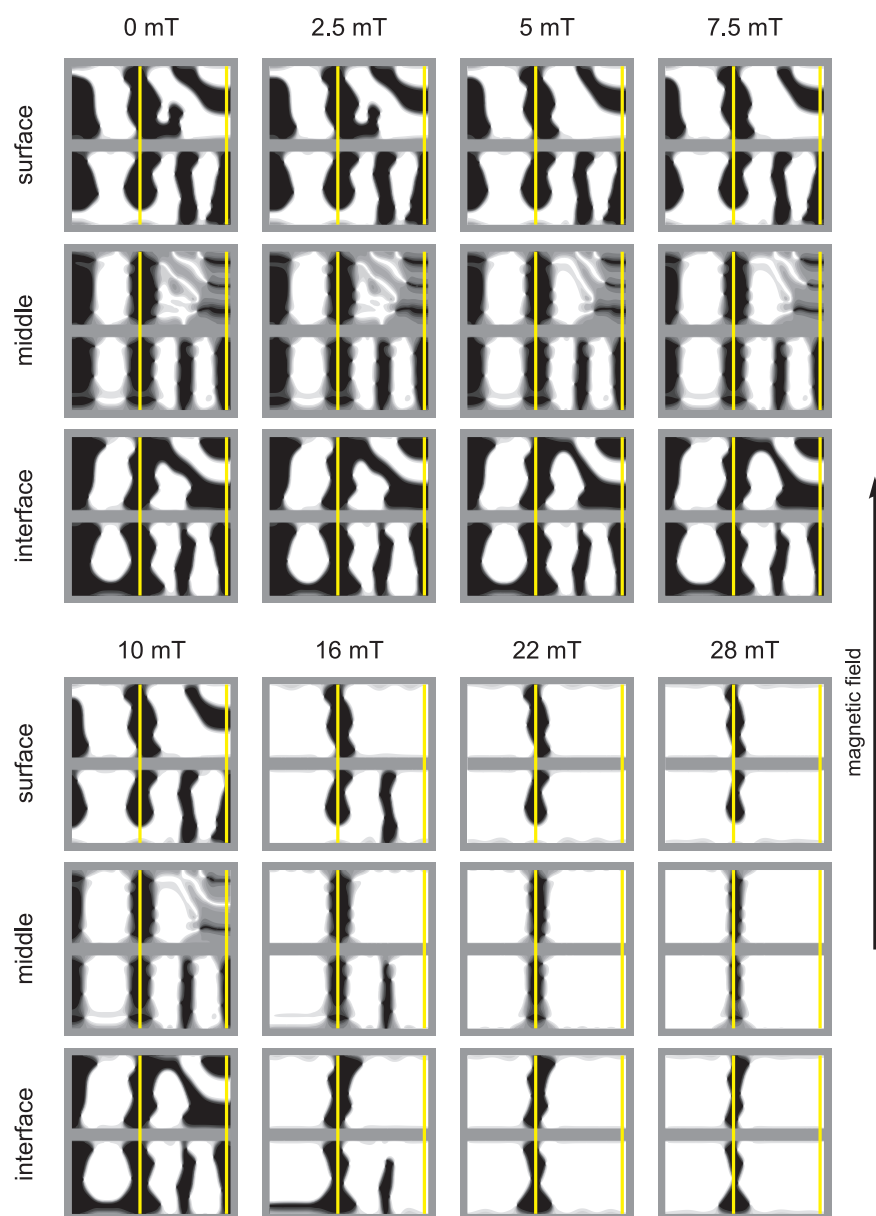


Figure 6.5: Field-dependence of the in-plane magnetization distribution  $m_y$  at the surface, in the middle, and at the interface of the MnAs film with GaAs. The direction of the applied magnetic field is shown on the right-hand side. The lines ① and ② indicate the positions of the cross-sections shown in Fig. 6.6.

figuration and a type (III) domain. Upon increasing the applied field, the domains of the 'S' state change to a flower state. At the edges of the ferromagnetic stripe the minor edge domain (black contrast) grows. At 7.5 mT, the flower state is fully developed and upon further increasing the applied field, it changes again to an 'S' state. The edge domains already extends far into the ferromagnetic stripe and a switching of the domain is almost initiated. For slightly higher fields the domain flips. The type (III) domain switches at 16 mT, however, the changes at smaller fields are not so pronounced. The type (III) exhibits a rotation of the out-of-plane magnetized domains ('diamonds') with increasing field, thereby increasing the size of the domains aligned along the applied field at the cost of the antiparallel aligned domains. Finally, in saturation, the cross-section of the ferromagnetic stripe shows a flower state.

For the cuts at position ① the situation is by far more complicated. In the beginning, domain types (I) and (II) are apparent, but they evolve differently upon increasing the applied field. The type (I) domain is in an 'S' state that remains up to 28 mT. The edge domain does not rotate to

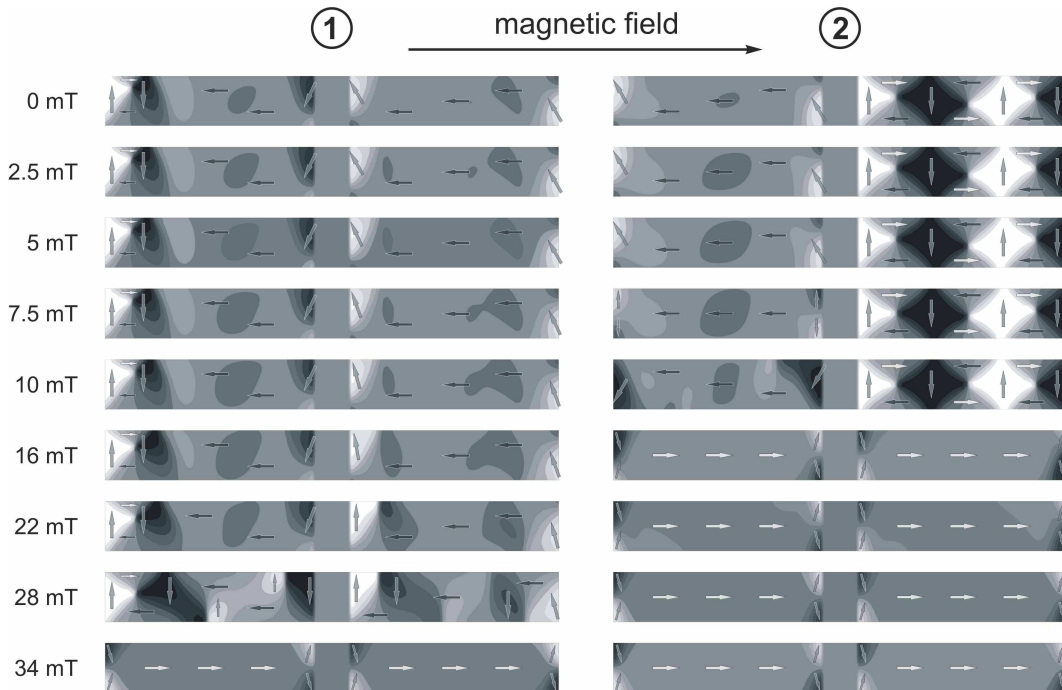


Figure 6.6: Field-dependence of the the out-of-plane magnetization distribution  $m_z$  of two selected cuts, indicated by lines ① and ② in Fig. 6.5.



initiate a switching event, but another domain type is introduced at higher fields, similar to the domain type (II). This is not the domain type (II) as introduced in the classification scheme in Sec. 5.2 but a vortex-like state. Whereas the diamond state shows a rotation of the diamond-like structure with increasing field, thereby reducing the antiparallel oriented moments, the vortex-like state remains pinned. The introduction of a vortex-like state at higher fields for the type (I) domain at the position of  $\textcircled{1}$  can be explained by a domain wall movement. The pinning centers are embedded in the domain walls.

The interesting question is why some domains switch at larger and some at lower fields. Already at zero applied field, the relaxed micromagnetic structure contains vortex-like configurations. They can be easily identified in the cross-sections of the middle layer, see Fig. 6.5. Between the domains, the  $y$ -component of the magnetization distribution ( $m_y$ ) is almost zero (see gray line). Here, the Bloch walls are located. At some points, however, the in-plane magnetization of adjacent domains almost touch each other. The domain transitions are very thin and these points act like a vortex which is persistent up to the disappearance of the antiparallel magnetized domains. They move in an applied field to allow an increase of parallel aligned domains. The vortex state acts like a pinning center and domains that are surrounded by many pinning centers remain up to higher fields. It has to be clarified, whether these points have a physical origin or have been introduced artificially in the simulation: the initial magnetization distribution of highly disordered magnetic moments at adjacent grid points can introduce the tendency of vortices. The exchange energy of the initial configuration is calculated to be 50 times higher than for the relaxed state, which supports that the initial configuration is magnetically highly disordered. Additionally, the three-point difference scheme of the exchange energy underestimates the gain in exchange energy, when neighboring magnetic moments have large angles between them (Sec. 4.2.1) and are tolerated. The discretization using cell sizes larger than the exchange length also underestimates the exchange.

To analyze the influence of the vortex-like structures on the experimental MFM images and to correlate the simulated domain structure with the experimental observations, the stray field of the simulated structure was calculated 100 nm above the surface (Fig. 6.7), i.e. at a typical working distance for MFM measurements. The stray field was obtained by the summation of the in-plane and out-of-plane magnetic field contributions obtained from the dipole approximation of the magnetization distribution. The measurement plane was sampled by a  $50 \times 50$  points grid with a step size of  $\Delta x = \Delta y = 40$  nm. In general, the simulated stray field images reproduce the typically measured MFM contrast. At zero applied field, three differ-

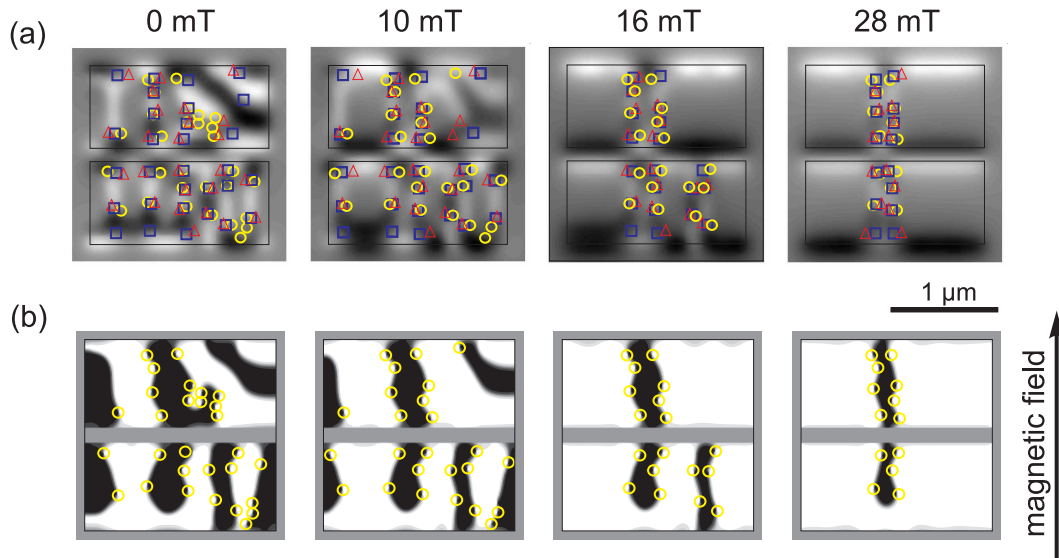


Figure 6.7: (a) Field-dependent calculation of the stray field ( $z$ -component) at a height of 100 nm above the simulated structure. The positions of the ferromagnetic stripes are indicated by rectangles. The circles mark the positions of pinning centers in the magnetization distribution for different depths: yellow circle, blue rectangle and red triangle for the position in the surface layer, middle layer and interface layer, respectively. (b) Magnetization distribution of the surface in-plane magnetization. The pinning centers are indicated by yellow circles.

ent domain types are observed. With increasing field, type (II) and (III) domains vanish. A small number of domains remains antiparallel magnetized and their size further decreases by domain wall movement. The stray field images show straight domain walls, whereas the magnetization distribution at the surface exhibits curved walls to connect the vortex-like pinning centers. Surprisingly, the vortex-like pinning centers are also visible in the calculated stray field. They correlate with the position where the apparent orientation of the domain wall changes. The contrast change occurs more often for the domain walls of the pinned domains. As already pointed out in the description of the experimental MFM images, the magnetic domains that flip at higher fields exhibit 'irregular' domain walls at lower fields. The irregularity can be attributed to a vortex-like structure, because the pinning of the domain and the fingerprint in the stray field coincide. It is not clear if the pinning centers in the experiment are due to structural inhomogeneities or a real feature of the magnetic structure.

In conclusion, the experimental findings and simulation results concerning the change of the proposed domain types in an applied field are consistent. The field range of switching events can be attributed to the pinning effect of the vortex-like structures and to the biasing effect of the neighboring ferromagnetic stripes. If the stripes are already aligned in an external field, the switching of the domains occurs at smaller fields. This may explain the systematic tendency of the simulated structure to align in the external field at higher values, since only two interacting stripes are simulated due to the limitations in computation time.

## 6.2 Magnetization reversal

So far, the stability of the domain structures in an applied field has been discussed, where the initial configuration is a completely demagnetized state. Now, a full hysteresis cycle is considered, starting from an initial magnetization configuration that shows saturation and complete alignment along the applied field. For the investigation of reversal processes, SQUID magnetometry and field-dependent MFM are used. The variable-field MFM measurements were performed with the rotatable permanent magnet setup explained in Chapter 3.3.2. The magnetic hysteresis loops were measured by SQUID magnetometry [109]. For a complete hysteresis cycle the external field was applied along the  $a$ -axis and  $c$ -axis direction in the film plane up to maximum field values of 2 T.

In general, two different behaviors were found in field-dependent MFM measurements at room temperature. Depending on the film thickness, in one case, the film magnetization switches collectively at the coercive field, while in the other case, the film demagnetizes almost completely in the remanent state. To find the origin of this behavior, a set of films with different thicknesses was systematically investigated with SQUID magnetometry at different temperatures. The obtained hysteresis curves are consistent with the MFM results. The two different magnetization reversal characteristics occur for all investigated films. The single domain behavior of thin films disappears for higher temperatures in the phase coexistence regime, whereas for thicker films the square-like hysteresis changes to the more rounded curves with low remanent magnetization already at lower temperatures.

The samples were prepared for the MFM experiments by first heating above the phase coexistence regime and then cooling them down resulting in the demagnetized state as described in Sec. 6.1. Then, the virgin curve was measured up to saturation with the field applied along the in-plane  $a$ -axis.

A series of MFM images acquired at 15°C is shown in Fig. 6.8 (a). Square-

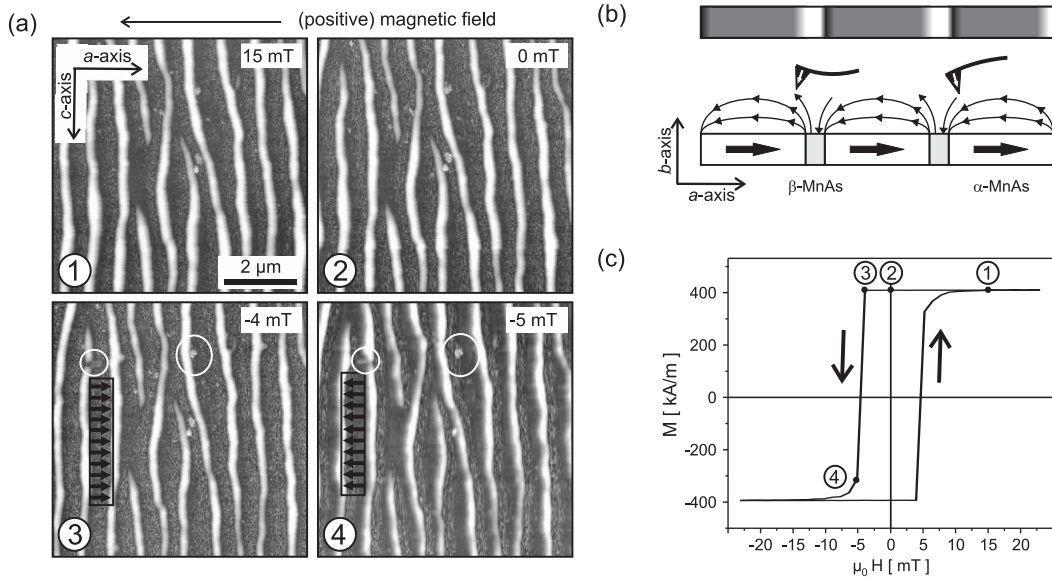


Figure 6.8: (a) MFM scans at 15°C corresponding to the decreasing field trace. The respective scans are indicated in the magnetization curve (c). The magnetization reversal occurs by the homogeneous switching of all stripes in the film. The white circle mark areas that are reference points as described in the text. The arrows in the rectangle indicate the magnetization of the particular area. (b) Sketch of the MFM contrast formation (bottom) and the resulting MFM contrast (top). (c) Hysteresis loop measured by SQUID magnetometry with the field applied along the easy *a*-axis direction at 15°C. The square-like hysteresis loop exhibits a coercive field of 5 mT.

like hysteresis loops are commonly observed in thin MnAs films. At 15 mT, the film is in a single domain state and the magnetization is along the positive direction of the applied magnetic field. It is not straightforward to interpret the MFM image of a saturated film in the coexistence regime. In this case, the MFM response shows neighboring dark and bright stripes, separated by larger gray areas. In Fig. 6.8(b), a schematic of the stray field (cross-section) of fully magnetized stripes is shown (bottom). The stray field emanates from the sample in the area of the  $\beta$ -MnAs stripes and points into and out-of the sample plane at the respective end of the domain. The MFM contrast obtained with a tip magnetized along its axis is bright (dark) in case of the stray field pointing out-of (into) the sample plane, as illustrated in Fig. 6.8(b) top. The position of the ferromagnetic stripes is verified by simultaneously acquired topography scans (not shown). The position of a ferromagnetic stripe segment is indicated by a black rectangle and the magnetization by arrows

[cf. measurements ③ and ④, Fig. 6.8(a)]. When reducing the applied field to zero, the observed domain structure remains unaffected, which is in accordance with the high remanent magnetization ratio  $M_r/M_s$  of 0.99 observed by SQUID magnetometry. A ratio of the remanent magnetization to the saturation magnetization  $M_r/M_s$  close to unity indicates that the reversible part of the magnetization is very small, as expected for coupled ferromagnetic stripes. This behavior continues down to almost -5 mT, where the coercive field is reached and the magnetization of the ferromagnetic stripes reverses collectively. The identification of the collective domain reversal is not obvious, since the changes in the MFM images are hard to identify. The striped structure is conserved, because the magnetization flips at once, however, the relative position of areas with attractive and repulsive interaction are changed. One way of recognizing the collective domain reversal in MFM is the tracking of topographical defects that are also visible as artifacts in the magnetic imaging mode, e.g. indicated by the white circle. Additionally, a pinned domain that has not flipped at -5 mT is indicated by another white circle, too. The pinned domains lead to a partial reversal, which shapes the hysteresis curve. The height of the tail is proportional to the number of pinned domains. The pinning is continuously driven out for higher fields up to a complete saturation at almost twice the switching field. This is in accordance with the findings for the switching fields in Sec. 6.1, where the pinned domains do also not switch until the applied field was doubled compared to the coercive field of unpinned type (I) domains.

In contrast to the square-like hysteresis loops observed for the 140-nm-thick film at 15°C, thicker MnAs films exhibit more rounded hysteresis loops with strongly reduced remanence. To investigate the properties of the rounded hysteresis loops in more detail, we performed MFM measurements of the micromagnetic domain structure on a 180-nm-thick film at 20°C. Especially in combination with AFM, the possible influences of structural defects on the magnetization and thus the hysteresis loop can be studied. The MFM images presented in Fig. 6.9 ( $T = 20^\circ\text{C}$ ) are obtained by first fully magnetizing the film. Upon decreasing the applied magnetic field, a single domain state is found (see image in Fig. 6.9 at 30 mT), as observed for the thin film in Fig. 6.8. The domains start to flip at 18 mT, leading to a multidomain state. The positions of the flipped domains appear to be correlated across the stripes (in the  $a$ -axis direction). Further, the magnetization reversal proceeds via the nucleation of reversed domains rather than domain wall propagation. The flipped domains are also spatially correlated, both in the  $a$ -axis direction as well as slightly tilted towards the  $c$ -axis direction (see 10 mT image of Fig. 6.9). This may have two origins: first, a magnetic effect due to coupling across the stripes or due to a disturbance by the MFM

tip. Second, besides the  $\alpha$ - $\beta$ -stripe structure, additional surface features are found in topography images that exhibit both an  $a$ -axis oriented as well as a slightly tilted step morphology [63]. It is very likely to assume a connection between morphological anomalies and the domain flipping. However, no di-

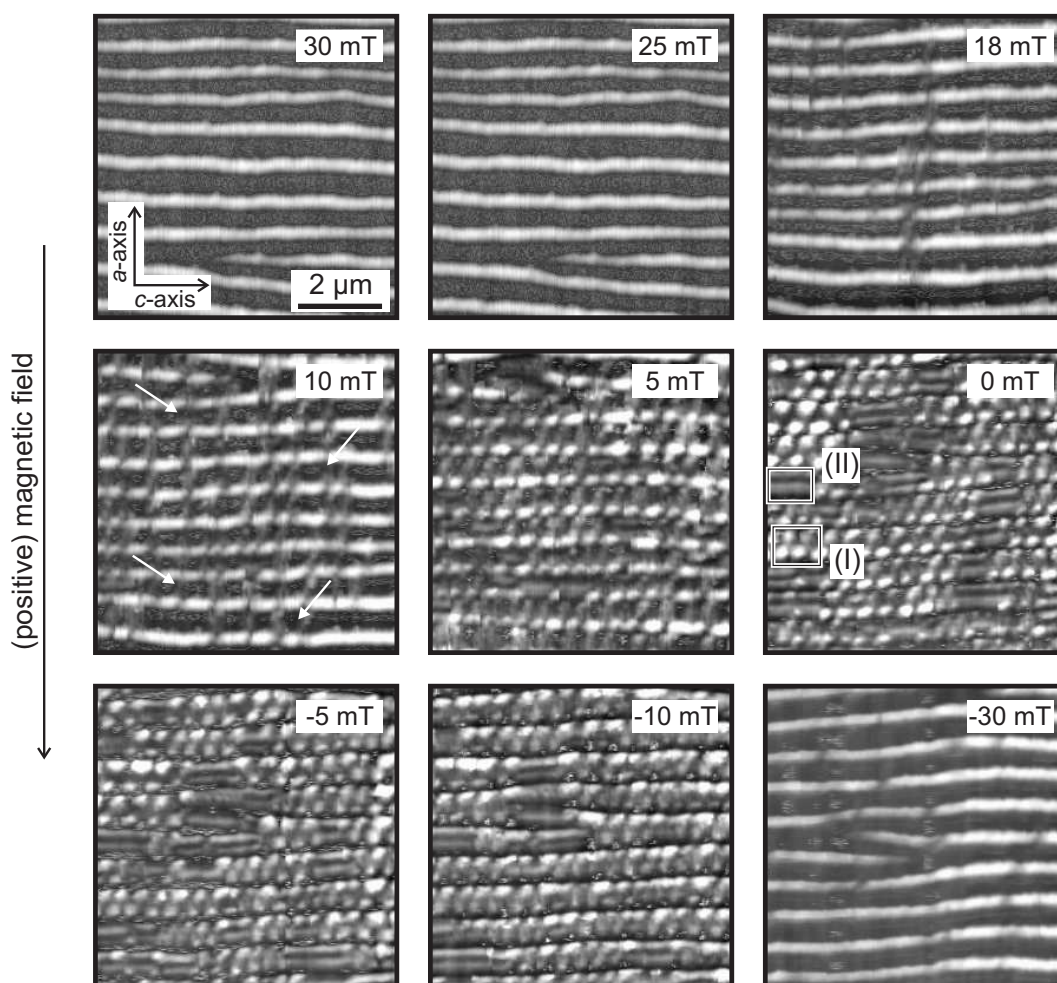


Figure 6.9: MFM images of a 180-nm-thick MnAs film recorded at decreasing applied fields as indicated. At 30 mT, the sample is fully magnetized. By reducing the applied field below 18 mT, a continuous decrease of the magnetization aligned in the field direction is observed. From 18 down to 10 mT, an increasing number of oppositely magnetized domains nucleate, however, no domain wall movement is obvious. The domains are correlated across the stripes along the  $a$ -axis direction. Below 10 mT, the extended single domains along a stripe decompose into segments of alternatingly magnetized domains. At zero applied field, the sample is almost completely demagnetized.

rect correlation between the surface defects and the position of the flipped domains was found. It will be discussed later that the nucleation of a domain with antiparallel magnetization is the reversal characteristic of flux-closure magnetic structures.

Below 10 mT, different domain types appear that all yield a very low net magnetization. On the one hand, alternating sequences of type (I) domains along the  $c$ -axis are formed, i.e. single domain across the width of the stripe. Alternating sequences of oppositely magnetized type (I) domains efficiently demagnetize the stripe as a whole. On the other hand, extended areas of type (II) domains appear. Type (II) domains are composed of two oppositely magnetized stripe segments along the  $a$ -axis direction.

Figure 6.10(a) shows the corresponding hysteresis loop measured at 25°C. The hysteresis curve is rounded with a very small remanent magnetization  $M_r/M_s = 0.12$ . The coercivity is approximately  $\pm 6$  mT. The curve resembles the behavior of a two-phase system consisting of a hard and a soft magnetic contribution [128]. The contribution of the part of the film that has a magnetically hard axis along the field direction can be identified in Fig. 6.10(b), where the influence of the hysteresis is canceled out by the

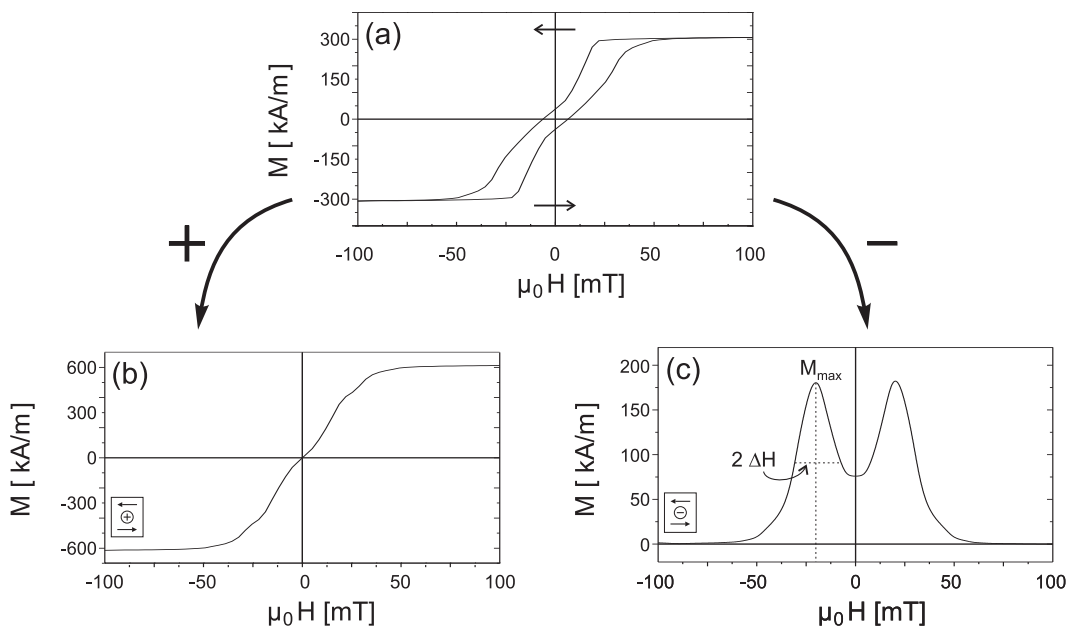


Figure 6.10: Hysteresis loop of a 180-nm-thick sample measured at 25°C (a). The added forward and backward scans (b), and the subtracted traces (c), reveal that the material behaves like a coupled two-phase system with a hard and a soft magnetic component.

addition of the forward and backward traces of the hysteresis loop. The curve shows an almost linear behavior and the magnetization saturates at approximately 60 mT. The presence of an additional soft axis loop can be extracted by the subtraction of the forward and backward traces, illustrated in Fig. 6.10(c). The symmetric two-peak structure shows maxima located at  $\pm 19$  mT. From the height of the maxima a remanent magnetization of  $M_{\max}/2 = 92 \text{ kA/m}^3$  is obtained, and the half width at half maximum leads to a field of  $\Delta H \approx 12$  mT.

To characterize the different magnetization reversal regimes in MnAs films, three film thicknesses at different temperatures in the phase coexistence interval between  $10 - 40^\circ\text{C}$  were investigated. The subtraction of the forward and backward branches of the hysteresis curve, i.e. the difference curve, is shown for 140, 180, and 215 nm thick films in Fig. 6.11 (a), (b), and (c), respectively. The curve at  $15^\circ\text{C}$  in Fig. 6.11(a) corresponds to the hysteresis curve presented in Fig. 6.8(c) and the curve at  $25^\circ\text{C}$  in Fig. 6.11(b) to Fig. 6.9.

The 140-nm-thick film shows difference curves from  $10^\circ\text{C}$  to above  $30^\circ\text{C}$  resembling a rectangle function centered around zero applied field. The rectangular shape is corresponding to an ideal square-like hysteresis loop. The width of the curve is twice the coercive field  $H_c$  and the height twice the remanent magnetization  $M_r$ . With increasing temperature,  $M_r$  decreases because of the temperature-dependent decrease of the ferromagnetic  $\alpha$ -phase content. At  $30^\circ\text{C}$ , the curve becomes rounded at zero applied field and a

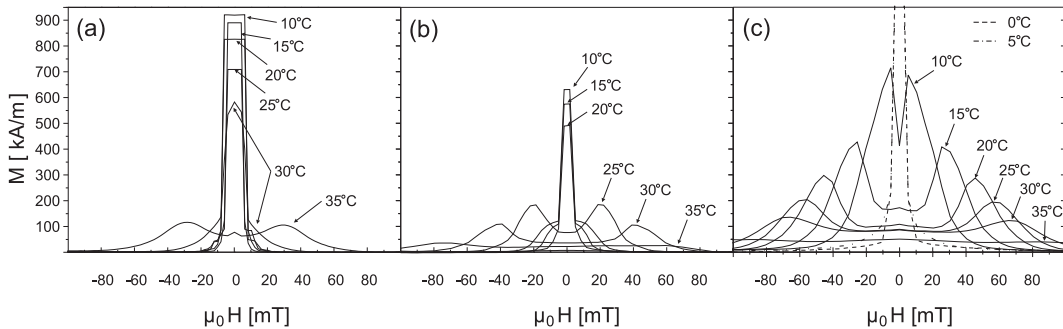


Figure 6.11: Subtracted hysteresis curves for (a) 140, (b) 180, and (c) 215 nm thick MnAs films; all three curves are plotted using the same scaling. Independent of film thickness, a double peak structure is visible at higher temperatures. For lower temperatures, all films exhibit square-like hysteresis loops resulting in the step-like function centered around zero field. In case of the 215-nm-thick film, square-like loops start appearing below the  $\alpha$ - $\beta$ -phase coexistence temperature of  $10^\circ\text{C}$ .



shoulder develops at fields slightly higher than  $H_c$ . At this temperature, a transition takes place from the square-like hysteresis regime to the previously described two-phase characteristics. At 35°C, the two-phase behavior is fully developed. The 180-nm-thick film tends to the same qualitative behavior, however, the transition takes place between 20°C and 25°C. Furthermore, the offset of the maxima in the two-phase regime increases with increasing temperature. Below the transition temperature, the rectangular curves exhibit a convex decay slightly above the coercive field, whereas the side lobe changes to a concave shape at 20°C.

The thicker film (215 nm) starts exhibiting the two-phase behavior already at the onset temperature of the  $\alpha$ - $\beta$ -phase coexistence regime of 10°C. Therefore, Fig. 6.11(c) also shows measurements at 0 and 5°C, i.e. fully in the  $\alpha$ -phase. These two rectangular curves clearly indicate the square-like loop behavior. The shift of the split maxima is larger than for the 180-nm-thick film at the same temperature. The same observations are made on a large set of samples, reaching from very thin samples (25 nm) to samples up to the maximum thickness of 500 nm at which cracking is observed [20, 21].

How does the magnetization reversal occur in MnAs films on GaAs(001)? The experimental findings can be summarized as follows: a double peak structure is visible in the hysteresis difference curves at higher temperatures, independent of film thickness. With increasing film thickness, the two peaks already form at lower temperatures. The offset of the double peaks at a given temperature is larger for thicker films. Two-phase loops are well-known for systems composed of a hard and a soft magnetic phase [128, 129]. In this system, we observe (i) morphological features which might indicate a magnetically different phase, and, (ii) different MnAs orientations on GaAs(001). (i) In case of the 180-nm-thick film, the MFM images in Fig. 6.9 reveal a correlation of the flipped domains across the stripes in the array. The onset of the correlated magnetic features at fields below 18 mT determines the further nucleation of domains. A similar streaky pattern is also found in topography scans, however, no correlation between topographic and magnetic features was verified. (ii) As mentioned above, A- and B-oriented MnAs is rotated by 90° with respect to each other in the film plane, such that the easy axis of magnetization lies in the hard axis direction of the other phase. A hysteresis loop in the hard axis direction of A-oriented MnAs, which is a sign of B-oriented MnAs in the film, was not found for the investigated samples. Furthermore, one would expect the full saturation of the magnetization along the  $a$ -axis to occur at an applied field of 2 T (which is the saturation field of the hard axis), and not at 60 mT as observed in Fig. 6.11. As the

B- to A-oriented phase ratio is high for thin films, and since phase mixing only occurs in the interfacial area, thin films should exhibit a stronger alteration of the magnetic properties. This means that the B-orientation is not responsible for the pinning either.

Thus, it is worth to directly investigate the magnetization reversal of the micromagnetic structure of an individual stripe. The magnetization reversal of an 'S' state is well known from calculations of a number of thin film elements, where the 'S' state lies in the film plane [37, 111]. The switching occurs in principle between two oppositely magnetized states exhibiting a steep transition in magnetization at the coercive field. The resulting square-like loop is slightly rounded as a result of the edge domains. This behavior is experimentally found for thin films, as well as for thicker films at low temperatures. For thicker films, the remanent state is most likely a Landau state which exhibits a reduced remanent magnetization. In high applied fields, the Landau state transforms into a so-called flower state that is closest to a uniformly magnetized state with deviations from the main magnetization direction at all four edges (cf. upper right-hand side inset in Fig. 6.12). Consequently, the hysteresis loop is characterized by the gradual transition from the flower state to the Landau state, resulting in a partial demagnetization of the sample already at large applied fields. For very thick films, the remanent state is dominated by the occurrence of a single or double diamond state. Again, at large applied fields, the sample exhibits a flower state. The corresponding hysteresis curve is similar to the result obtained for films with a Landau state at remanence. However, the switching from the flower to the diamond state occurs already at larger applied fields, leading to the observed broadening of the magnetization difference curves [compare Fig. 6.11(b) and (c)].

Figure 6.12 shows the simulated hysteresis loop of a 208-nm-thick MnAs sample related to the Landau state. The magnetization reversal was studied on a sample measuring width (along  $a$ -axis)  $\times$  width (along  $c$ -axis)  $\times$  thickness =  $416 \times 1664 \times 208 \text{ nm}^3$  and a cell size of 13 nm. The ratio of width (along  $a$ -axis) to thickness of 2 : 1 corresponds to a temperature of approximately 30°C. For these parameters it is not assumed that inter-stripe related phenomena affect the reversal and it is sufficient to simulate a single stripe. The hysteresis curve was calculated starting with a fully magnetized sample at 500 mT with the magnetization pointing in the  $+y$ -direction. The field was gradually reduced and the relaxed magnetization distribution was calculated. At selected fields, cross-sectional views of the magnetization distribution in the easy plane are shown. The calculated hysteresis loop is qualitatively in good agreement with the observed curve shown in Fig. 6.10. As discussed above, the film starts in a flower state at high fields. Upon

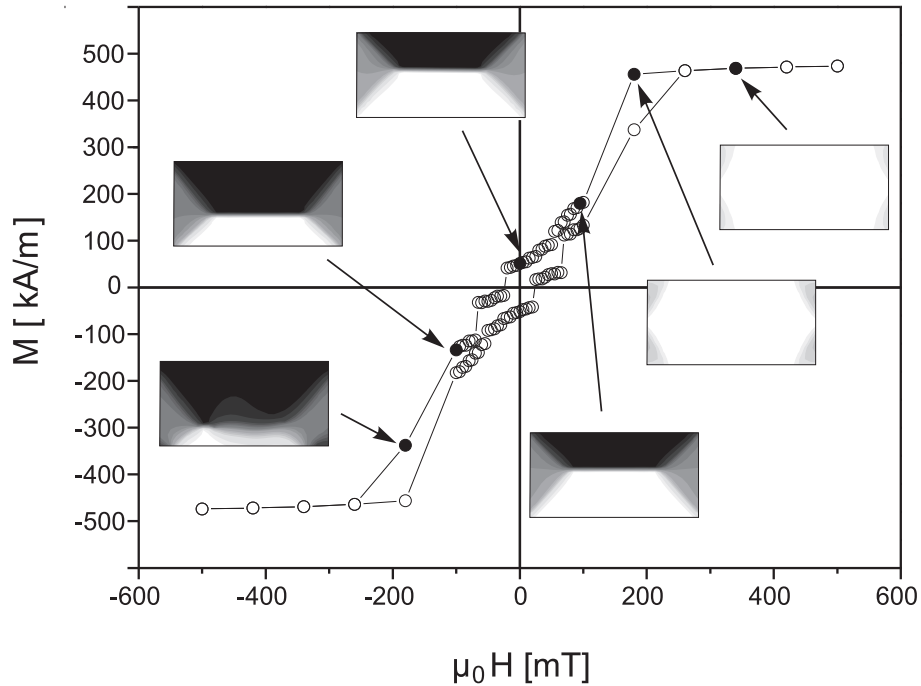


Figure 6.12: Simulated hysteresis loop for a 208-nm-thick MnAs film showing a Landau state at remanence. The magnetic field is applied along the in-plane  $a$ -axis direction. The insets show cross-sectional views of the magnetization distribution in the easy plane. The grayscale plots represent the magnetization component  $m_y$  at the respective field values.

decreasing the field, the edge domains grow thereby reducing the magnetization only slightly. At approximately 200 mT the field is small enough for the nucleation of a large, oppositely magnetized domain (cf. cross-sectional view at 120 mT). This Landau state is asymmetric — in contrast to the Landau state at remanence. For a lower temperature of approximately 20°C, i.e., a stripe width of 832 nm, a diamond state is nucleating at lower field, resulting in a narrower magnetization difference curve as the one observed experimentally [cf. Fig. 6.11(c)].

The numerical simulations lead to a basic understanding of magnetization reversal and the involved processes. Additional simulations reveal that the exact hysteresis curves depend to a large degree on the geometry of the simulated slab, and less on the chosen material parameters. Depending on pinning effects (not related to material inhomogeneities) and the chosen cell size, the coercive field can shift although the overall curve shape remains the same. Due to the uncertainty in some material parameters of MnAs, the

exact experimental geometry, and the lack of material inhomogeneities that might be responsible for the nucleation process, it is not reasonable to try to reproduce the experimental curve quantitatively.

# Chapter 7

## Summary

In this thesis, the micromagnetic structure of the material system MnAs-on-GaAs has been studied. The experimental work is based on MFM measurements and their interpretation is supplemented by XMCDPEEM data. Based on qualitative MFM response calculations, using the analytical solution of the stray field of uniaxial bar magnets, a classification scheme of the domain structure has been proposed. Three different domain types are distinguished according to the number of domains across the width of the stripe. The MFM contrast can be explained resulting from an arrangement of bar-shaped uniaxial domains. There is a good qualitative agreement of simulation and experiment, and the proposed domain structure is further confirmed by XMCDPEEM. Nevertheless, the deduced domain configuration is associated with an unreasonable magnetization distribution. The main obstacle is the unreasonable assumption of a straight domain wall separating head-on domains. Additionally, MFM and XMCDPEEM results differ for thicker films, which suggests the existence of a complex three-dimensional domain configuration.

To resolve these inconsistencies, and to unambiguously determine the micromagnetic structure of the stripe array, a simulator was developed. It allows for the calculation of the three-dimensional magnetization distribution of large structures. The equilibrium magnetization distribution is obtained by the time integration of the Landau-Lifshitz-Gilbert equation, whereby the demagnetization energy is calculated efficiently using a fast Fourier transformation technique. The reliability of the simulator was successfully demonstrated solving the micromagnetic standard problem #1.

In a first step, the micromagnetic simulator was applied to the MnAs stripe structure. Distinct domain patterns evolve as a result of the system's attempt to reduce its energy through the formation of flux-closure patterns in the easy plane. The domain patterns are consistent with the classification

scheme. However, the simulations reveal that the domain transition between head-on domains – apparent in type (II) and type (III) domains – is not a domain wall but an out-of-plane magnetized domain. The reason is the planar symmetry of the magnetocrystalline anisotropy, favoring the magnetization in the basal plane. For films thicker than a critical value of 100 nm, a nucleation of out-of-plane magnetized domains effectively reduces the demagnetization energy of the stripe due to the formation of flux-closure patterns. The possible domain structures are not only affected by the thickness of the film, but also by the width and distance of the ferromagnetic stripes, and thus by the temperature.

Several magnetic phenomena have been investigated in the light of the three-dimensional micromagnetic structure. For film thicker than 200 nm a zig-zag pattern is observed in XMCDPEEM. Depending on the width of the ferromagnetic stripes, which is a function of temperature, the zig-zag angle increases from  $90^\circ$  in the case of wide stripes to a straight wall for narrow stripes. A diamond-like state consisting of two intersecting sub-surface domain walls is the underlying magnetic structure resulting in the observed domain walls. The zig-zag pattern of the domain boundary is explained by stray field minimization of the diamond state along the stripe.

The magnetic coupling of submicron-sized stripes was investigated by temperature-dependent MFM and XMCDPEEM. A specific coupling state can be selected by a certain combination of stripe period and width, i.e. film thickness and temperature. Micromagnetic imaging in combination with simulations reveals two coupling regimes: strong magnetic coupling between the stripes creates micromagnetic domains extended across several stripes, whereas weak coupling allows for demagnetization within individual stripes. The observed behavior is universal for all film thicknesses as the geometrical relationship of stripe period and film thickness is constant. For thicker films, the breakdown of inter-stripe coupling occurs at lower temperatures which is attributed to a stronger tendency to nucleate flux-closure type domains.

To investigate the influence of the easy plane character of the magnetocrystalline anisotropy, we study the micromagnetic properties of MnAs grown on GaAs(111)B where the  $c$ -axis is normal to the surface. As expected, these films exhibit completely different domain patterns compared to films on GaAs(001). In the course of the first order phase transition, ferromagnetic  $\alpha$ -MnAs forms a network of quasi-hexagonal areas separated by  $\beta$ -MnAs. The analysis of the XMCDPEEM images and simulations reveal closure domains that mainly appear either as a vortex-like state or a stripe structure.

For possible applications the magnetization reversal behavior has to be understood. For this purpose, variable-temperature MFM was complemented with a magnetic field setup. To avoid sample heating, and thus to combine magnetic fields with a precise temperature control, the magnetic field unit uses a rotatable permanent magnet. Variable amounts of flux can be guided via the yoke towards the sample.

The stability of the different domain types at remanence is investigated. Increasing fields drive out the complex domains first, leaving alternating type (I) domains behind. The remaining magnetization process aligns an increasing fraction of the domains along the field direction by domain wall movement. Micromagnetic simulations confirm the observed behavior.

The magnetization reversal was studied by MFM imaging in conjunction with SQUID magnetometry and micromagnetic simulations. The investigated thin samples show square-like hysteresis loops and the corresponding field-dependent MFM measurements confirm a collective flipping of the domains at the coercive field. Thicker samples, as well as thinner samples at higher temperatures, generally exhibit a rounded magnetization curve with a very low remanent magnetization. Based on three-dimensional micromagnetic simulations, the micromagnetic structure as well as the magnetic hysteresis are explained in a consistent way.

In the future, a detailed investigation of the influence of size, shape and distribution of the ferromagnetic areas on the micromagnetic structure of MnAs/GaAs(111)B should be performed. Moreover, nanofabrication techniques can be applied to the patterning of MnAs to extend the investigation to other confined geometries. Since MnAs is conductive, it is very interesting to investigate the magnetotransport properties on the nanoscale.

The development of the MFM contrast simulation package – that has been integrated with the micromagnetic simulator – enables the quantitative calculation of the tip-sample interaction. Its general concept allows the application to arbitrary probe-sample combinations, which have not been accessible for present simulators so far. It can also be used to predict experimental parameters for optimal MFM contrast and resolution. Finally, the possibility to calculate mutual tip-sample disturbances dynamically will provide the necessary quantitative insight into this useful, yet difficult to interpret, micromagnetic imaging technique.

# Bibliography

- [1] L. Abelman, S. Porthun, M. Haast, C. Lodder, A. Moser, M. E. Best, P. J. A. van Schendel, B. Stiefel, H. J. Hug, G. P. Heydon, A. Farley, S. R. Hoon, T. Pfaffelhuber, R. Proksch, and K. Babcock. Comparing the resolution of magnetic force microscopes using the CAMST reference samples. *J. Magn. Magn. Mater.*, 190:135–147, 1998.
- [2] A. Aharoni. Demagnetizing factors for rectangular ferromagnetic prisms. *J. Appl. Phys.*, 83:3432–3434, 1998.
- [3] K. Akeura, M. Tanaka, M. Ueki, and T. Nishinaga. Epitaxial ferromagnetic MnAs thin films grown by molecular beam epitaxy on Si (001) substrates. *Applied Physics Letters*, 67:3349–3351, Nov. 1995.
- [4] K. Akeura, M. Tanaka, T. Nishinaga, and J. de Boeck. Epitaxial ferromagnetic MnAs thin films grown on Si (001): The effect of substrate annealing. *Journal of Applied Physics*, 79:4957–4959, 1996.
- [5] T. R. Albrecht, P. Grütter, D. Horne, and D. Rugar. Frequency modulation detection using high-Q cantilevers for enhanced force microscope sensitivity. *Journal of Applied Physics*, 69:668–673, 1991.
- [6] Armco soft iron. URL "<http://www.remag.de/>".
- [7] G. E. Bacon and R. Street. Magnetic Structure of Manganese Arsenide. *Nature*, 175:518, 1955.
- [8] E. Bauer. Photoelectron microscopy . *Journal of Physics Condensed Matter*, 13:11391–11404, Dec. 2001.
- [9] E. Bauer. LEEM Basics. *Surface Review and Letters*, 5:1275–1286, 1998.
- [10] E. Bauer. *et al.* unpublished.



- [11] E. Bauer, S. Cherifi, L. Däweritz, M. Kästner, S. Heun, and A. (Locatelli). Low-energy electron microscopy/x-ray magnetic circular dichroism photoemission electron microscopy study of epitaxial MnAs on GaAs. *J. Vac. Sci. Technol. B*, 20(6):2539–2542, 2002.
- [12] C. P. Bean and D. S. Rodbell. Magnetic Disorder as a First-Order Phase Transformation. *Physical Review*, 126:104–115, Apr. 1962.
- [13] K. D. Belashchenko. Anisotropy of exchange stiffness and its effect on the properties of magnets. *Journal of Magnetism and Magnetic Materials*, 270:413–424, Apr. 2004.
- [14] D. V. Berkov and N. L. Gorn. Micromagus. URL "<http://www.micromagus.de>".
- [15] W. F. Brown. *Micromagnetics*. Wiley, New York, 1963.
- [16] D. E. Bürgler and P. A. Grünberg. *Magnetoelectronics - Magnetism and Magnetotransport in Layered Structures*. Wiley-VCH, 1st edition, 2003. ISBN 3-527-40363-9.
- [17] P. Carra, B. T. Thole, M. Altarelli, and X. Wang. X-ray circular dichroism and local magnetic fields. *Physical Review Letters*, 70:694–697, 1993.
- [18] V. A. Chernenko, L. Wee, P. G. McCormick, and R. Street. Giant magnetoelastic response in MnAs. *Journal of Applied Physics*, 85:7833–7837, 1999.
- [19] A. K. Das, C. Pampuch, A. Ney, T. Hesjedal, L. Däweritz, R. Koch, and K. H. Ploog. Ferromagnetism of MnAs Studied by Heteroepitaxial Films on GaAs(001). *Physical Review Letters*, 91(8):087203–+, 2003.
- [20] L. Däweritz, L. Wan, B. Jenichen, C. Herrmann, J. Mohanty, A. Trampert, and K. H. Ploog. Thickness dependence of the magnetic properties of MnAs films on GaAs(001) and GaAs(113)A: Role of a natural array of ferromagnetic stripes. *Journal of Applied Physics*, 96:5056–5062, 2004.
- [21] L. Däweritz, C. Herrmann, J. Mohanty, T. Hesjedal, K. H. Ploog, E. Bauer, A. Locatelli, S. Cherifi, R. Belkhou, A. Pavlovska, and S. Heun. Tailoring of the structural and magnetic properties of MnAs films grown on GaAs—Strain and annealing effects. *J. Vac. Sci. Technol. B*, 23(4):1759–1768, 2005.

- [22] R. W. De Blois and C. D. J. Graham. Domain Observations on Iron Whiskers. *Journal of Applied Physics*, 29(6):931–939, 1958.
- [23] R. W. De Blois and D. S. Rodbell. Magnetic First-Order Phase Transition and Anisotropy in Single-Crystal MnAs. *Journal of Applied Physics*, 34(4):1101–1103, 1963.
- [24] R. W. De Blois and D. S. Rodbell. Magnetic First-Order Phase Transition in Single-Crystal MnAs. *Physical Review*, 130:1347–1360, 1963.
- [25] M. Donahue and D. Porter. Object Oriented MicroMagnetic Framework (OOMMF). URL "<http://math.nist.gov/oommf>".
- [26] M. J. Donahue and D. G. Porter. Exchange energy formulations for 3D micromagnetics. *Physica B Condensed Matter*, 343:177–183, 2004.
- [27] W. Döring. *Mikromagnetismus*, volume 18/2. Springer, Berlin, 1966.
- [28] H. Ebert, J. Stöhr, S. S. P. Parkin, M. Samant, and A. Nilsson. L-edge x-ray absorption in fcc and bcc Cu metal: Comparison of experimental and first-principles theoretical results. *Phys. Rev. B*, 53:16067–16073, 1996.
- [29] ELETTRA. - BL 1.2L - Nanospectroscopy Beamline technical data. URL "<http://www.elettra.trieste.it/experiments/beamlines/nano/index.html>".
- [30] R. Engel-Herbert and T. Hesjedal. Calculation of the magnetic stray field of a uniaxial magnetic domain. *Journal of Applied Physics*, 97(7):074504, 2005.
- [31] R. Engel-Herbert, J. Mohanty, A. Ney, T. Hesjedal, L. Däweritz, and K. H. Ploog. Understanding the submicron domain structure of MnAs thin films on GaAs(001): Magnetic force microscopy measurements and simulations. *Applied Physics Letters*, 84:1132–1134, 2004.
- [32] R. Engel-Herbert, R. Hesjedal, D. M. Schaadt, L. Däweritz, and K. H. Ploog. Micromagnetic properties of MnAs(0001)/GaAs(111) epitaxial films. *Applied Physics Letters*, 88(5):052505, 2006.
- [33] R. Engel-Herbert, D. M. Schaadt, S. Cherifi, E. Bauer, R. Belkhou, A. Locatelli, S. Heun, A. Pavlovska, J. Mohanty, K. H. Ploog, and T. Hesjedal. The nature of charged zig-zag domains in MnAs thin films. *Journal of Magnetism and Magnetic Materials*, 305:457–463, 2006.

- [34] V. H. Etgens, M. Eddrief, D. Demaille, Y. L. Zheng, and A. Ouerghi. Growth morphology of MnAs epilayers on GaAs(1 1 1)-B substrates by molecular beam epitaxy. *J. Cryst. Growth*, 240:64–72, 2002.
- [35] Euxine Technologies, Magsimus. URL "<http://www.euxine.com>".
- [36] J. Fidler and T. Schrefl. TOPICAL REVIEW: Micromagnetic modelling - the current state of the art. *Journal of Physics D Applied Physics*, 33:135–+, 2000.
- [37] J. Fidler, R. W. Chantrell, T. Schrefl, and M. A. Wongsam. *Micromagnetics I: Basic principles*. Elsevier, Amsterdam. ISBN 0-08-0431526.
- [38] M. J. Freiser. Zigzag form of charged domain-walls. *IBM Journal of Research and Development*, 23:330–338, 1979.
- [39] M. Frigo and S. G. Johnson. Fastest Fourier Transform in the West. URL "<http://www.fftw.org/>".
- [40] J. M. García, A. Thiaville, J. Miltat, K. J. Kirk, J. N. Chapman, and F. Alouges. Quantitative interpretation of magnetic force microscopy images from soft patterned elements. *Applied Physics Letters*, 79:656–658, 2001.
- [41] C. J. García-Cervera, Z. Gimbutas, and W. E. Accurate numerical methods for micromagnetics simulations with general geometries. *Journal of Computational Physics*, 184:37–52, 2003.
- [42] F. J. Giessibl. A direct method to calculate tip-sample forces from frequency shifts in frequency-modulation atomic force microscopy. *Applied Physics Letters*, 78(1):123–125, 2001.
- [43] T. Göddenhenrich, H. Lemke, M. Mück, U. Hartmann, and C. Heiden. Probe calibration in magnetic force microscopy. *Applied Physics Letters*, 57:2612–2614, 1990.
- [44] R. D. Gomez, A. O. Pak, A. J. Anderson, E. R. Burke, A. J. Leyendecker, and I. D. Mayergoyz. Quantification of magnetic force microscopy images using combined electrostatic and magnetostatic imaging. *Journal of Applied Physics*, 83:6226–6228, 1998.
- [45] F. Grønvold, S. Snildal, and J. E. F. Westrum. Manganese monoarsenide - thermodynamic properties in Range 5 to 700 degrees K and transition behavior. *Acta Chemica Scandinavica*, 24:285, 1970.

- [46] P. Grütter, A. Wadas, E. Meyer, H. Heinzelmann, H.-R. Hidber, and H.-J. Guntherodt. High resolution magnetic force microscopy. *Journal of Vacuum Science and Technology A: Vacuum, Surfaces, and Films*, 8(1):406–410, 1990.
- [47] P. Grütter, H. J. Marmin, and D. Rugar. *Magnetic Force Microscopy (MFM)*, volume 28. Springer, Berlin, Heidelberg, New York, 1998.
- [48] C. Guillaud. Les points de transformation des composés définis MnAs, MnBi en relation avec un mécanisme probable d'antiferromagnétisme. *Journal de Physique et le Radium*, 12:223–227, 1951.
- [49] U. Hartmann. The point dipole approximation in magnetic force microscopy. *Phys. Lett. A*, 137:475–478, 1989.
- [50] C. Herring and C. Kittel. On the Theory of Spin Waves in Ferromagnetic Media. *Physical Review*, 81:869–880, 1951.
- [51] F. Heusler. Über Manganbronze und über die Synthese magnetisierbarer Legierungen aus unmagnetischen Metallen. *Zeitschrift für Angewandte Chemie*, 17:260–264, 1904.
- [52] S. Hosaka, A. Kikukawa, and Y. Honda. High resolution of magnetic force microscope image using a just-on-surface magnetic force microscope. *Jpn. J. Appl. Phys.*, 33:3779–3784, 1994.
- [53] A. Hubert and R. Schäfer. Springer, Berlin, 1998. ISBN 3-540-64108-4. URL "<http://wwwold.ifw-dresden.de/~thicksim/schaefer/Glos/home.htm>".
- [54] H. J. Hug, B. Stiefel, P. J. A. van Schendel, A. Moser, R. Hofer, S. Martin, H.-J. Güntherodt, S. Porthun, L. Abelmann, J. C. Lodder, G. Bochi, and R. C. O'Handley. Quantitative magnetic force microscopy on perpendicularly magnetized samples. *Journal of Applied Physics*, 83:5609–5620, 1998.
- [55] IBS Magnet. URL "<http://www.ibs-magnet.de/>".
- [56] S. Imada, S. Suga, W. Kuch, and J. Kirschner. Magnetic Microspectroscopy by a Combination of XMCD and PEEM. *Surface Review and Letters*, 9:877–881, 2002.
- [57] F. Ishikawa, K. Koyama, K. Watanabe, and H. Wada. Field induced structural transformation in MnAs. *Japanese Journal of Applied Physics Part 2-Letters*, 42:L918–L920, 2003.

- [58] J. D. Jackson. Walter de Gruyter, Berlin, 2. auflage edition, 1983. ISBN 3-11-009579-3.
- [59] B. Jenichen, V. M. Kaganer, M. Kästner, C. Herrmann, L. Däweritz, K. H. Ploog, N. Darowski, and I. Zizak. Structural and magnetic phase transition in MnAs(0001)/GaAs(111) epitaxial films. *Phys. Rev. B*, 68(13):132301–+, 2003.
- [60] V. M. Kaganer, B. Jenichen, F. Schippan, W. Braun, L. Däweritz, and K. H. Ploog. Strain-Mediated Phase Coexistence in Heteroepitaxial Films. *Physical Review Letters*, 85:341–344, 2000.
- [61] V. M. Kaganer, B. Jenichen, F. Schippan, W. Braun, L. Däweritz, and K. H. Ploog. Strain-mediated phase coexistence in MnAs heteroepitaxial films on GaAs: An x-ray diffraction study. *Phys. Rev. B*, 66(4):045305–+, 2002.
- [62] M. Kästner, L. Däweritz, and K. H. Ploog. Surface reconstruction, screw dislocations and anisotropic step flow growth of MnAs on GaAs (1 1 1)B substrates. *Surf. Sci.*, 511:323–330, 2002.
- [63] M. Kästner, L. Däweritz, and K. H. Ploog. Atomic scale morphology of self-organized periodic elastic domains in epitaxial ferromagnetic MnAs films. *Journal of Applied Physics*, 92(10):5711–5713, 2002.
- [64] T. Kebe and A. Carl. Calibration of magnetic force microscopy tips by using nanoscale current-carrying parallel wires. *Journal of Applied Physics*, 95:775–792, 2004.
- [65] D. Kolovos-Vellianitis, C. Herrmann, L. Däweritz, and K. H. Ploog. Structural and magnetic properties of epitaxially grown MnAs films on GaAs(110). *Applied Physics Letters*, 87:092505–+, 2005.
- [66] L. Kong and S. Y. Chou. Quantification of magnetic force microscopy using a micronscale current ring. *Applied Physics Letters*, 70:2043–2045, 1997.
- [67] F. Krause, F. Kaisinger, H. Starke, G. Persch, and U. Hartmann. The influence of experimental parameters on contrast formation in magnetic force microscopy. *Thin Solid Films*, 264:141–147, 1995.
- [68] L. Landau and E. Lifshitz. On the theory of the dispersion of magnetic permeability in ferromagnetic bodies. *Physikalische Zeitschrift Sowjetunion*, 8:153–169, 1935.

- [69] J. Lindner, T. Toliński, K. Lenz, E. Kosubek, H. Wende, K. Baberschke, A. Ney, T. Hesjedal, C. Pampuch, R. Koch, L. Däweritz, and K. H. Ploog. Magnetic anisotropy of MnAs-films on GaAs(001) studied with ferromagnetic resonance. *Journal of Magnetism and Magnetic Materials*, 277:159–164, 2004.
- [70] C. Liu, K. Lin, R. Holmes, G. J. Mankey, H. Fujiwara, H. Jiang, and H. Seok Cho. Calibration of magnetic force microscopy using micron size straight current wires. *Journal of Applied Physics*, 91:8849–8851, 2002.
- [71] A. Locatelli, A. Bianco, D. Cocco, S. Cherifi, S. Heun, M. Marsi, M. Pasqualetto, and E. Bauer. High lateral resolution spectroscopic imaging of surfaces: The undulator beamline “nanospectroscopy” at Elettra. *Journal de Physique IV*, 104:99–102, 2003.
- [72] J. Lohau, S. Kirsch, A. Carl, G. Dumpich, and E. F. Wassermann. Quantitative determination of effective dipole and monopole moments of magnetic force microscopy tips. *Journal of Applied Physics*, 86:3410–3417, 1999.
- [73] H. J. Mamin, D. Rugar, J. E. Stern, R. E. Fontana, Jr., and P. Kasiraj. Magnetic force microscopy of thin Permalloy films. *Applied Physics Letters*, 55:318–320, 1989.
- [74] M. Mansuripur. Magnetization reversal dynamics in the media of magneto-optical recording. *Journal of Applied Physics*, 63:5809–5823, 1988.
- [75] M. Mansuripur. Computation of fields and forces in magnetic force microscopy. *IEEE Transactions on Magnetics*, 25:3467–3469, 1989.
- [76] Y. Martin and H. K. Wickramasinghe. Magnetic imaging by “force microscopy” with 1000 Å resolution. *Applied Physics Letters*, 50:1455–1457, 1987.
- [77] Y. Martin, C. C. Williams, and H. K. Wickramasinghe. Atomic force microscope-force mapping and profiling on a sub 100-Å scale. *Journal of Applied Physics*, 61:4723–4729, 1987.
- [78] N. Mattoso, M. Eddrief, J. Varalda, A. Ouerghi, D. Demaille, V. H. Etgens, and Y. Garreau. Enhancement of critical temperature and phases coexistence mediated by strain in MnAs epilayers grown on GaAs (111) B. *Phys. Rev. B*, 70(11):115324–+, 2004.

- [79] S. McVitie, R. P. Ferrier, J. Scott, G. S. White, and A. Gallagher. Quantitative field measurements from magnetic force microscope tips and comparison with point and extended charge models. *Journal of Applied Physics*, 89:3656–3661, 2001.
- [80] N. Menyuk, J. A. Kafalas, K. Dwight, and J. B. Goodenough. Effects of Pressure on the Magnetic Properties of MnAs. *Physical Review*, 177: 942–951, 1969.
- [81] Micromagnetic Modeling Activity Group, National Institute of Standards and Technology.  $\mu$ Mag Standard Problem Strategy. URL "<http://www.ctcms.nist.gov/~rdm/mumag.html>".
- [82] Mikromasch. URL "<http://www.spmtips.com/products/cantilevers/datasheets/co-cr/>".
- [83] J. J. Miles and M. Jones. An accurate and efficient 3-D micromagnetic simulation of metal evaporated tape. *Journal of Magnetism and Magnetic Materials*, 171:190–208, 1997.
- [84] J. Mira, F. Rivadulla, J. Rivas, A. Fondado, T. Guidi, R. Caciuffo, F. Carsughi, P. G. Radaelli, and J. B. Goodenough. Structural Transformation Induced by Magnetic Field and “Colossal-Like” Magnetoresistance Response above 313 K in MnAs. *Phys. Rev. Lett.*, 90(9): 097203, 2003.
- [85] M. Mizugushi, H. Kuramochi, J. Okabayashi, T. Manago, and H. Akimaga. Magnetic domain structure of MnAs thin films as a function of temperature. *Materials Transactions*, 44:2578–2581, 2003.
- [86] MMR Technologies Inc. URL "<http://www.mmr.com>". Micro miniature refrigerator with a K-20 temperature controller.
- [87] J. Mohanty, T. Hesjedal, T. Plake, M. Kästner, L. Däweritz, and K. H. Ploog. Variable-temperature micromagnetic study of epitaxially grown MnAs films on GaAs(001). *Applied Physics A: Materials Science & Processing*, 77:739–742, 2003.
- [88] J. Mohanty, R. Engel-Herbert, and T. Hesjedal. Variable magnetic field and temperature magnetic force microscopy. *Applied Physics A: Materials Science & Processing*, 81:1359–1362, 2005.
- [89] J. Mohanty, Y. Takagaki, T. Hesjedal, L. Däweritz, and K. H. Ploog. Selective etching of epitaxial MnAs films on GaAs(001): Influence of structure and strain. *Journal of Applied Physics*, 98(1):013907, 2005.

- [90] J. R. Mohanty. *Micromagnetic investigation of MnAs thin films on GaAs surfaces*. PhD thesis, Humboldt University Berlin, 2005.
- [91] G. E. Moore. Cramming more components onto integrated circuits. *Electronics*, 38:114, 1965. URL "<http://www.intel.com/technology/mooreslaw/index.htm>".
- [92] G. E. Moore. Talk at the International Electron Devices Meeting, 1975. URL "<http://www.intel.com/technology/mooreslaw/index.htm>".
- [93] MPI. The Message Passing Interface (MPI) standard. URL "<http://www-unix.mcs.anl.gov/mpi/>".
- [94] S. Müller-Pfeiffer, M. Schneider, and W. Zinn. Imaging of magnetic domain walls in iron with a magnetic force microscope: A numerical study. *Phys. Rev. B*, 49:15745–15752, 1994.
- [95] A. J. Newell, W. Williams, and D. J. Dunlop. A generalization of the demagnetizing tensor for nonuniform magnetization. *Journal of Geophysical Research*, 98:9551–9555, 1993.
- [96] A. Ney, C. Pampuch, R. Koch, and K. H. Ploog. Programmable computing with a single magnetoresistive element. *Nature*, 425:485–487, 2003.
- [97] A. Ney, T. Hesjedal, C. Pampuch, A. K. Das, L. Däweritz, R. Koch, K. H. Ploog, T. Toliński, J. Lindner, K. Lenz, and K. Baberschke. Nature of the magnetic and structural phase transition in MnAs/GaAs(001). *Phys. Rev. B*, 69(8):081306–+, 2004.
- [98] A. Ney, T. Hesjedal, L. Däweritz, R. Koch, and K. H. Ploog. Extending the magnetic order of MnAs films on GaAs to higher temperatures. *Journal of Magnetism and Magnetic Materials*, 288:173–177, 2005.
- [99] M. K. Niranjan, B. R. Sahu, and L. Kleinman. Density functional determination of the magnetic state of  $\beta$ -MnAs. *Phys. Rev. B*, 70(18):180406–+, 2004.
- [100] J. O. Oti. Numerical micromagnetic techniques and their applications to magnetic force microscopy calculations. *IEEE Transactions on Magnetics*, 29:2359–2364, 1993.



- [101] D. V. Ovchinnikov and A. A. Bukharaev. Computer Simulation of Magnetic Force Microscopy Images with a Static Model of Magnetization Distribution and Dipole–Dipole Interaction. *Technical Physics*, 46:1014–1019, 2001.
- [102] C. Pampuch, A. K. Das, A. Ney, L. Däweritz, R. Koch, and K. H. Ploog. Magnetologic with  $\alpha$ -MnAs Thin Films. *Physical Review Letters*, 91(14):147203–+, 2003.
- [103] T. Plake, M. Ramsteiner, V. M. Kaganer, B. Jenichen, M. Kästner, L. Däweritz, and K. H. Ploog. Periodic elastic domains of coexisting phases in epitaxial MnAs films on GaAs. *Applied Physics Letters*, 80:2523–2525, 2002.
- [104] S. Porthun, L. Abelmann, S. J. L. Vellekoop, J. C. Lodder, and H. J. Hug. Optimization of lateral resolution in magnetic force microscopy. *Applied Physics A: Materials Science & Processing*, 66:1185–1189, 1998.
- [105] W. H. Press, B. P. Flanery, S. A. Teukolsky, and W. T. Vetterling. In *Numerical Recipes Example Book C*. Cambridge University Press, Cambridge, 1988. ISBN 0521357462. URL "<http://www.nr.com/>".
- [106] G. A. Prinz. Hybrid ferromagnetic-semiconductor structures. *Science*, 250:1092–1097, 1990.
- [107] G. A. Prinz. Spin-polarized transport. *Physics Today*, 48:58–63, 1995.
- [108] R. B. Proksch, S. Foss, and E. D. Dahlberg. High resolution magnetic force microscopy of domain wall fine structures. *IEEE Transactions on Magnetics*, 30:4467–4472, 1994.
- [109] Quantum Design. URL "<http://www.qdusa.com/products/mpms.html>". MPMS SQUID VSM.
- [110] M. Ramsteiner, H. Y. Hao, A. Kawaharazuka, H. J. Zhu, M. Kästner, R. Hey, L. Däweritz, H. T. Grahn, and K. H. Ploog. Electrical spin injection from ferromagnetic MnAs metal layers into GaAs. *Phys. Rev. B*, 66(8):081304–+, 2002.
- [111] W. Rave and A. Hubert. Magnetic ground state of a thin-film element. *IEEE Transactions on Magnetics*, 36:3886–3899, 2000.

- [112] W. Rave, K. Ramstöck, and A. Hubert. Corners and nucleation in micromagnetics. *Journal of Magnetism and Magnetic Materials*, 183:329–333, 1998.
- [113] D. Rugar, H. J. Mamin, P. Guethner, S. E. Lambert, J. E. Stern, I. McFadyen, and T. Yogi. Magnetic force microscopy: General principles and application to longitudinal recording media. *Journal of Applied Physics*, 68:1169–1183, 1990.
- [114] J. J. Sáenz, N. García, P. Grütter, E. Meyer, H. Heinzelmann, R. Wiesendanger, L. Rosenthaler, H. R. Hidber, and H.-J. Güntherodt. Observation of magnetic forces by the atomic force microscope. *Journal of Applied Physics*, 62:4293–4295, 1987.
- [115] E. Sasioglu, I. Galanakis, L. M. Sandratskii, and P. Bruno. Stability of ferromagnetism in the half-metallic pnictides and similar compounds: a first-principles study. *Journal of Physics Condensed Matter*, 17:3915–3930, 2005.
- [116] M. R. Scheinfein, J. Unguris, D. T. Pierce, and R. J. Celotta. High spatial resolution quantitative micromagnetics. *Journal of Applied Physics*, 67:5932–5937, 1990.
- [117] R. Scheinfein. LLG Micromagnetics Simulator. URL "<http://llgmicro.home.mindspring.com>".
- [118] F. Schippan. *Materialintegration von Halbleitern mit magnetischen Werkstoffen*. PhD thesis, Humboldt University Berlin, 2000.
- [119] F. Schippan, A. Trampert, L. Däweritz, and K. H. Ploog. Kinetics of MnAs growth on GaAs(001) and interface structure. *Journal of Vacuum Science and Technology B*, 17:1716–1721, 1999.
- [120] F. Schippan, G. Behme, L. Däweritz, K. H. Ploog, B. Dennis, K.-U. Neumann, and K. R. A. Ziebeck. Magnetic structure of epitaxially grown MnAs on GaAs(001). *Journal of Applied Physics*, 88:2766–2770, 2000.
- [121] F. Schippan, M. Kästner, L. Däweritz, and K. H. Ploog. Growth control of MnAs on GaAs(001) by reflection high-energy electron diffraction. *Applied Physics Letters*, 76:834–836, 2000.
- [122] T. Schmidt, S. Heun, J. Slezak, J. Diaz, K. C. Prince, G. Lilienkamp, and E. Bauer. SPELEEM: Combining LEEM and Spectroscopic Imaging. *Surface Review and Letters*, 5:1287–1296, 1998.

- [123] T. Schmidt, J. Slezak, S. Heun, J. Diaz, R. R. Blyth, R. Delaunay, D. Cocco, K. C. Prince, E. Bauer, and M. Coreno. Optical layout of a beamline for photoemission microscopy. *Journal of Synchrotron Radiation*, 6:957–963, 1999.
- [124] W. Scholz, J. Fidler, T. Schrefl, D. Suess, R. Dittrich, H. Forster, and V. Tsiantos. Scalable parallel micromagnetic solvers for magnetic nanostructures. *Computational Materials Science*, 28:366–383, 2003.
- [125] T. Schrefl, J. Fidler, D. Süß, and V. Tsiantos. *Micromagnetic simulation of dynamic and thermal effects*. Springer, Berlin, 1998.
- [126] G. Schütz, W. Wagner, W. Wilhelm, P. Kienle, R. Zeller, R. Frahm, and G. Materlik. Absorption of circularly polarized x rays in iron. *Physical Review Letters*, 58:737–740, 1987.
- [127] J. Scott, S. McVitie, R. P. Ferrier, and A. Gallagher. Electrostatic charging artefacts in Lorentz electron tomography of MFM tip stray fields. *Journal of Physics D Applied Physics*, 34:1326–1332, 2001.
- [128] R. Skomski. Nanomagnetism. *Journal of Physics–Condensed Matter*, 15:R841–R896, 2003.
- [129] R. Skomski and J. M. D. Coey. Giant energy product in nanostructured two-phase magnets. *Phys. Rev. B*, 48:15812–15816, 1993.
- [130] R. Skomski, A. Kashyap, J. Zhou, and D. J. Sellmyer. Anisotropic exchange. *J. Appl. Phys.*, 97(10):10B302+, 2005.
- [131] J. Stöhr. Exploring the microscopic origin of magnetic anisotropies with X-ray magnetic circular dichroism (XMCD) spectroscopy. *Journal of Magnetism and Magnetic Materials*, 200:470–497, 1999.
- [132] J. Stöhr and S. Anders. X-ray spectro-microscopy of complex materials and surfaces. *IBM Journal of Research and Development*, 44:535–551, 2000.
- [133] J. Stöhr, H. A. Padmore, S. Anders, T. Stammler, and M. R. Scheinfein. Principles of X-Ray Magnetic Dichroism Spectromicroscopy. *Surface Review and Letters*, 5:1297–1308, 1998.
- [134] D. G. Streblechenko, M. R. Scheinfein, M. Mankos, and K. Babcock. Quantitative magnetometry using electron holography: field profiles near magnetic force microscope tips. *IEEE Transaction on Magnetics*, 32:4124–4129, 1996.

- [135] Y. Takagaki, E. Wiebicke, M. Ramsteiner, L. Däweritz, and K. H. Ploog. Spontaneous growth of arsenic oxide micro-crystals on chemically etched MnAs surfaces. *Applied Physics A: Materials Science & Processing*, 76:837–840, 2003.
- [136] Y. Takagaki, E. Wiebicke, L. Däweritz, and K. H. Ploog. Distribution of  $\alpha$  and  $\beta$  phases in the coexistence regime in MnAs(0001) layers grown on GaAs(111)B. *Applied Physics Letters*, 85:1505–+, 2004.
- [137] K. M. Tako, M. A. Wongsam, and R. W. Chantrell. Numerical simulation of 2D thin films using a finite element method. *Journal of Magnetism and Magnetic Materials*, 155:40–42, 1996.
- [138] M. Tanaka. Ferromagnet (MnAs)/III-V semiconductor hybrid structures. *Semiconductor Science and Technology*, 17:327–341, 2002.
- [139] M. Tanaka. Epitaxial ferromagnetic thin-films and superlattices of Mn-based metallic compounds on GaAs. *Materials Science and Engineering B*, 31:117–125, 1995.
- [140] M. Tanaka. Epitaxial ferromagnetic thin films and heterostructures of Mn-based metallic and semiconducting compounds on GaAs. *Physica E: Low-dimensional Systems and Nanostructures*, 2:372–380, 1998.
- [141] M. Tanaka, J. P. Harbison, M. C. Park, Y. S. Park, T. Shin, and G. M. Rothberg. Epitaxial orientation and magnetic properties of MnAs thin films grown on (001) GaAs: Template effects. *Applied Physics Letters*, 65:1964–1966, 1994.
- [142] M. Tanaka, J. P. Harbison, M. C. Park, Y. S. Park, T. Shin, and G. M. Rothberg. Epitaxial ferromagnetic MnAs thin films grown by molecular-beam epitaxy on GaAs: Structure and magnetic properties. *Journal of Applied Physics*, 76:6278–6280, 1994.
- [143] M. Tanaka, J. P. Harbison, T. Sands, T. L. Cheeks, V. G. Keramidas, and G. M. Rothberg. Molecular beam epitaxy of MnAs thin films on GaAs. *Journal of Vacuum Science and Technology B*, 12:1091–1094, 1994.
- [144] R. C. Taylor and A. Gangulee. Magnetization and magnetic anisotropy in evaporated GdCo amorphous films. *Journal of Applied Physics*, 47:4666–4668, 1976.

- [145] A. Thiaville, L. Belliard, D. Majer, E. Zeldov, and J. Miltat. Measurement of the stray field emanating from magnetic force microscope tips by Hall effect microsensors. *Journal of Applied Physics*, 82:3182–3191, 1997.
- [146] B. T. Thole, P. Carra, F. Sette, and G. van der Laan. X-ray circular dichroism as a probe of orbital magnetization. *Physical Review Letters*, 68:1943–1946, 1992.
- [147] T. Tolinski, J. Lindner, K. Lenz, K. Baberschke, A. Ney, T. Hesjedal, C. Pampuch, L. Däweritz, R. Koch, and K. H. Ploog. Magnetic coupling and exchange stiffness in striped MnAs films. *Europhysics Letters*, 68:726–732, 2004.
- [148] S. L. Tomlinson and A. N. Farley. Micromagnetic model for magnetic force microscopy tips. *Journal of Applied Physics*, 81:5029–5031, 1997.
- [149] A. Trampert. Heteroepitaxy of dissimilar materials: effect of interface structure on strain and defect formation. *Physica E: Low-dimensional Systems and Nanostructures*, 13:1119–1125, 2002.
- [150] V. D. Tsiantos, J. J. Miles, and B. K. Middleton. Stiffness in Micromagnetic Simulations. 16th IMACS World Congress 2000 on Scientific Computation, Applied Mathematics and Simulation, August 21–25, 2000, Lausanne, Switzerland. URL "<http://magnet.atp.tuwien.ac.at/ts/>".
- [151] B. Vellekoop, L. Abelmann, S. Porthun, and C. Lodder. On the determination of the internal magnetic structure by magnetic force microscopy. *Journal of Magnetism and Magnetic Materials*, 190:148–151, 1998.
- [152] R. H. Victora. Quantitative theory for hysteretic phenomena in CoNi magnetic thin films. *Physical Review Letters*, 58:1788–1791, 1987.
- [153] G. Wastlbauer and J. A. C. Bland. Structural and magnetic properties of ultrathin epitaxial Fe films on GaAs(001) and related semiconductor substrates. *Advances in Physics*, 54:137–219, 2005.
- [154] B. T. M. Willis and H. P. Rooksby. Magnetic Transitions and Structural Changes in Hexagonal Manganese Compounds. *Proceedings of the Physical Society B*, 67:290–296, 1954.

- [155] R. H. Wilson and J. S. Kasper. Crystal structure of MnAs above 40 degrees C. *Acta Crystallographica.*, 17:95–&, 1964.
- [156] T. M. Wright, W. Williams, and D. J. Dunlop. An improved algorithm for micromagnetics. *Journal of Geophysical Research*, 102:12085–12094, 1997.
- [157] R. P. Yongsunthon, J. McCoy, and E. D. (Williams). Calibrated magnetic force microscopy measurement of current-carrying lines. *J. Vac. Sci. Technol. A*, 19:1763–1768, 2001.
- [158] R. P. Yongsunthon, A. Stanishevsky, E. D. Williams, and P. J. Rous. Mapping electron flow using magnetic force microscopy. *Appl. Phys. Lett.*, 82:3287–3289, 2003.
- [159] S. W. Yuan and H. N. Bertram. Fast adaptive algorithms for micromagnetics. *IEEE. Transactions on Magnetism*, 28:2031–2036, 1992.
- [160] X. Zhu and P. Grütter. Imaging, manipulation, and spectroscopic measurements of nanomagnets by magnetic force microscopy. *MRS Bulletin*, 29:457–462, 2004.
- [161] R. Zorn. *Magnetometrie*. Forschungszentrum Jülich, Jülich, 1999.

# Danksagung

Mein Dank gilt allen, die mich auf die eine oder andere Weise bei der Anfertigung dieser Arbeit unterstützt haben. Mein besonderer Dank gilt

Prof. Dr. K. H. Ploog für die Möglichkeit zur Promotion am Paul-Drude-Institut.

Prof. Dr. Thorsten Hesjedal für die Zusammenarbeit und Betreuung. Während meiner Promotion habe ich sehr viel von Ihm gelernt. Ich bin froh, daß trotz der Belastungen und Schwierigkeiten, denen wir in dieser Zeit ausgesetzt waren, es uns immer wieder gelungen ist, uns zu finden und zusammenzurufen. Die Selbstverständlichkeit, sowohl Herausforderungen und Arbeit, als auch Anerkennung zu teilen, sowie seine Begeisterung für die Wissenschaft haben mich tief beeindruckt. Ich habe zudem das Glück gehabt, dass ich aktiv in Diskussionen und Entscheidungen mit einbezogen wurde, was ich sehr genossen habe. Neben den vielen bohrenden, physikalischen Fragen mußte er die Erstkorrektur dieses Manuskriptes überstehen. Sehr robust! Ich bedauere, dass wir die Langzeitversuche bei der Optimierung des vollendeten Espresso genusses aus medizinischen Gründen abbrechen mußten, wir waren mit Carstens Hilfe so kurz davor . . .

Dr. Daniel Schaadt für die Unterstützung in einer sehr kritischen Zeit. Sein Rückhalt beim Überwinden der Probleme des Simulator, debuggen und kompilieren, und und und. Außerdem für die komplette Sichtung sämtlicher DVD Sammlungen auf guten Fernsehern und das wohl nie endende Gefecht um die Krone des Bowling.

Dr. Carsten Hucho für seine Bemühungen bei der Beschaffung des Servers, eines Kristalls, sowie seinem Interesse für meine Arbeiten, seine Ermunterungen und sein Verständnis für meine kleinen Zipperlein während der Zeit am PDI.

Dr. Jyoti Mohanty für die harmonische Zeit im gleichen Büro, im Labor und im Käfig. Er hat mir einen interessanten Einblick in indische Kultur gewährt von Bollywood bis zur Huldigung der Göttin Durga. Seine guten Kochkünste waren eine willkommene Abwechslung im Berliner Alltagsdön-

erlei. An dieser Stelle sei auch allen Doktoranden, insbesondere Fabian, gedankt, die zur gleichen Zeit am PDI waren.

Werner Seidel für die Unterstützung bei der Herstellung von MEMS. Er hat mir nicht nur wertvolle Reinraumtricks verraten sondern mich stetig mit den Tourdaten der Band "Totally stressed" versorgt.

Holger Pforte für die Zusammenarbeit sowohl beim Wachstum und der Charakterisierung von CNTs, als auch bei der Kombination von AFM - Spitzen mit Röhrchen. Der Genuss seines selbstgebrannten Dingsmetapfelweinblind bei zermürbenden Taktikspielchen des Besiedelns fremder Welten haben die Niederlagen weniger bitter schmecken lassen.

Dr. Martin Bowen für Diskussionen über amerikanische Politik, Symmetrien des Tunnelmatrixelements, Austauschkopplung und Tricks beim Hackesack.

Ich danke meiner Familie für die Unterstützung und den Rückhalt während des Studiums und der Promotion. Damit meine ich besonders das unerschütterliche Vertrauen meines Vaters in mich, daß mir bei allen Irrungen und Wirrungen der Faden nicht verlorenggeht, was mir den Rücken sehr gestärkt hat. Das beinhaltet aber genauso die Engelsgeduld von Dieter, mir die theoretischen Grundlagen der Physik einzubimsen und gleichzeitig deren Eleganz und Schönheit erfahren zu lassen.

Ich möchte Tante Ilse und Onkel Egon für Ihre Unterstützung danken, dass Sie mir in lebenswichtigen Belangen geholfen und mich ermutigt haben.

Ich möchte weiterhin Falk, Fabian und Kay-Uwe erwähnen. Seit wir uns kennen, haben Sie mich immer unterstützt und gute als auch schlechte Zeiten mit mir geteilt. Trotzdem ich nach Beendigung meines Studiums nach Berlin gegangen bin, hat es unsere Freundschaft kaum beeinträchtigt, und ich hoffe, daß es immer so bleiben wird.

Am Ende möchte ich meinen persönlichsten Dank an Mandy aussprechen. Ohne Ihre Toleranz, Ihr Verständnis und Ihre Unterstützung hätte diese Arbeit so nicht entstehen können. Ihr Mut und Ihre Kraft immer wieder aufs Neue zu beweisen, dass es sich lohnt *NICHT* aufzugeben, haben mich sehr beeindruckt und motiviert.

Ihr ist diese Arbeit in großer Liebe und tiefem Respekt gewidmet.



# Selbständigkeitserklärung

Hiermit erkläre ich, die vorliegende Arbeit Micromagnetic study of self-organized magnetic nanostructures selbständig und nur unter Verwendung der gemäß §6 Absatz (3) angegebenen Hilfen und Hilfsmittel angefertigt zu haben.

Ich habe mich an keiner anderen Universität um einen Doktorgrad beworben und besitze auch keinen entsprechenden Doktorgrad.

Ich erkläre weiterhin die Kenntnis der dem Verfahren zugrunde liegenden Promotionsordnung der Mathematisch-Naturwissenschaftlichen Fakultät I der Humboldt-Universität zu Berlin.

Roman Harald Engel-Herbert